KAUNAS UNIVERSITY OF TECHNOLOGY

IGNAS GRYBAS

RESEARCH AND DEVELOPMENT OF A HIGH-RESOLUTION PIEZOELECTRIC ROTARY STAGE

Doctoral Dissertation
Technological Sciences, Mechanical Engineering (09T)

2017, Kaunas

This doctoral dissertation was prepared at Kaunas University of Technology, Institute of Mechatronics during the period of 2013–2017. The studies were supported by the Research Council of Lithuania.

Scientific Supervisor:

Habil. Dr. Algimantas Bubulis, (Kaunas University of Technology, Technological Sciences, Mechanical Engineering, 09T).

Doctoral dissertation has been published in:
http://ktu.edu

Editor:

Dovilė Dumbrauskaitė (Publishing Office “Technologija”)

ISBN xxxx-xxxx

The bibliographic information about the publication is available in the National Bibliographic Data Bank (NBDB) of the Martynas Mažvydas National Library of Lithuania

KAUNO TECHNOLOGIJOS UNIVERSITETAS

IGNAS GRYBAS

AUKŠTOS SKYROS PJEZOELEKTRINIO SUKAMOJO STALIUKO KŪRIMAS IR TYRIMAS

Daktaro disertacija
Technologiniai mokslai, mechanikos inžinerija (09T)

2017, Kaunas

Disertacija rengta 2013–2017 metais Kauno technologijos universiteto Mechatronikos institute. Mokslinius tyrimus rėmė Lietuvos mokslo taryba.

Mokslinis vadovas:

Habil. dr. Algimantas Bubulis (Kauno technologijos universitetas, technologiniai mokslai, mechanikos inžinerija, 09T).

Interneto svetainės, kurioje skelbiama disertacija, adresas:
http://ktu.edu

Redagavo:

Dovilė Dumbrauskaitė (leidykla "Technologija")

ISBN xxxx-xxxx

Leidinio bibliografinė informacija pateikiama Lietuvos nacionalinės Martyno Mažvydo bibliotekos Nacionalinės bibliografijos duomenų banke (NBDB)

CONTENTS

INTRODUCTION

Research relevance, aim and objectives

High-precision positioning often plays the key role in many modern electromechanical and mechatronic devices and systems in a wide range of scale, with a sub-nanometer-size highly expected in the nearest future. Such fields as microscopy, metrology, precise machining, robotics, biomedicine, etc. significantly benefit from angular (rotary) positioning stages [1–7].

Conventional (electromagnetic) motors, extensively designed and employed as actuators for high-precision positioning applications, in particular, high-tech products (e.g. mobile medical robots, drugs delivery systems, space satellites, smart photo cameras, hand watches, etc.), can no longer meet the constantly increasing new technical requirements, including (but not limited to) compactness, simple structure, high precision, low manufacturing costs, and others. They also suffer from noise, backlash and drift, run-out errors, slow response, and so on. Therefore, a lot of effort have been put on the worldwide scale into finding alternatives. The motors based on the electrostatic, magnetostrictive, photo-thermal, thermoelectric, shape-memory and other principles are considered to be potential options [8]. However, due to their merits, piezoelectric motors (particularly, resonant ultrasonic) constitute probably the most prominent category. That is mainly governed by the ability of these devices to fulfil most of the aforementioned requirements and offer such properties as fast response, relatively large output torque at low speed, no electromagnetic interference, low noise, etc.

Although resonant ultrasonic standing-wave motors have been widely explored so far as potential drivers for the rotary stages and positioners, they still face issues associated with insufficiently high precision, scalability, structural complexity, wear of contacting surfaces, and relatively high manufacturing costs. Hence, a number of various design and technological methods are applied to solve these problems.

The aim of this research is to design, fabricate and characterise high-resolution standing-wave-driven piezoelectric rotary stage with integrated incremental scales.

In order to achieve the aim, the following objectives were raised:

1. To perform a comprehensive literature review of the existing high-precision rotary stages, placing the highest emphasis on the piezoelectric ones, and identify the possibilities of using the incremental scales for achieving high-resolution rotary motion of the stage.
2. To develop analytical and numerical models for the investigation of vibro-impact interaction dynamics and transient responses of piezocylinder and rotor.
3. To experimentally investigate the dynamic characteristics of high-resolution piezoelectric rotary stage and identify their dependence on the driving signal and applied external load.

4. To fabricate and experimentally characterise polymeric incremental scales by using contact-free and contact-based methods for the evaluation of their surface morphology and optical properties.
5. To develop geometric virtual and physical models of the designed high-resolution piezoelectric rotary stage with an integrated closed-loop feedback control system.

Research methods

This work was prepared using theoretical and experimental investigation methods. The theoretical study was carried out by analytical and numerical methods, applying SolidWorks 2016, ANSYS 17.1, Matlab 2016 and Borland C++ Builder 6 software packages. For additional graphical representation, Autodesk 3ds Max software was applied.

The experimental research was executed in the Institute of Mechatronics and the Institute of Materials Science of Kaunas University of Technology.

When performing the experiments, the analyser Wayne Kerr 6500B was used to determine the impedance characteristics of the piezoelement; a 3D scanning laser Doppler vibrometer (LDV) system Polytec PSV-500-3D-HV was employed to measure the displacement of the top surface of the piezocylinder and form motion trajectories of contact zone elements; the surface displacement of the analysed piezocylinder from qualitative point of view was evaluated by using a holographic interferometry-based measurement system PRISM 100 (Hytec); in combination with additional equipment, a single-point LDV system Polytec was utilised to measure all the major dynamic characteristics of the piezoelectric rotary stage; polymeric incremental scales were formed using a vacuum vapour deposition device YBH-71D, optical lithographic equipment, and a reactive ion etching machine PK-2420RIE.

Scientific novelty

The following scientific novelties are presented in the thesis:

1. The topology of electrodes of piezocylinder, which ensures the generation of elliptical motion trajectories of three active contact zone elements of the piezocylinder; the influence of the defined trajectories on dynamic properties of the piezoelectric rotary stage.
2. Lumped-parameter analytical model and distributed-parameter finite element model that take into account the vibro-impact interaction between the piezocylinder and rotor; the finite element model which enables to determine the dependence of rotor response in time on the applied external load.
3. Experimentally investigated dynamic characteristics of high-resolution piezoelectric rotary stage, depending on the driving signal and applied external load.
4. Novel polymeric incremental scales that can be employed instead of conventional glass-chromium incremental scales for ensuring precise angular positioning of piezoelectric stages.

Defended statements

1. The original piezoelectric rotary stage, which is driven by standing-wave vibrations of the piezocylinder, ensures high-resolution bidirectional motion of the rotor.
2. The developed finite element model of the piezocylinder is adequate to the experimental one and enables precise determination of motion trajectories of the contact zone elements.
3. Uniformity of motion of the rotor depends on the excitation frequency of the piezocylinder with respect to resonant frequency and on the air gap between the rotor and the contact zone element of the piezocylinder.
4. The fabricated novel polymeric incremental scales are comparable to conventional glass-chromium incremental scales in terms of surface quality and fidelity of raster pattern and can potentially replace them in cost-sensitive applications, ensuring the required level of precision in angular positioning.

Practical value

The designed, fabricated and characterised piezoelectric rotary stage can be applied for high-resolution angular translation of an object analysed by an optical microscope, positioning of optical elements in scientific/industrial research, dosage of liquid drugs in (bio)medical equipment, and so on. It can also be used as a teaching aid to demonstrate capabilities of mechatronic systems.

The fabricated polymeric incremental scales can be employed in precise rotary encoders and positioning systems instead of conventional glass-chromium incremental scales and are favoured to the latter ones in terms of cost-performance ratio.

The designed and fabricated high-resolution piezoelectric rotary stage with an integrated closed-loop feedback control system is comparable (or more competitive) to analogous devices on the market with respect to the main performance characteristics and superior in terms of cost-effectiveness.

Research approbation

The main results of this dissertation were published in seven scientific papers: four papers in Web of Science database-indexed journals with impact factor, one paper in a journal referred in another international database, and two national patents.

The research results were also presented in four international scientific conferences: Vibroengineering-2013 (Druskininkai, Lithuania), Mechanika 2014 (Kaunas, Lithuania), Vibroengineering-2014 (Katowice, Poland), and International Conference on Advances in Vibrations, 2015 (Porto, Portugal).

Structure of the dissertation

The dissertation consists of an introduction, five chapters, general conclusions, a list of references, scientific publications on the topic of dissertation, and five appendices.

A comprehensive literature review is provided in the first chapter. The performed analysis encompasses high-precision rotary positioning stages, conventional (electromagnetic) and piezoelectric rotary stages and their categories, and the major piezoelectric materials used in ultrasonic motors. The review also includes optical rotary incremental encoders and the scales typically exploited in the encoders, as well as the major ways of fabrication of the scales.

In the second chapter, the novel design of high-resolution piezoelectric rotary stage is presented, with the developed computational model of the piezocylinder and relevant theoretical investigation results given afterwards. The analytical and numerical models for the investigation of interaction between the piezocylinder and rotor in the time domain were also developed in this chapter.

The third chapter includes the main experimental results of the designed piezoelectric stage with respect to dynamic characteristics taking into consideration surface displacement of the piezocylinder, vibrational motion trajectories of the contact zone elements, resolution- and torque-related properties of the rotor, etc. when applying the optical and contact-based investigation methods. Also, a possible motion regime combining torsional oscillations concomitant with rotational motion of the rotary stage is revealed as a novel additional dynamic operational mode.

The fourth chapter is devoted to the fabrication process and the characterisation of polymeric incremental scales by means of contact-free and contact-based methods so as to evaluate the surface morphology and optical properties of the formed scales.

In the last chapter, geometric virtual and physical models of prototypes of the designed high-resolution piezoelectric rotary stage with integrated closed-loop feedback control system are presented.

The results of the essential theoretical and experimental investigations are provided in general conclusions.

Material supporting the main results of theoretical and experimental investigations is provided in appendices.

The volume of the dissertation is 150 pages in total, including 40 formulae, 114 figures, and 16 tables. The list of references contains 145 sources.

1. LITERATURE REVIEW

1.1. Introduction to high-precision angular positioning systems

The term “high-precision” refers to the concepts of micro-positioning and/or nano-positioning that are used to describe motor-driven stages capable of achieving micro-/nano-level displacement resolution and accuracy. High-precision positioning often plays the key role in many modern electromechanical or mechatronic devices and systems in a wide range of scale, with a sub-nanometer-size extension highly expected in the nearest future. Such fields as microscopy, metrology, precise machining, robotics, biomedicine [1–6], semiconductor and IT industries [7] and others significantly benefit from angular (rotary) positioning stages.

Various precise rotary stages have been developed over the last fifty years. Despite the changes in design, each of them contained an actuator for motion generation (stator) and a driven output link (rotor). Essentially, these two components represent a motor (drive). If a position sensor with associated displacement readout and control units is present, the device is referred to as a stage, though a lot of cutting-edge stages have been ambiguously called ‘motors’ or ‘drives’ in literature and elsewhere. Unlike translational positioning, a stage possessing 3 degrees of freedom (DOF) with respect to X, Y and Z axes, rotary stage enables the restriction of translational motion of the output link in all the stated directions but maintain the capability to exhibit rotation about those axes, i.e. roll, pitch, and yaw.

Conventional (electromagnetic) motors have been extensively designed and employed as actuators for precise positioning applications all over the world and have significantly contributed to our society in both the academia and industry. With the pass of years, the relevant theories, design methods and production techniques have been developed so successfully that they undergo just incremental improvements. The ever-increasing demands in science and technology (in particular, high-tech products, e.g., drug delivery systems, space satellites, smart photo cameras, hand watches, etc.) are constantly raising new technical requirements for motors. The criteria include (but are not limited to) compactness, simple structure, high precision, and low manufacturing costs. Low noise and no electromagnetic interference are among the most desirable qualities as well. Nonetheless, the structure and operation principle of conventional actuators imposes limitations on the possibilities to meet these requirements. Therefore, a lot of effort have been put on the worldwide scale into finding alternatives. Motors based on the electrostatic, bionic, photo-thermal, shape-memory and other principles are considered to be potential options [8]. However, piezoelectric (particularly, ultrasonic) motors stand for probably the most prominent category. It is mainly governed by the ability of these devices to fulfil most of the aforementioned requirements and, in addition, offer such properties as a response of millisecond-level order, relatively large output torque, etc. At the heart of the piezoelectric motor, there is a piezoelectric transducer converting electrical energy to mechanical one. Nowadays, piezoelectric motors are utilised as one of the major means in

various processes, where precision of micro-/nano-scale is demanded. Characterised by reliability, piezoactuators have been applied in medical engineering, aviation, nuclear sector, consumer devices, automotive industry, etc.

In case of angular positioning, the precision of displacement measurement is substantially affected by the resolution of a system, not to mention the previously stated criteria, system dynamics, and mass of both the stage and the object to be positioned. According to [9], resolution is the smallest mechanical step which the machine (or a part of it) can make during point-to-point motion. Although the given definition is rather straightforward, it is actually referred to as a programmable part of positioning stage (e.g., the smallest increment of displacement encoder), whereas the minimal incremental motion is meant to express the adequate feature related to motion of the device. Resolution can be significantly smaller than the minimal actual motion of the output link, which is the key distinction disclosed very rarely. The factors potentially affecting the minimal incremental motion include friction, load, vibrations and inertia, system dynamics, external forces, and motion controller peculiarities [10]. Nonetheless, for the sake of simplicity, the concept of resolution will be used to characterize the overall performance of a system everywhere in this work later on.

1.2. Conventional and piezoelectric rotary stages

The application of proper design principles is critical for successful implementation of rotary positioning stages, thus each of the four previously enumerated components (i.e. actuator, output link, position sensor with displacement read-out unit, control unit) has to be carefully considered for its contribution to the performance of the device. Since these are the fundamental elements of any positioning stage defining how well the operation can be executed, they are worth to be explained in more detail.

Conventional (electromagnetic) rotary stages

A lot of technical processes and industrial applications involve conventional rotary positioning stages, each of which is directly dependent on the performance of the electromagnetic motor (EM). Despite the numerous choices of additional elements of rotary stage, they all fall into the major groups elaborated below.

1) Motion generated by an actuator

Examples of EM are mainly servomotors and stepper motors easily available in almost any size, with their power varying from a few milliwatts to several watts. Beside the distinction of the motors in terms of the number of magnetic poles, servoactuators offer a high speed and torque (even for short periods of time), reliability, quiet operation, and close-loop control ensuring the desired operation of the overall system. Efficiency value reaches 80–90%. Stepper actuators, on the other hand, are an alternative possessing a higher torque at lower speeds than servomotors of the same size, as well as the opportunity to provide a constant holding torque without the need for the motor to be powered. High power density, easy drive control (open-loop), variety in size, simplicity of the structure and relatively low cost are the benefits in this case as well [11, 12].

2) Output link with a mechanical transmission

All rotary stages consist of some form of a movable platform (output link) contacting with the motion generator via a mechanical transmission that allows rotation of the platform only about a single axis with respect to the housing (base). Acceptable performance of the rotary stage requires the surfaces of the platform to match not only those of mechanical transmission elements, but also the surface of the object to be positioned upon request. Therefore, such materials as stainless steel, aluminium, brass and granite are most commonly selected to manufacture the platform. Young's modulus, density, yield strength, thermal conductivity and expansion are critical properties in making the right choices during the design phase.

Worm drives and gear boxes encompass the mechanical transmission part. The first group is commonly used for rotary systems of a very low profile design. In order to eliminate backlash, both worm (screw) and worm wheel (gear) need to be in a perfect contact with each other, which requires a sophisticated worm preloading system with high transversal stiffness. High torque capacity and self-locking capability are the advantages of this kind of drive. Another way is to utilize gearboxes which act as reducers to obtain the required resolution, torque and speed, all of which are difficult or impossible to obtain with standard motors. Gearboxes can introduce considerable backlash and hysteresis to the motion [13]. The absence of the described measures in the transmission elements convert the rotary stage to the direct one (instead of indirect), thus easing its maintenance, decreasing the frictional effects, low inertia, etc. [14].

Bearings are the primary elements of mechanical transmission, which ensure smooth low-friction rotary motion between two surfaces. They account for the run-out errors of the rotor; namely, eccentricity and wobble. The stiffness of the rotor (but not in the direction of travel) and its static load capacity are also influenced by the bearings. Dynamic load capacity, however, is primarily limited by the rigidity of the transmission drive train and power of the motor [13]. Ball bearings are among the most widely employed for the given purpose. Aerostatic, hydrostatic and magnetic types of guides are available as well.

3) Position sensor with a displacement read-out unit

The ability of allocating an accurate and unambiguous angular position value make the position sensor with a displacement read-out unit one of the most substantial links between the mechanical components and control system of the stage. The sensors are split into two groups – digital and analogue. Laser interferometers and grating scales fall into the first category, with encoders, capacitive, inductive and magnetic sensors comprising the second class. Due to the difficulties arising from the adaptation of digital sensors to conventional rotary stages, the analogue sensors are mainly exploited. Absolute or incremental encoders and capacitive sensors comprise the largest part of the relevant market, because they can come close to the highly-performing grating scales with respect to uncertainty, repeatability, resolution, bandwidth, and measuring range properties [14, 15].

4) Motion control unit

The motion control unit is an electronic device physically separated from all the previously mentioned components of the system. It has the capability to store the

desired motion profile as a function of time or any other reference signal, process data related to the actual position feedback, calculate the error and send a command signal to the generator/amplifier of the driving signal as a complex function of the error and its derivatives, so that the desired angular position would be achieved. It can also monitor various I/O signals and communicate with additional peripheral devices (e.g., a computer) [16]. The most commonly used control mechanism is a PID (proportional-integral-derivative) or PWM (pulse-width-modulation) algorithm, but other ways are also possible. The control unit can be separated into the controller itself and the amplifier or integrate both elements in one box.

- Representative commercial devices

Commercial EM-driven rotary positioning stages can be classified into four groups depending on the type of actuator providing mechanical motion via direct/indirect drive. Several representative examples of similar dimensions and medium load capacity devices (without motion control unit) are shown in Fig. 1.1.

a) Aerotech ANT130-R

b) Newport RGV100BL

c) Thorlabs CR1-Z7

d) Newmark RM-3

e) Newmark HR-3

f) Primatics PLR190

g) Thorlabs NR360S

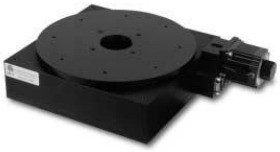

h) Dover RTR

Fig. 1.1. Commercially available conventional rotary positioning stages containing a servomotor with direct (a, b) and indirect (c, d) transmission and a stepper motor with direct (e, f) and indirect (g, h) transmission [17–22]

Table 1.1 compares the given rotary positioning stages in terms of essential performance characteristics. Comparing the features, it can be stated that stages with direct transmission achieve better operational characteristics than the stages containing mechanical drives. In particular, the performance of servomotor-driven devices is of a rather high level.

Table 1.1. Essential performance characteristics of commercial conventional rotary positioning stages (referring to Fig. 1.1) [17–22]

Parameter	**Servomotor-driven stages**				**Stepper motor-driven stages**			
Notation in Fig. 1.1	a)	b)	c)	d)	e)	f)	g)	h)
Gear drive	No	No	Yes	Yes	No	No	Yes	Yes
Travel range (degrees)	360	360	360	360	360	N/A	360	360
Accuracy (arc sec)	10	11	N/A	70	N/A	2	300	180
Repeatability (arc sec)	1.5	2	<60	5	N/A	1	10	36
Resolution (arc sec)	0.01	0.4	2.2	3.6	50.4	0.2	1	7.2
Speed (rpm)	200	120	1	30	2,000	2.5	8.3	20

- Issues and limitations

Despite all positive aspects associated with conventional rotary positioning stages, there are many issues and limitations which constrain those devices from the perspective of high-precision positioning applications. As a rule, it is mainly determined by structural components; EM, mechanical transmission and rotational mechanism mostly impact it. The majority of issues and limitations are [8, 23–24]:

1) Moderate accuracy, repeatability and resolution – these features are highly dependent on the number and distribution of magnetic poles inside the motor.

2) Size and performance – desired performance of the system is limited by the dimensions and complexity of the driving elements.

3) Backlash and drift – the need for a gear drive to increase angular resolution magnifies the backlash and drift problems.

4) Run-out errors – bearings are responsible for the presence of eccentricity and wobbling issues.

5) Slow response – arises from the intrinsically highly inductive input impedance.

6) Limited dynamic response – it is invariably limited by the motor inertia, inductance, and motor drive technology.

7) Load-dependent performance – performance is sensitive to changes in load, particularly, in the absence of positional feedback mechanisms.

8) Need for continuous power – continuous power supply is required even when the system is stationary (i.e. in a braked position).

9) Need for keeping in position – continuous sensing of small positional errors is a must to hold the system locked on the target (i.e. at the desired position).

10) Loss of tracking – the risk of loss of the tracking-demanded position is present whenever the load exceeds the motor torque rating.

11) Motor burnout – the risk of motor burnout, if the latter is jammed physically, when a continuous demand for movement is present.

12) Stick-slip effect – non-linear dynamic phenomenon, when the initially applied driving force generates no motion (stick) of the system until the force exceeds static friction of the system, and there is a jump in position, which causes a small over-shoot (slip). Stick-slip imposes limitations on accuracy, resolution and speed of response of the system.

13) Noise – the motor generates audible noise during operation, particularly at high speeds.

14) Increased maintenance costs – a variety and complexity of structural components increases the maintenance costs.

15) Sensitivity to electromagnetic noise – due to the operation principle, the motor is sensitive to external electromagnetic noise/interference.

16) Environmental issues – constant demands for electricity cause extensive use of rare-earth elements for permanent magnets (e.g., neodymium) of motors, thus inducing long-lasting environmental issues in the global scale.

- Market and applications

Though conventional rotary positioning devices are inherently characterised by the revealed limitations, they are still used to a considerably large extent. The systems come in various dimensions and mounting types. Industrial robots, CNC machines, fibre optics and photonics, semiconductor equipment and micromachining, medical, office and household appliances are some of the areas where these products generate scientific and practical gain [23, 25].

Piezoelectric rotary stages

In order to compare a conventional angular positioning stage with a piezoelectric one, the actuators, as the crucial elements for motion generation, have to be considered. An output link with a mechanical transmission, a position sensor with a displacement read-out unit and a motion control unit should be neglected in this case, since these components are very similar to those employed in analogous electromagnetic-based stages.

In a broad sense, a piezoelectric motor is an actuating device that creates a linear or rotary motion by means of converse piezoelectric effect – piezoelectric material is deformed under effect of applied electric field. The piezoelectric motor aims to move an object over a certain distance with a high resolution and accuracy [26]. This distance is very short, since the occurring deformations are very small – the maximal elongation is commonly less than 0.1% of the length of piezoelectric transducer [27].

Depending on the operation frequencies, piezoelectric motors are mainly classified into non-resonant (quasi-static) motors and ultrasonic motors (USMs). Usually, an ultrasonic motor utilises the mechanical resonance at high frequency to increase the output motion, whereas a quasi-static motor operates at low frequency with a stable response [26]. Based on wave propagation methods, the USMs are

classified into standing- and traveling-wave devices. Correspondingly, non-resonant motors are separated into those operating on the basis of stepping (including inchworm, seal and walking drives) or inertial principle (impact/stick-slip, self-inertia, impact-inertia drives) [26, 28]. Each of these groups is discussed in greater detail further in this chapter.

- Representative commercial devices

Commercial piezoelectric rotary stages can be categorised according to the type of employed piezoelectric motor. Fig. 1.2 provides several examples of similar dimensions and medium load capacity devices (motion control unit is not included).

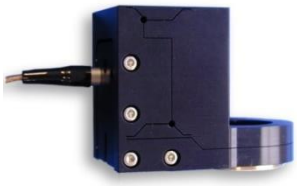

a) Cedrat OPP120SM

b) Piezomotor Piezo LEGS WavePlate

c) Attocube ECR5050

d) SmarAct SR5714

e) PI Q-632

f) Nanomotion FBR060

g) PI U-628

Fig. 1.2. Commercially available piezoelectric rotary stages containing non-resonant stepping (a – seal, b – walking), non-resonant inertial (c, d, e – impact), and resonant ultrasonic standing-wave motors (f, g) [29–35]

The key performance characteristics of the shown piezoelectric stages are listed in Table 1.2. It is observed that non-resonant-type devices are mostly

distinguished by high resolution and developed torque, with resonant ultrasonic standing-wave-driven devices characterised by high speed.

Table 1.2. Essential performance characteristics of commercial piezoelectric rotary stages (referring to Fig. 1.2) [29–35]

	Non-resonant (quasi-static)					Resonant ultrasonic	
Parameter	**Stepping**		**Inertial**				
Notation in Fig. 1.2	a)	b)	c)	d)	e)	f)	g)
Category	Seal	Walking drive	Stick-slip	Stick-slip	Stick-slip	Standing-wave	Standing-wave
Gear drive	No	No	No	No	No	No	No
Travel range (degrees)	N/A	360	360	360	360	360	360
Accuracy	N/A	N/A	N/A	N/A	N/A	10″	N/A
Repeatability	N/A	N/A	N/A	5%	0.62″	NA	21″
Resolution	14 nm	0.01″	0.018″	0.72″	0.62″	0.5″	10.5″
Speed (rpm)	N/A	17	1.5	1.7	7.5	60	120
Torque (mNm)	N/A	20	50	40	6	N/A	25

A summary of the major benefits and drawbacks of piezoelectric rotary stages is given below.

Table 1.3. Major pros and cons of piezoelectric rotary stages [8, 26, 28, 37]

No.	Benefits	Drawbacks
1.	Easy scalability	Special requirements for amplitude, frequency and phase of control signal
2.	Simple design	Difficult support of stator
3.	Fast response	Heat generation inside stator
4.	High precision, accuracy, resolution	Presence of stator hysteresis
5.	Noiseless operation	Presence of stator creep
6.	No gear drive or brake mechanism	Unsuitability for long continuous operation
7.	May/may not include bearings	Low power output and efficiency
8.	No backlash	Complex control circuitry
9.	No electromagnetic interference	Short operational lifetime
10.	High output torque at low speed	High cost
11.	High torque/weight ratio	-
12.	High holding torque	-
13.	Presence of self-locking	-
14.	Compatibility with extreme environmental operational conditions	-

- Market and applications

Despite of the limitations attributed to the piezoelectric rotary stages, both academia and industry still pay a lot of attention to them. This tendency is determined by valuable positive aspects, with most of them helping to address the performance properties of EM-driven positioning devices. A variety of operation principles and design configurations are practical solutions for different high-tech markets, including semiconductor technology (mask and wafer alignment),

biotechnology/life science (optical testing of specimens, cell sorting), aeronautics and space applications (satellite positioning), (micro)robotics (grippers and manipulators), consumer devices (toys, wristwatches, camera lenses), and so on. Some of these implementations are disclosed in Fig. 1.3.

a)  b) 

Fig. 1.3. Examples of application of piezoelectric rotary stages for precise positioning of: a) satellite in space; b) self-learning geosystem measurement station [37–38]

1.3. A review of piezoelectric rotary motors and drives

There are two main groups of piezoelectric motors and drives used in angular positioning stages, i.e. non-resonant (quasi-static) and resonant ultrasonic devices. A schematic representation of classification of these devices is shown in Fig. 1.4.

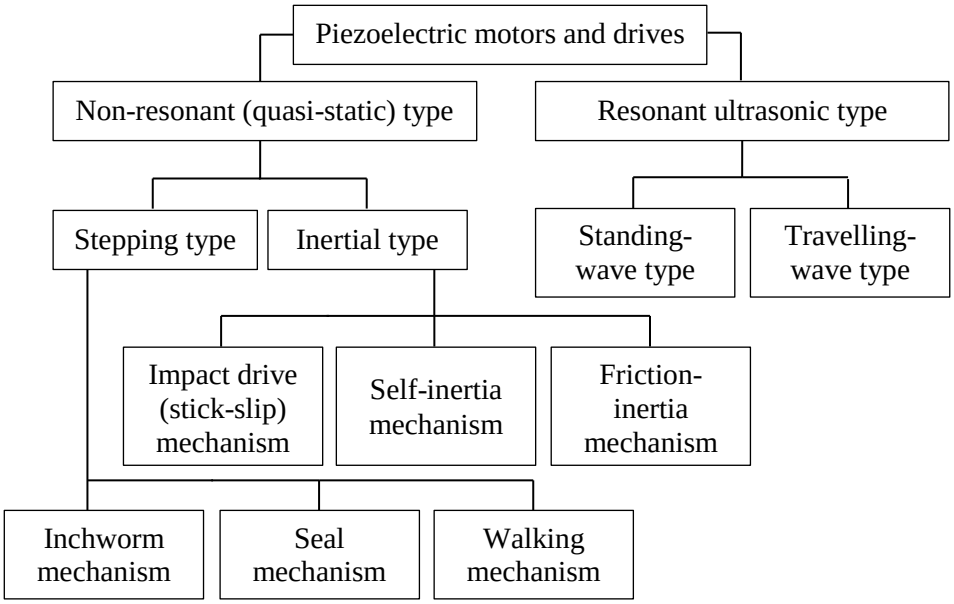

Fig. 1.4. A schematic representation of piezoelectric motors and drives classification [26, 28]

1.3.1. Non-resonant stepping type

In the stepping-based mechanisms, the piezoelectric motor consists of several piezoactuators that are integrated within a mechanical structure in a way to generate

motion by a sequence of expand-contract and/or clamp-unclamp cycles [28]. Piezoelectric motors based on the inchworm, seal and walking mechanisms are discussed further; their operation principles are shown in Appendix A and corresponding detailed descriptions are provided in Table 1.5.

Inchworm mechanism

Much attention has been paid to piezoelectric inchworm motors during the years, as most of them are suitable for precision instruments due to fine motion with nanometer accuracy [28]. Most of these motors have an angular step size less than 1 mrad. However, some of them have difficulties in assembly because of a strict gap requirement between the stator and the rotor. Others are limited by their rotation ranges and output torques [39]. The three groups of inchworm motors found in literature are: a) "walker" (actuator moves through a fixed guide way); b) "pusher" (shaft moves through a fixed body of actuator); c) "walker-pusher" (hybrid mode). In general, the operation of these motors relies on the basis of "pusher" mode motion patented by Wiliam G. May in 1975 [40].

It should be noted that until now most of the announced inchworm actuators have been linear, so rotary motors of this type are still being researched and developed. However, several examples are available; Li et al. constructed a novel drive which can realise stepping rotary movement with high accuracy by means of nine piezoelectric stacks and flexure hinges (Fig. 1.5). The fabricated prototype is featured by minimal stepping angle of 4.95 μrad, when the driving voltage is 20 V and the excitation frequency is 1 Hz; the maximal output torque (93.1 Nmm) is observed at 100 V driving voltage, with the maximal angular speed (6508.5 μrad/s) registered at 30 Hz [39]. Kim and Kim created a precise motor driven by inchworm motion using two belts. A lever structure with flexure hinges is designed to reduce the number of components and the assembly effort. A rotational motion with the step size of 2.36 μrad is obtained. The maximal speed (416,005 μrad/s) and developed torque (3 Nmm) was identified in the presence of 100 Hz and 40 V driving signal in this work [41]. Hu et al. proposed another version of the drive which is able to reach the minimal step of less than 2.6″ induced by signal of 20 V and 5 Hz; the maximal speed of 430.4″/s can be reached under the applied voltage of 160 V [42]. Several other designs of motors were developed by the authors as well [43–44].

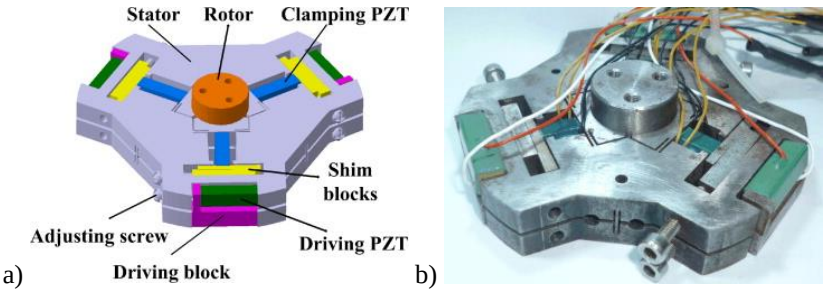

Fig. 1.5. The model (a) and prototype (b) of a piezoelectric rotary inchworm motor [39]

Seal mechanism

A seal mechanism is another clamping and feeding mechanism that has nearly the same structure as the inchworm-driven actuator. It consists of friction devices (elements) *A* and *B* connected with a piezoelectric extension device. Element *A* is passive and applies constant frictional force, while element *B* is controlled by an on-off action, thus, causing clamp-release operation at the base. The following relation has to be satisfied in order to initiate the motion of actuator [26, 45]:

$$F_{BOff} < F_A < F_{BOn}; \quad (1)$$

here F_A is the constant frictional force between the friction device *A* and base, F_{BOn} is the frictional force, when the friction device *B* adheres (i.e. is clamped), and F_{BOff} is the frictional force, when the friction device *B* is free (i.e. is released).

So far, only a couple of motors of this type are known. All of them were designed by Furutani et al. In 2001, the team proposed a mobile device with three DOF for a scanning probe microscope. The motor is comprised of two piezoactuators, two controlled electromagnets, and an electromagnet generating constant friction. The control of the two main electromagnets enables one to alternate corresponding frictional forces. With extended/contracted piezoelements, the operation of the third electromagnet (and thus, the motor) is executed. In the presence of 100 V, the resulting displacements per cycle in X and Y directions were 8.8 μm, and angular displacement was 0.19 mrad [45]. The performance of the improved motor design was reported in [46–47].

The walking mechanism

In the walking-type motors, several drive elements (piezo-actuated legs) alternately engage and disengage in a frictional contact to a movable slider. Both clamping and releasing of the slider are realised by the same piezo-actuated legs, in contrast to the separate set of clamping and extensional actuators in the inchworm motor. Due to the nature of up-down as well as the forward-backward movement of the piezo-actuated legs, this mechanism is considered to simulate a walking sequence of biological species [26, 48].

One of the first motors of this type using the classical walking mechanism was proposed by Brisbane in 1968 [50]. It was mainly composed of two piezoelectric disc-shaped plates functioning as actuators attached to a hollow cylinder (i.e. movable member) at both ends. Galutva et al. developed a motor which is the same in operation but slightly different in structure in 1972 [51]. 23 years later, Marth et al. created a motor which contained four piezo-actuated legs that press a slider to make a linear motion, with each piezo-actuated leg able to be controlled separately [52]. This motor became a predecessor to the novel walking mechanism practically implemented by the Swedish company PiezoMotor Uppsala [53]. The rotary stage based on this operation principle was already presented in the previous subchapter. A similar motor was developed by Physik Instrumente (PI) in Germany. In this case, the device makes use of clamping and feeding actions achieved by longitudinal and shear actuators contained in four piezo-actuated legs [28].

In general, all the clamping-feeding mechanisms described in this section are characterised by a rather high output force/torque but low speed, complicated structure and control. There are also some issues regarding the reliability and applications of the mechanism in a small space, as well as weak signal measurements [26].

1.3.2. Non-resonant inertial-type mechanisms

In the inertial-type mechanisms, the piezoelectric motor operates mainly on the basis of inertia of a moving mass connected to some sort of a shaft (usually, made of metal) which, in turn, is attached to a piezo-actuator. The motors driven by piezoelectric friction-inertial actuators (PFIA) are known for their long-range and high-resolution motions [54]. There are three motion generation mechanisms [28, 55]; each of them is schematically illustrated in Appendix A, with the corresponding principles presented in Table 1.5.

- Impact drive (stick-slip) mechanism
- Self-inertia mechanism
- Friction-inertia mechanism

It should be noted that actuators (and thus, motors) based on the impact drive (stick-slip) and self-inertia mechanisms are commonly called piezoelectric friction-drive actuators (PFDA), and those relying on the friction-inertia mechanism are commonly named piezoelectric inertial-drive actuators (PIDA) [54]. A typical structure of a PFDA- and PIDA-driven motor involves the following (see Appendix A): a supporting frame (ground), a piezoactuator (*PA*), a driving object, and an end-effector (slider) [54]. The two latter (c-d) actuators are also called the impact drive mechanism (IDM) and smooth impact drive mechanism (SIDM), respectively. The only difference between them is that the counter object in the SIDM is supported by the ground with a very small friction. This makes SIDM more stable than IDM in terms of lateral movement of the counter object [26, 54].

Since the introduction of the first well-known PFDA and PIDA-driven motors proposed by Pohl in 1986 and Higuchi in 1990 [36], many translational motors of this type for different applications have been designed. Some of them were commercialised by such companies as PI, SmarAct, Nanomotor, Attocube, etc. [28]. Nonetheless, literature does not extensively describe the rotary versions of these motors and drives (particularly, those of 1-DOF). In 2010, Gao et al. developed an impact drive (stick-slip) motor (45 x 45 x 35 mm^3) capable of generating linear and rotational motion (Z-θ_Z), where the moving member (steel cylinder) is supported and actuated by two driving units, each of which consists of two piezoelectric elements and a friction component realised by a permanent magnet (Fig. 1.6a–b). The piezoelectric motor was found to achieve the angular speed of 1.1 rad/s and a resolution of 48.5 μrad [56]. Chen et al. developed a friction-inertial motor based on asymmetrical clamping structures (Fig. 1.6c–d). The designed actuator with symmetrical electrical signals produces a rather large inertial driving moment difference because of the existence of the bias unit. In this case, the angular speed is 5.39 rad/s, resolution is 14.3 μrad, and torque is 3.62 Nmm [62].

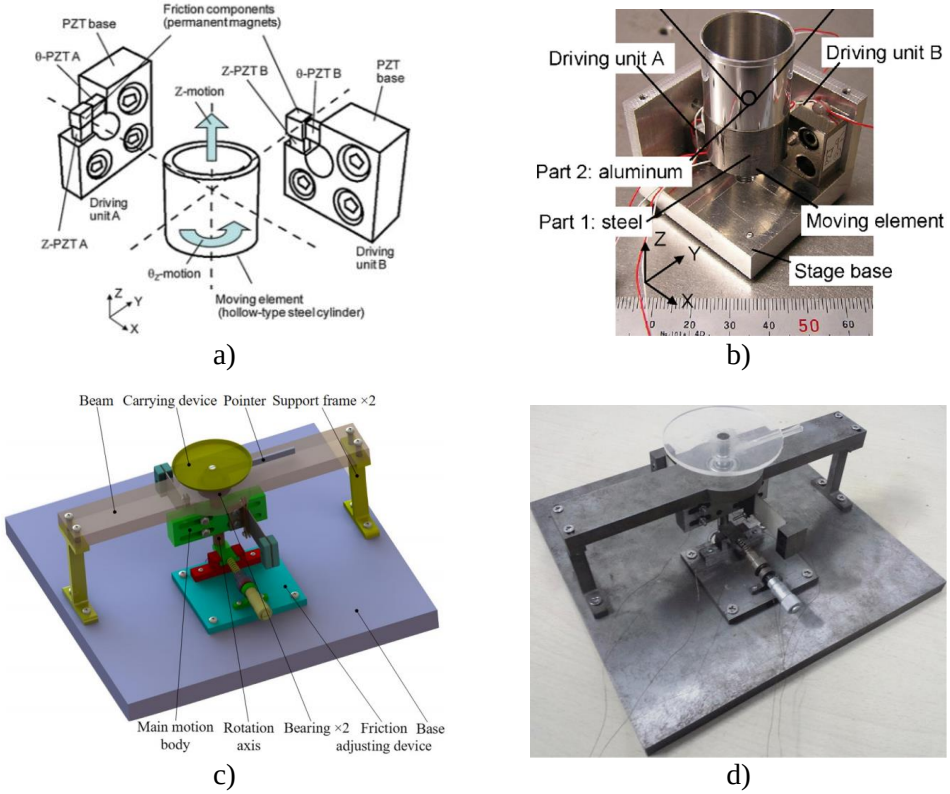

Fig. 1.6. The model and prototype of piezoelectric rotary impact drive (stick-slip) motor (a, b) [56] and friction-inertial motor (c, d) [62]

The performance characteristics of other relevant analysed motors are summarised and provided in the table below. Since no information about the designed self-inertia motors was found, they are not included in this table.

Table 1.4. Performance characteristics of typical piezoelectric non-resonant inertial-type motors

Author	Motor type	Speed	Resolution	Torque	Size
Gao et al. [56]	Impact drive (stick-slip)	1.1 rad/s	48.5 μrad	N/A	45 × 45 × 35
Morita et al. [57]		2.83 rad/s	N/A	5.5 mNm	Φ16 × 40
Bergander et al. [58]		0.21 rad/s	N/A	N/A	10 × 10 × 0.5
Wang et al. [59]		0.024 rad/s	0.13 μrad	N/A	N/A
Zhang et al. [60]		2.4 rad/s	N/A	1.6 mNm	Φ8 × 10
Peng et al. [61]		1.57 rad/s	10.2 μrad	N/A	11 × 11 × 5.7
Chen et al. [64]	Friction-inertia	5.39 rad/s	14.3 μrad	3.62 Nmm	N/A
Buechi et al. [62]		6.28 rad/s	0.1 μrad	0.3 mNm	10 × 7 × 7
Cheng et al. [63]		4.02 rad/s	0.85 μrad	2.48 Nmm	N/A
Van de Wulp et al. [65]		0.5 rad/s	N/A	N/A	N/A
Shim et al. [66]		1 rad/s	0.64 μrad	N/A	50 × 50 × 50
Zhang et al. [67]		0.2 rad/s	1 μrad	20mNm	55 × 40 × 40

To sum up, PFIA-driven motors are relatively simple in structure and compact in size. In addition, they are characterised by rather simple operation and high accuracy and resolution in comparison with other types of piezoelectric motors. On the other hand, they are not very rigid, as well as prone to vibration. Their developed angular speed, output torque and efficiency are relatively low due to the quasi-static operation, friction coupling mechanism, and sliding friction dissipation [26, 28].

Operation principles with the main advantages and disadvantages of piezoelectric non-resonant-type motors and drives are summarised and given further.

Table 1.5. Operation principles, advantages and disadvantages of piezoelectric non-resonant-type motors and drives

1. Stepping type. Inchworm mechanism (see Appendix A)
The motor usually has two sets of clamps and a mechanism for generating rotor motion. One clamp is fixed to the stator and the other is attached to the rotor. A repetition of clamping and feeding motion cycles enables the shaft to be driven continuously over a long range. The direction of the shaft can be reversed by changing the clamping sequence of the two clamps. The stroke of each cycle is limited by the maximum displacement of the central piezoactuator. Advantages include compactness, no backlash, high precision and accuracy, high output force/torque, etc. On the other hand, at least three phases of operation are needed which makes the motor complex. The operation principle leads to vibration of the shaft (or other driven element). High precision in manufacturing is also a challenge required to be met so that the clamps would operate reliably [26].
2. Stepping type. Seal mechanism (see Appendix A)
The motion of the actuator is described by the following sequence: 1) The extension device is contracted, and friction device *B* is off; 2) Due to the presence of $F_{BOff} < F_A$ at friction device *B*, the actuator moves to the right; 3) Friction device *B* is powered on; 4) Because $F_A < F_{BOn}$ at friction device *B* is valid, friction device *A* is retracted towards friction device *B*. The motion direction can be reversed by changing the sequence of extension and contraction of the piezoelectric element. The presented operational regime is known as the coarse mode, since movable range is virtually infinite. When friction element *B* is off, it can be driven with a finer step by changing the length of the extension device continuously. The latter regime is called the fine mode. The seal mechanism utilises passive elements, thus decreasing the number of controlled actuators but retaining the same performance characteristics as those of the inchworm mechanism [26, 45].
3. Stepping type. Walking mechanism (see Appendix A)
The walking motors can usually operate in the stepping mode and/or bending mode. In the first case, two of piezo-actuated legs are in contact with the rod until the other two acquire the rod. A four-phase electrical excitation signal is necessary for this mode. If, for instance, a sinusoidal signal is applied, there should be a 90° phase shift between phases *1* and *2*. Phases *3* and *4* should be shifted by 180° with respect to phases *1* and *2*, respectively. In the case of bending mode, four piezo-actuated legs generate a constant clamping contact with the rod and move forward and backward simultaneously. So as to induce this motion, a 90° phase shift between the two phases is sufficient [49]. The walking mechanism, comparing to the inchworm mechanism, has a more complex structure but allows for the clamping motion of one piezo-actuated leg during its feeding phase. Therefore, it can cooperate with the movement of the shaft fed by other piezo-actuated legs. Hence, the walking drive mechanism can move continuously and smoothly with high rigidity [26].
4. Inertial type. Impact drive (stick-slip) mechanism (see Appendix A)
When applying a saw-tooth voltage signal, each cycle consists of a slow deformation (extension) of the piezoactuator (*PA*), with the driving object followed by an abrupt jump backwards (contraction). During the slow deformation, the slider follows the piezoactuator together with the driving object because of friction ('stick'), whereas it cannot follow the sudden jump back because of its inertia ('slip'). This mechanism provides long displacements at a relatively high velocity (typically up to 5 mm/s) and resolution (on average 200–400 nm) [26, 55].

5. Inertial type. Self-inertia mechanism (see Appendix A)
During self-inertia motion, the actuation force generated from the inertia of the slider primarily is smaller than the static friction force between the driving object and the ground. Therefore, the driving object 'sticks' on the ground. When the voltage rapidly decreases, the actuation force becomes larger than the friction force between the piezoelement and the slider. As a result, the *PA*, the slider and the driving object 'slip' rightward on the ground. Once the voltage decreases to the original level, the *PA* is back to the neutral state [54, 55]. This mechanism provides motion characterised by long range and high resolution [26, 55].
6. Inertial type. Friction-inertia mechanism (see Appendix A)
Starting from a completely contracted state, the piezoactuator pushes the counter object with a small acceleration and makes a slow extension, which generates the inertial force that does not exceed the static friction between the main object and the ground. The main object keeps its position ('stick' phase). When the voltage rapidly decreases, the PA pulls the counter object with a large acceleration, and the slow extension is suddenly reversed into a very fast contraction, resulting into an inertial force higher than the static friction ('slip' phase). This causes a small step of the main body [54, 55]. This mechanism provides motion characterised by long range and high resolution [26, 55].

1.3.3. Resonant ultrasonic standing-wave type

Unique design and operation principle enable the piezoelectric resonant ultrasonic motors to achieve nanometer/sub-nanometer level displacement accuracy and resolution. Hence, among the piezoelectric motors, USMs have been the most studied ones [36]. Ultrasonic (above 20 kHz) resonant mechanical vibrations are the driving source in this case. The operation of these motors is realised by converting the cyclic motion of piezoelectric element to an effective work of the rotor. This is achieved by means of a friction coupling between the stator and the rotor [8].

Depending on the way to generate elliptical motion, resonant USMs are separated into two major groups: 1) standing-wave-type; 2) traveling-wave-type. There is no uniform further classification of these motors, but differentiation based on vibration modes of stator, contact state between the stator and rotor or the number of degree of freedom of rotor is found in literature. Considering that vibration modes are the basis for USMs design (in particular, for standing-wave type), the classification according to oscillation modes is considered to reflect the properties of these motors in the most reasonable way [8, 26, 28]. The major modes exploited when designing standing-wave motors are: longitudinal mode, bending mode, torsional mode, and radial mode. These characteristic modes are shown Fig. 1.7. Nevertheless, the majority of rotary motors are driven using the combined modes, including (but not limited to) orthogonal bending mode, longitudinal-bending mode, longitudinal-torsional mode, etc. [8, 26].

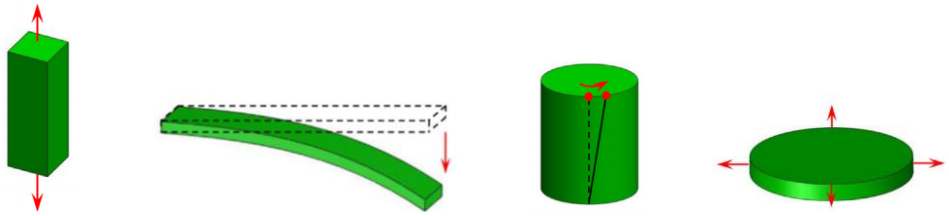

Fig. 1.7. The basic vibration modes used to generate motion in piezoelectric resonant USMs: a) longitudinal; b) bending; c) torsional; d) radial (in-plane) [26]

- Longitudinal vibration mode

Longitudinal vibration mode is one of the essential modes frequently utilised in resonant ultrasonic standing-wave motors (RUSWMs). It is sometimes called the axial mode, and leads to the axial displacement of the piezocylinder. This mode is often combined with others, such as, bending or torsional, to achieve the desired motion. Commonly, this type of motors uses a well-known Langevin transducer with a high converting efficiency. However, the abrasion of the friction material on the contact surface is a serious issue. The first standing-wave linear motor proposed by Sashida employed this vibration mode. The classical piezoelectric resonant USMs designed by Lavrinenko in 1965, Barth in 1973, Vasiliev in 1981, Bansevičius in 1988 were based on this mode as well [8, 26]. In 2002, Wischnevskiy was granted a US patent [68], on the basis of which a lot of different linear and rotary motors have been produced by company PI. The core of these RUSWMs is a rectangular piezoelectric plate with two sectioned electrodes on the frontal side and a ground electrode at the back side (Fig. 1.8). A frictional (coupling) element is attached to the top of the plate, between the two separated electrodes. If one of the sections is excited by high-frequency electrical excitation signal, the longitudinal vibrations are induced within the plate in both longitudinal and transversal directions. This causes the friction tip to continuously contact with the runner and thus make it move. The principle is also valid for cylinder-shape piezoelectric stator.

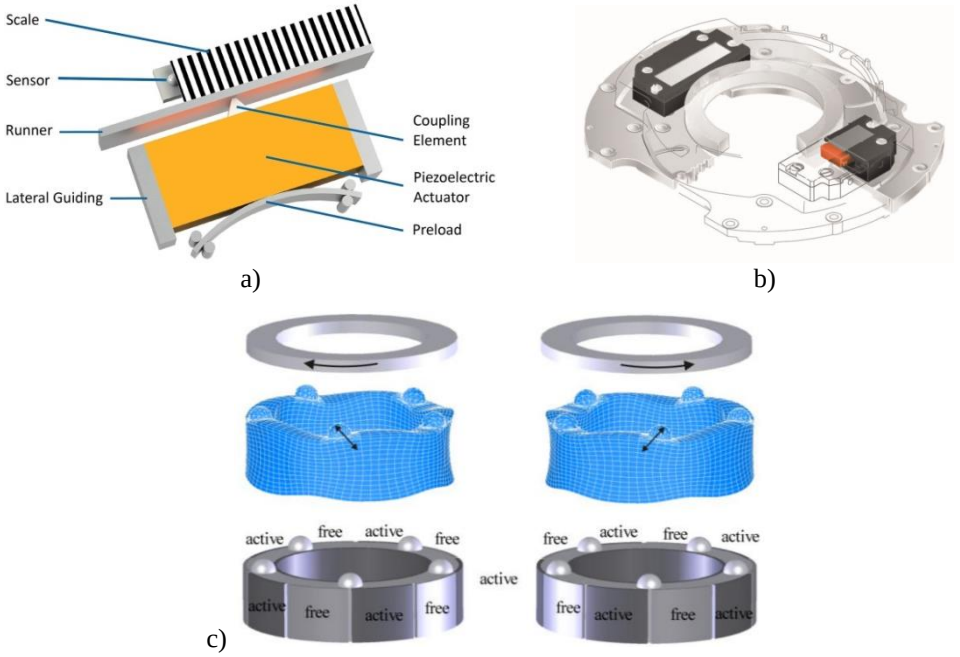

Fig. 1.8. Piezoelectric RUSWM design used by the PI (Physik Instrumente) company: a) the excitation of longitudinal vibration mode in piezoelectric plate-based drive; b) the application of piezoelectric plates in low-profile motor; c) the excitation of longitudinal vibration mode in piezocylinder [69]

In this case, the number of piezoplates are mutually connected in order to ensure a uniform motion of the rotor. So as to change the direction of motion, the opposite section (group of sections) has to be excited.

- Bending vibration mode

As it is indicated in Fig. 1.7, this mode is characterised by bending deformations perpendicular to the longitudinal axis of piezoelement [26]. The bending mode has not been widely applied, though several versions of these piezoelectric RUSWMs were proposed by Bansevičius and Ragulskis [70]. In 2011, He et al. developed a motor using only a single bending vibration mode of a piezoelectric tube containing four electrode sections to generate rotation. When the piezoelectric tube with special teeth bends, the diagonal motion of points on selected areas at the ends of the tube generates forces with tangential components along the same circumferential direction, thus, initiating the motion of the rotor. The obtained angular speed is 400 rpm and torque of about 300 μNm when applying a sinusoidal driving signal of ±50 V [71]. It should be noted that this oscillation mode is very popular in combination with other modes.

- Torsional vibration mode

In terms of physical expression, torsional vibration is angular vibration excited by shear deformation of the upper part of the stator. Torsional vibration mode is commonly used in combination with other orthogonal modes [26], and there are not many investigations performed with actuators of this type. A representative example is a miniature piezoceramic fibre wound with helical electrodes on its outer surface proposed by Pan et al. [72].

- Radial vibration mode

In the case of radial vibration mode, the stator is deformed (and thus, displaced) in the radial direction. Commonly, the radial mode is always combined with the bending mode to generate the necessary elliptical motion [26].

- Orthogonal bending vibration mode

Orthogonal bending vibration mode can be perceived using the illustration in Fig. 1.9a. Having the same piezoelectric element (e.g., beam) with multiple electrodes and supplying the corresponding two excitation signals at the same time, two orthogonal bending modes are created, resulting in the rotation of the beam and elliptical motion of the tip in X-Y plane [26]. One of the orthogonal bending vibration mode-driven RUSWMs was introduced by Kurosawa et al. in 1989 [73]. A short piezocylinder with free-free ends acted as the major component. The dimensions of the device were 20 mm in diameter and approximately 75 mm in length. The maximal output torque was 0.15 Nm, and load-free angular speed was up to 300 rpm. Due to its favourable properties, this piezoelectric motor was successfully applied in the focusing unit of Canon DSLR camera lenses [8, 73]. A compact ultrasonic motor (2.4 mm in diameter and 10 mm in length) operating at 69.5 kHz was proposed by Koc et al. [74]. Its operation was based on the performance of a hollow metal cylinder, the outside surface of which was flattened on two sides at 90 degrees to each other, on which two rectangular piezoelectric plates were bonded. In this case, the maximal torque of 1.8 mNm was obtained, with angular speed being 60 rad/s. Another version of the motor which makes use of this

vibration mode was developed by Liu et al. in 2013 [75]. A miniature SQUIGGLE motor belongs to this type as well [26].

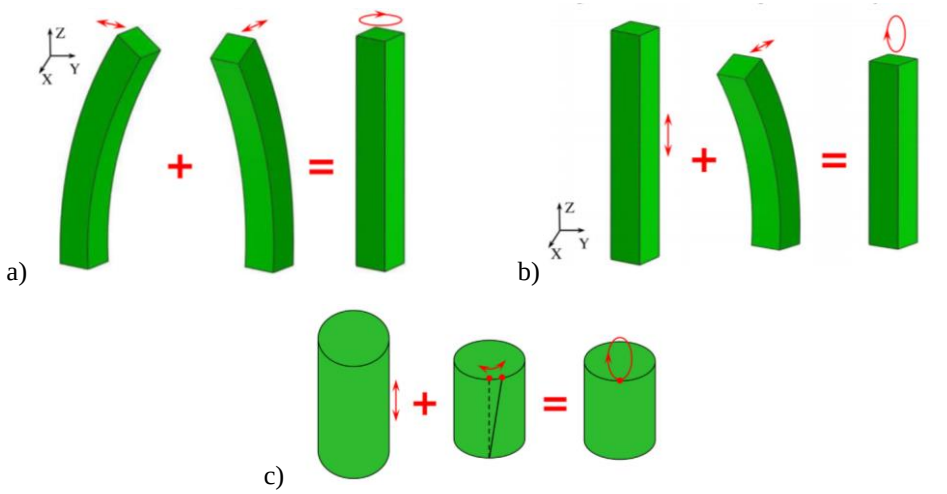

Fig. 1.9. The main vibration modes used to generate motion in piezoelectric resonant USMs: a) orthogonal bending; b) longitudinal-bending; c) longitudinal-torsional [26]

- Longitudinal-bending vibration mode

The generation principle of this mode is given in Fig. 1.9b. The early structures of these piezoelectric RUSWMs were intended for linear motion. Later, the rotary-type versions were designed [70]. After about 15 years, Suzuki et al. and Aoyagi et al. proposed miniaturised motors characterised by impressive angular speed [26]. By far, the motors of this category comprise the largest group of piezoelectric resonant USMs. An abundant amount of implementations with respect to dimensions, excitation frequency, voltage, output torque and angular speed can be found in literature [8, 28, 76].

Imagine a simplified version of the piezoactuator (Fig. 1.9b) with the tip attached and pressed against X-Y plane representing the rotor. Assume that the resonator is excited by a harmonic (sinusoidal) driving signal and that the natural frequencies of the resonator and the tip coincide. Then the resulting horizontal (x) and vertical (y) displacement locus of the tip point describes an ellipse defined by the laws provided further [76]:

$$x = A_0 \sin(\omega t + \alpha), \tag{2}$$

$$y = A_1 \sin(\omega t + \beta); \tag{3}$$

here A_0, A_1 are the vibrational amplitudes, ω is the angular frequency, t is the time, and α, β are the vibrational phases.

The latter principle has been applied in the well-known piezoelectric RUSWMs owned by Nanomotion. Fig. 1.10 provides a schematic illustration of the employed actuator; the operation principle of the motor is as follows: four electrodes denoted as A, A', B and B' are bound to the front face to form a checkerboard pattern

of rectangles, with each electrode covering one-quarter of the surface area. The diagonally located electrodes *A* and *A′* as well as *B* and *B′* are electrically connected by wires. The rear face is fully covered by a single electrode which is grounded via the tuning inductor that can change the resonant frequency. The excitation of electrode sections *A* and *A′* leads to motion generation. Reverse motion requires *B* and *B′* electrodes to be energised. The movement of the motor is constrained by four support strings with large stiffness along the long edges [77].

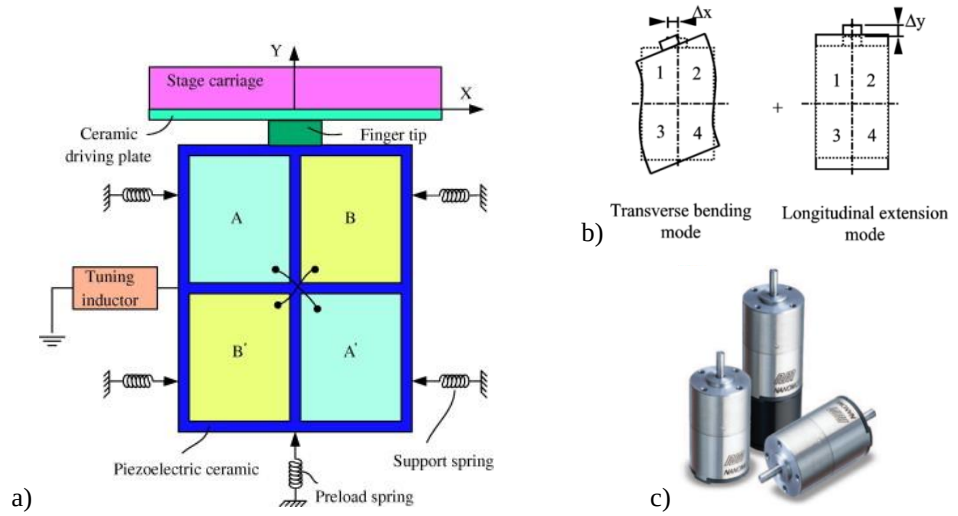

Fig. 1.10. Piezoelectric RUSWM of Nanomotion Ltd: a) the structure of a piezoactuator; b) the excited longitudinal-bending vibration mode; c) motor (ER-15-4) design [77–78]

- Longitudinal-torsional vibration mode

A schematic depiction of this vibration mode is shown in Fig. 1.9c. In 1991, Kurosawa et al. developed one of the first motors of this type [28]. The Penn State University proposed a compact piezoelectric RUSWM (Fig. 1.11a), the stator of which is composed of the piezoelectric ring and two concave/convex metal endcaps with ‘windmill’-shaped slots bonded together in order to generate a coupled vibration of longitudinal-torsional-type. When driven at 160 kHz, the maximal angular speed equal to 600 rpm and torque of 1 mNm are obtained for 11 mm diameter motor [76].

A more recent research enabled Watson et al. to create a miniature piezoelectric RUSWM (Fig. 1.11b); the stator is 250 μm in diameter, 1 mm in length, and it is driven by a single piezoelectric transducer at 652–682 kHz. At 28.1 V, it outputs the maximal torque of 13 nNm and angular speed of 1295 rpm [79].

It should be noted that the discussed combined modes are the major ones. Nonetheless, there are also piezoelectric RUSWMs based on other modes, e.g., longitudinal-shear, radial-torsional, torsional-bending, and so on. Various modes are often applied not only for 1-DOF, but for multiple DOFs as well. Due to a wide range of possible designs, dimensions and performances (in particular, angular speed and output torque), RUSWMs act as a competitive alternative to resonant ultrasonic

travelling (propagating or ‘surfing’)-wave motors (RUTWMs) that will be discussed in the next section.

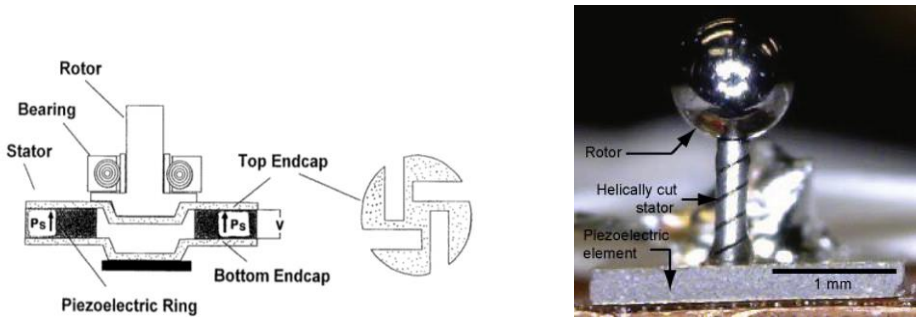

a) b)

Fig. 1.11. Piezoelectric RUSWMs utilising longitudinal-torsional vibration mode: a) ‘windmill’ motor developed by the Penn State University [76]; b) miniature motor with stator of 250 μm in diameter and 1 mm in length proposed by Watson et al. [79]

1.3.4. Resonant ultrasonic travelling-wave type

In general, the operation of piezoelectric RUTWMs is partially similar to that of the RUSWMs. Elliptical motion is generated in the stator and then transferred to the rotor through friction coupling. However, it is not generated at one point within the stator; instead, every point on its surface undergoes elliptical locus due to the combination of longitudinal and transversal waves.

Assuming that the standing wave of flexural vibration of the *n*-th mode is excited along an elastic ring (Fig. 1.12a), the out-of-plane displacement of an induced standing-wave can be expressed as [76, 81]:

$$u_{s1}(x,t) = A\cos(nx)\cos(\omega t); \tag{4}$$

here x is the angular position, t is the time, n is the integer number of vibration mode in the circumferential direction, and ω is the angular frequency of vibration. Another standing wave of the same order but shifted by 90° with respect to both space and time is written as:

$$u_{s2}(x,t) = A\sin(nx)\sin(\omega x). \tag{5}$$

Then the resulting travelling (progressive) wave in the circumferential direction is obtained from the superimposition of both standing waves and defined by:

$$u_t(x,t) = A\cos(nx)\cos(\omega t) + A\sin(nx)\sin(\omega x) = A\cos(nx - \omega t). \tag{6}$$

One should assume that the electrode on the outer surface of the piezoring is divided into an appropriate number of sections to excite the two standing waves. By using, for example, a four-phase source (*Vcos(ωt)*, *Vsin(ωt)*, *-Vcos(ωt)*, *-Vsin(ωt)*) as a driver the second-order (n = 2) vibration is induced within the piezoring (Fig. 1.12b). The formed motion of a single particle on the surface of an elastic body transmitting a traveling wave is represented in Fig. 1.12c.

The shape of the elliptic motion and the ratio of the in-plane to the out-of-plane displacement component are determined by the thickness and radius of the body and the mode order. The rotational speed is proportional to the in-plane vibration component, whereas the contact between the surface of piezoelectric transducer (vibrator) and the rotor is controlled by the out-of-plane component [81].

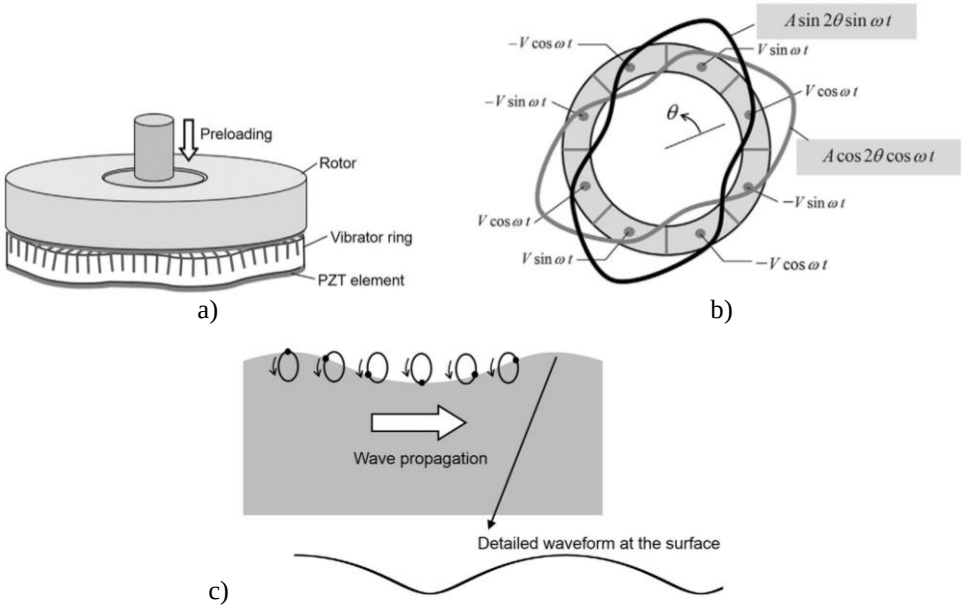

Fig. 1.12. The operation principle of the piezoelectric RUTWM: a) basic structural components; b) four-phase driving voltage application to generate traveling waves; c) the motion of a single particle on an elastic body transmitting a traveling wave [81]

The nature of piezoelectric RUTWMs ensures sub-nanometer accuracy and displacement resolution to be exhibited in various angular positioning systems. On the other hand, both the amplitude of the propagating wave and the complex design of the motor have a detrimental effect on the scalability of these devices.

The amplitude of the wave reduces linearly with the scale of the device. As a sub-millimetre scale actuator is approached, the vibration amplitude becomes so small that it becomes difficult to use as a driving mechanism in an actuator. Although the analysed RUTWMs are characterised by relatively low theoretical efficiency (max. 50%) compared to RUSWMs (up to 90%), they are capable of actuating bi-directionally, which is often an obstacle for the RUSWMs [76].

Probably the most famous and successful piezoelectric RUTWM was created and patented in 1984 [55] and commercialized one year later by Sashida in Japan. The basic structure and the produced motor are presented in Fig. 1.13. Due to the travelling wave induced within a thin PZT piezoring, a ring-shape slider contacting with a “rippled” surface of the elastic body bonded onto the piezoring is driven in both directions by exchanging the sine and cosine voltage inputs connected to two vibration sources (*a* and *b*). The teeth in the stator increase the flexibility of the motor and amplify the motion of the output link. The piezoelectric ring is divided

into 16 positively and negatively poled regions and two asymmetric electrode gap regions so as to generate the travelling wave of the ninth vibration mode at 44 kHz frequency. A prototype was composed of a brass ring of 60 mm in the outer diameter, 45 mm in the inner diameter and 2.5 mm in thickness bonded onto a PZT ring of 0.5 mm in thickness, with divided electrodes on the backside. The rotor was made of polymer coated by hard rubber or polyurethane. The application of the noted frequency and input voltage of 10.3 V led to the achievement of the maximal torque (around 100 × 103 μNm) and angular velocity higher than 30 rpm. The maximum power reached was 0.8 W, and the efficiency equal to 35%. Canon installed these motors in the in-lens automatic focus units [26, 76, 81].

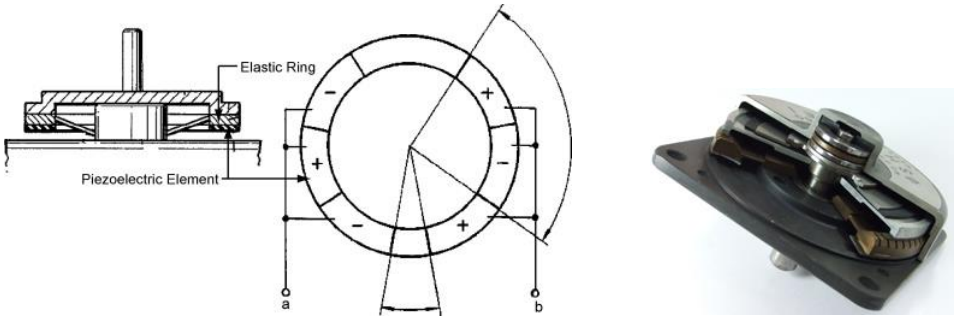

a) b)

Fig. 1.13. Sashida's piezoelectric RUTWM: a) patented design [81]; b) produced version (USR-60-4-100) [82]

Other design involves Matsushita Electric which proposed a nodal line support method using a higher order vibration mode. In this model, the stator structure incorporates a wide ring supported at the nodal circular line, and the teeth are arranged on the maximum amplitude circle to obtain larger revolution [76]. Seiko Instruments miniaturized the RUTWM to 10 mm in diameter and 4.5 mm in thickness using basically the same principle. A driving voltage of 3 V and a current of 60 mA provides 6000 rpm (no load) and torque of 0.1 mNm [76]. Another intriguing variant is a 'plate-spinning' type proposed by Tokin, where a rotary bending vibration is excited on a PZT rod by a combination of sine and cosine voltages, and then a cup is made to contact the 'spinning' rod with the internal face for achieving rotation [76].

Another type of piezoelectric RUTWMs is the surface acoustic wave (SAW) motor, also known as a Rayleigh wave. Basically, it is an acoustic wave traveling along the surface of an elastic material. The resulting wave couples longitudinal and shear wave and has a normal displacement component to a boundary [26]. Kurosawa et al. is known to have proposed the first motor of this type in 1996, with an updated modified version in 2006 [26]. A micromotor based on the rotation of the arbitrary axis was reported by Tjeung et al. in 2011 [26].

Summing up, it can be stated that piezoelectric RUTWMs exhibit less abrasion on the contact surfaces due to continuous drive of the rotor by travelling wave. High frequency allows for high accuracy of motion of the rotor. Due to the dual-signal

drive, the RUTWM possesses easier control of bidirectional motion. From the point of view of demerits, these motors can be used in applications requiring short-time operation, since heat dissipation is challenging. The complex structure of stator, dual-signal drive and the linear reduction of the needed amplitude of the wave with the size of the device make it difficult when trying to miniaturise the RUTWM. Last but not least are the manufacturing costs of the motor, which are high because of two vibration sources necessary to generate one wave [28].

1.4. Piezoelectric materials for ultrasonic motors

As it was already mentioned, when an electric field is applied to piezoelectric material, its shape is changed. A selection of this material for the purpose of actuation is highly important, since it determines the operation quality of a device.

Although there are a lot of piezoelectric materials, they all can be classified into the following categories [28]:

1) Inorganic piezoelectric materials (piezoelectric monocrystalline materials and piezoceramics). Typical examples are quartz (SiO_2), lead zirconate titanate (PZT), barium titanate ($BaTiO_3$), lead titanate ($PbTiO_3$), lead magnesium niobate-lead titanate gallium (PMN-PT), langasite ($La_3Ga_5SiO_{14}$), potassium niobate ($KNbO_3$), bismuth ferrite ($BiFeO_3$), etc. Piezoelectric monocrystalline materials benefit from the factor of high mechanical quality and excellent stability but low piezoelectric coefficient and dielectric constant. In addition, the machining of these materials is often troublesome. Piezoceramics are characterised by a strong piezoelectric coefficient and high dielectric constant, but they face low mechanical quality factors, large electric losses, and poor stability. Therefore, inorganic piezoelectric materials are mostly applied as actuators, sensors, filters, etc. [28, 83].

2) Organic piezoelectric materials (piezoelectric polymers). Typical examples include polyvinylidene fluoride (PVDF), polyvinylidene difluoride (PVDF2), and other co-polymers. These materials exhibit excellent flexibility, low density, small impedance, and low piezoelectric coefficient. These characteristics enable piezoelectric polymers to be utilised in the fields of ultrasonic measurement, pressure sensing, energy harvesting, etc. [28, 83].

3) Composite piezoelectric materials (a combination of inorganic (mostly, piezoceramic) and organic materials). One of the advanced materials are active fibre composites (AFCs) and macro fibre composites (MFC). As well as any other composite materials, composite piezoelectric materials are intended for a better, enhanced performance which often requires high piezoelectric coefficient, high strength, low density, and easy machinability. Such materials are gaining a lot of attention, because they can be applied in such fields, as bio(medicine), electroacoustics, hydroacoustics, and so on [28, 83].

The production of piezoelectric resonant USMs mostly uses the ceramics (particularly, in the monolithic form). Despite the brittleness, which induces limitations in terms of strain of the piezoceramics, and susceptibility to fatigue crack growth (when these materials are subjected to high frequency cyclic loading), they are still exploited a lot, with PZT acting as the preference in various engineering fields, particularly, mechatronics. Such a wide spread is mainly caused by high

coupling factors as well as piezoelectric and dielectric constants of PZT over extended temperature and stress ranges [84]. Low production costs, chemical inertness and relatively high operating temperature are other positive qualities [83].

There are three substantial properties of piezoelectric material that have to be seriously considered for potential application in piezoelectric resonant USM. These are as follows: 1) electromechanical coupling factor (*k*); 2) dielectric constant (ε); 3) mechanical quality factor (*Q*). The indicated parameters should be as high as possible for the analysed purpose. Table 1.6 contains the essential piezoelectric constants of common piezoelectric materials.

Table 1.6 Material properties of commonly used piezoelectric materials [8, 84–85]

Property	PZT	$BaTiO_3$	PVDF
Coupling factor, k_{33} (CV/Nm)	0.68	0.49	0.18
Coupling factor, k_{31} (CV/Nm)	0.33	0.21	0.12
Piezoelectric constant, d_{33} (10^{-12} C/N)	300	191	33
Piezoelectric constant, d_{31} (10^{-12} C/N)	-11	-79	23
Dielectric constant, $\varepsilon/\varepsilon_0$	1,300	1,680	12
Mechanical quality factor, Q_m	1,000	1,300	4
Young's modulus, E (GPa)	50	67	3
Curie temperature, T_c (^oC)	330	115	170

1.5. Rotary encoders as a means to determine angular displacement

High resolution is indispensable to cutting-edge rotary positioning stages. For this reason, further emphasis is placed on digital rotary encoders allowing one to measure angular displacement precisely. The operation of the encoders is commonly based on one of the following methods [86]:

- Optical (photosensor)
- Sliding contact (electrical conducting)
- Magnetic saturation (reluctance)
- Proximity sensing

Even though all of them are widely utilised in practice, the first one gains most attention when considering resolution, compactness, and reliability. A simplified classification of the latter encoders is illustrated in Figure 1.14.

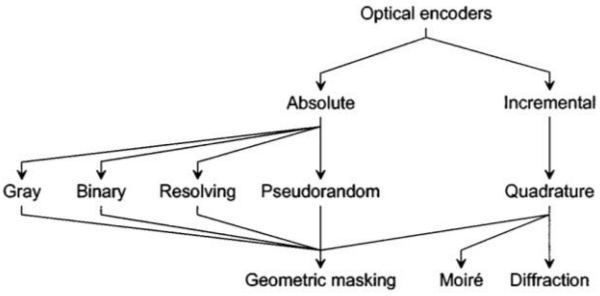

Fig. 1.14. A simplified classification of optical encoders [87]

Knowing that the opportunity to define distances between individual 'steps' is more important than determination of an absolute position in the case of high-

resolution rotary stage, incremental encoders were selected for further analysis. A typical encoder of this type consists of incremental (grating) scale (usually, made of glass) used as a measurement reference, an optical head unit (e.g., photodiode) for reading the scale graduations, and associated electronics [88–89].

The following three techniques are applied to generate electrical signals obtained from a relative movement of the angular grating (scale) with respect to the optical head(s) in the optical incremental encoders: 1) geometric masking; 2) Moiré effect; 3) laser interference (interferential read-out).

- Geometric masking

a) Light transmission

Geometric masking relies either on light transmission or reflection phenomenon. A transmissive encoder is composed of an emitter, a detector and associated electronics located at the opposite sides of the code wheel. The light from the emitter (LED) collimated by a lens passes through the rotating disc (moving grating) and propagates through the stationary one (mask or index grating). The scale is scanned by a photodetector (reading head) to generate an electrical output (i.e. angular displacement) according to the amount of light on its sensitive surface.

b) Light reflection

Fig. 1.15a shows a schematic operation principle of the reflective encoder. Most of its elements coincide with those of the transmissive transducer. Nonetheless, the emitter, detector and board of electronics are located at the same side of the code wheel. The light beam falling on the reflective area (rasters) of the code wheel is reflected back to the photodetector. The latter component generates the output signal according to the amount of the received light. These encoders do not require any masking element, which significantly simplifies the overall system design [90]. A common scheme of arrangement of optical and electronic elements in the reflection-based encoder is depicted in Fig. 1.15b.

Due to the simplicity, small dimensions, reliability and low cost-performance ratio, encoder of this type is considered as the most suitable one to register angular displacement in high-resolution piezoelectric rotary stage presented in this thesis.

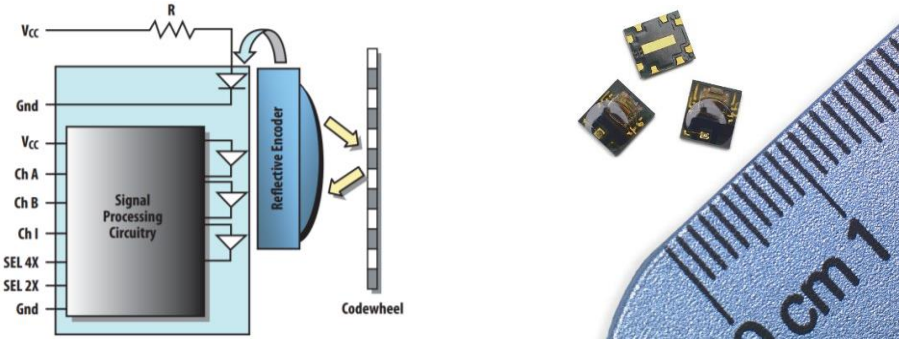

a) b)

Fig. 1.15. Geometric masking technique based on light reflection: a) the interaction of optical head with incremental scale of the encoder [93]; b) the smallest commercial three-channel optical reflective encoder AEDR-850-100 (Avago) [94]

- Moiré effect

Moiré is an optical technique for the full-field and non-contact measurement of in-plane and out-of-plane deformations [95]. The Moiré pattern is an interference pattern (fringes) typically created when the light passes through two periodic gratings (scales) overlaid at a certain angle (superposition) or when they have slightly different mesh sizes (periods). In such cases, one of the gratings is stationary, while another one moves. A source of light is placed on the moving side of the plate, and the photosensor(s) is(are) located on the opposite side (as for transmissive encoders). During the motion of the scale, a pulse train is generated by the photodetector, and the output signal can be used to determine the desired displacement and/or velocity.

- Laser interference (interferential read-out)

The encoders of this type are successfully referred to as encoders of physical optics, in opposite to the geometrical ones. When a light wave passes through the scanning reticle, it is diffracted into three partial waves of orders +1, 0, and –1 with approximately equal luminous intensity. The partial waves are diffracted by the step reticle (main scale acting as the measuring standard) and meet again at the phase grating of the scanning reticle (of the same period as the main scale), where they are diffracted again and interfere. This produces essentially three wave trains which leave the scanning reticle at different angles. Photodetectors convert alternating light intensity into electrical signals as an output [30–31].

1.6. Incremental (grating) scales

With circular incremental scales being indispensable to successful angular displacement measurement in rotary positioning stages, it is obvious that there is a high need for the mentioned structural elements to be not only qualitative and reliable, but also featured by a competitive cost-performance ratio. When seeking for alternatives, the fabrication techniques and materials have to be considered.

1.6.1. Fabrication methods

For many years, conventional UV-lithography has been used to fabricate rotary incremental scales of various diameters, thickness, and grating period. One of the best-known approaches utilised in practice joins an ordinary lithographic technique with physical vapour deposition. The combination is commercially available and ensures high throughput in terms of formation of the grating scales (in particular, relatively large in size). This process also ensures high accuracy and renders the scales extremely resistant to chemical and mechanical abrasion [97–98]. Glass-chromium incremental scales are mostly obtained in this way. However, the described formation method is subject to limitations dealing with the physics of diffraction and the interactions of high energy photons, thus, causing the restricted smallest pitch to be about 40 nm. Moreover, this method is not suitable for the formation of an easy pattern on the polymeric or curved substrates. Also, large areas with significant resolution in a single step cannot be patterned. Probably the essential issue attributed to this technique is high capital and operational costs correspondingly causing high cost-performance ratio of the scales [98].

Nanoimprint lithography (NIL) has been flagged as an extremely promising process for next-generation lithography due to its simplicity, low operational costs, high replication fidelity (lines up to 15 nm in thickness), and relatively high throughput when fabricating micro-/nanometer scale patterns [97]. NIL is based on the principle of mechanically modifying a thin polymer film (mechanical deformation of resist) using a template (mould or stamp), which contains micro-/nano-pattern, by using a thermo-mechanical or UV-curing process (UV-NIL). Thus, NIL is separated into thermal nanoimprinting (hot embossing) and UV-nanoimprinting (UV-casting). These processes are schematically represented in the figure below. The disadvantages of the T-NIL include high temperature resulting in difficulty of demoulding and significant residual thermal stress due to different coefficients of thermal expansion between the mould and the polymer. As a result, the embossed devices suffer from global warpage or distortion due to mechanical and residual thermal stresses [100]. Compared to T-NIL, UV-NIL requires much lower imprinting force, and it can be carried out at room temperature. In addition, it is a rapid and very precise (high aspect ratios can be obtained) technique [98].

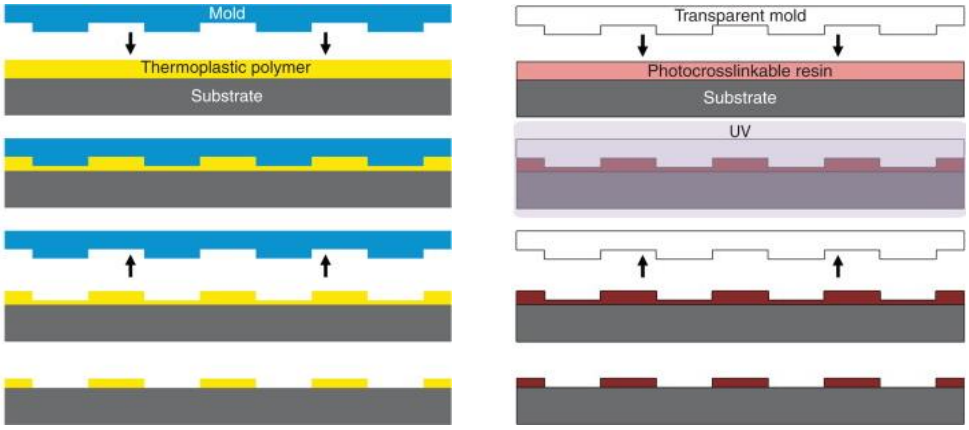

Fig. 1.16. Two fundamental processes of nanoimprint lithography (NIL): a) thermal nanoimprinting (hot embossing); b) UV-nanoimprinting (UV-casting) [99]

1.6.2. Substrate materials

Substrates necessary to produce incremental scales play a crucial role in order to achieve the desired results in both the academia and industry. When the scales are fabricated by using conventional UV-lithography, they are usually made of glass. Soda-lime (float) glass is the basis for this purpose due to its favourable material properties (light transmission, optical clarity, mechanical strength, etc.) and sufficient surface adhesion with respect to the coating of chromium or other similar substances that form the final pattern of these scales. However, the cost of this material is quite high, thus, being the major issue. Nonetheless, everyday products and devices, for instance, architectural building windows, automobile glass, household mirrors, solariums, greenhouses, solar cells make use of this glass [102]. The essential material properties of the float glass are listed in Table 1.7.

Polymers are increasingly attractive alternatives to inorganic materials in many photonic devices, including surface relief structures and grating scales. They offer several unique advantages over the existing semiconductor and inorganic technologies, such as cost-effective fabrication, adequate transparency in the visible and near-infrared spectra, as well as versatility in structures and grades [103]. Polymers are lightweight, making the produced devices possible to be integrated with the existing silicon/non-silicon-based technologies. The optical properties of polymers can be engineered to give the desired refractive index, loss, transparency or electro-optic coefficient. Moreover, the emerging lithographic technologies (including NIL) are well-suited to affordable mass production of polymeric structures [104–105]. It is known that thermal nanoimprinting is compatible with polymethylmethacrylate (PMMA) and other methacrylate-based polymers, polystyrene, co-polymers containing aromatic components, siloxane co-polymers, etc. [98]. Also, different acrylates are widely applied in UV-NIL because of their commercial availability and suitable inherent material properties [98]. Polyethylene terephthalate (PET) is one of the substances which have lots of opportunities to be used as a substrate for potential grating scales. In its natural state, PET ($C_{10}H_8O_4$) is a colourless, semi-crystalline or rigid, lightweight, strong resin. Table 1.7 contains the essential material properties of PET. According to the given data, being not as elastic as float glass and exhibiting larger value of thermal expansion coefficient, PET is still very attractive due to the remaining properties and low cost-performance ratio.

Table 1.7. Material properties of float glass and PET [101, 106–107]

Property	Float glass	PET
Density, kg/m^3	2,500	1,380
Young's modulus, GPa	72	3
Poisson's ratio	0.23	0.4
Optical transmission, %	90	90
Refractive index	1.51	1.58
Coefficient of thermal expansion, 10^{-6}/^{o}C	8.3	60
Thermal conductivity, W/m ^{o}C	0.94	0.25

1.7. Chapter conclusions and the objectives of the thesis

This chapter presented a comprehensive review of recent publications, technological means and descriptions of the existing high-precision rotary positioning stages. Based on this, the following conclusions were made:

- Piezoelectric rotary stages outperform the ones driven by electromagnetic motors in terms of compactness, simple structure, high precision, other technical properties, and low manufacturing costs.
- Resonant USMs are among the most popular piezoelectric motors used for high-precision positioning applications. RUSWMs and RUTWMs are the two categories of these motors; the first group is characterised by high speed and torque, simple excitation, easy support of stator at the nodal points/lines, theoretical efficiency up to 98%, and decreased manufacturing costs because of a single vibration source. The disadvantages encompass insufficiently

high precision, scalability (in some cases), complexity of the structure and discontinuous rotor motion causing wear of contacting surfaces. The second group benefits from high accuracy of rotor motion and less abrasion of the contacting surfaces due to continuous drive of the rotor. Nonetheless, the challenges include heat dissipation in the stator, its complex structure, difficult miniaturisation of the motor and decreased manufacturing costs due to the necessity of two vibration sources.

- For the production of piezoelectric resonant USMs, inorganic materials (ceramics) have been most widely applied, with PZT often acting as the preference mainly because of high coupling factors as well as piezoelectric and dielectric constants over extended ranges of temperature and stress.
- Optical rotary encoders are very popular when considering their application in high-precision rotary stages. The optical reflection technique is found to be the most suitable when generating an output signal for applications requiring a small space, high resolution, and low cost-performance ratio.
- Nanoimprint lithography has been flagged as a highly promising technique to form polymeric incremental scales due to its simplicity, low operational costs, high replication fidelity, and relatively high throughput. This method can take the form of T-NIL or UV-NIL; the first one results in difficulty of demoulding and significant residual thermal stress, whilst the second one is rapid, very precise, requires a rather low imprinting force, and can be carried out at room temperature. Due to its favourable properties, PET is one of the polymers which has lots of opportunities to be used as a substrate for incremental grating scales fabricated by UV-NIL.

Aim and objectives

According to the literature review and the findings, the aim and objectives of this work were formulated.

The aim of this thesis is to design, fabricate and characterise a high-resolution standing-wave-driven piezoelectric rotary stage with integrated incremental scales.

In order to achieve the aim, the following objectives were raised:

1. To develop analytical and numerical models for the investigation of vibro-impact interaction dynamics and transient responses of piezocylinder and rotor.
2. To experimentally investigate the dynamic characteristics of high-resolution piezoelectric rotary stage and identify their dependence on the driving signal and applied external load.
3. To fabricate and experimentally characterise polymeric incremental scales by contact-free and contact-based methods for the evaluation of their surface morphology and optical properties.
4. To develop geometric virtual and physical models of the designed high-resolution piezoelectric rotary stage with an integrated closed-loop feedback control system.

2. THEORETICAL INVESTIGATION OF A HIGH-RESOLUTION PIEZOELECTRIC ROTARY STAGE

Based on the findings of literature review and the formulated objectives, the high-resolution piezoelectric stage has to be theoretically investigated before proceeding to the next steps. This chapter presents the information regarding the design and operation principle of the developed object, followed by the presentation of geometric model of the stage. A computational model of piezocylinder (PC) is provided afterwards, placing an emphasis on harmonic and modal analysis as well as the motion of contact zone (driving) elements. Lastly, analytical and numerical approaches are used to analyse the interaction between the contact zone elements and the rotor.

2.1. Design and operation principle

The rotary stage was developed in cooperation with the Lithuanian high-tech company Precizika Metrology specialising in the production of various cutting-edge measurement systems, rotary encoders, and incremental scales (i.e. limbs). Considering the professional expertise, technological capabilities and requirements of the mentioned enterprise, it was decided upon the form, dimensions and characteristics of the actuator, which would be novel in the scientific field and attractive for the commercial market. Moreover, in the case of high-quality operation of the stage, a range of different scale (including miniature) devices will be generated in the future. Considering all these details, the design of the conceptual stage model was created and proposed initially (Fig. 2.1). The stage is composed of housing (*1*), three supporting base elements (*2*), a piezocylinder (*3*), three contact zone elements (*4*), a rotor (*5*), a rotor shaft (*6*), a precise bearing (*7*), a magnet (*8*), non-magnetic material (*9*), an incremental scale (*10*), and an optical head with a displacement read-out unit (*11*). Since PC is the heart of the stage, this work describes it first, and the relevance of other parts is discussed in greater detail further in the thesis. To begin with, axially polarised ceramics PZT-401 (Morgan Advanced Materials) was employed. The dimensions of the piezocylinder were as follows: the outer diameter (*OD*) – Ø32 mm, the inner diameter (*ID*) – Ø28 mm, the height (*H*) – 14 mm. The element is schematically depicted in Fig. 2.2. PZT-401 is an all-round hard piezoelectric material, capable of producing large displacement amplitudes while maintaining low mechanical and dielectric losses. It is characterised by long-lasting stability, high Curie temperature, coupling and mechanical quality factors. In addition, it can be used under constant and periodic excitation conditions; this makes it ideal for the piezoelectric stage. Typical applications include high-power transmitters, medical transducers, different sensor types (e.g. level, flow, NDT), and so on [108–109]. The main properties of the used piezoceramics are summarised and listed in Appendix B.

Operation principle

The operation principle of the newly designed piezoelectric rotary stage is explained referring to Fig. 2.3. A combined tangential-axial vibration mode of the

PC is used to generate rotor motion and achieve the desired dynamic properties of the device. This vibration mode was selected as the most suitable one for generating symmetrical elliptical motion trajectory of the contact zone elements (Fig. 2.3b). On the contrary to the conventional unsymmetrical ('egg-like') trajectory, the adopted vibration mode provides no displacement of the neutral axis of the PC. This behaviour is determined by the topology of the sectioned electrodes (see Fig. 2.3a).

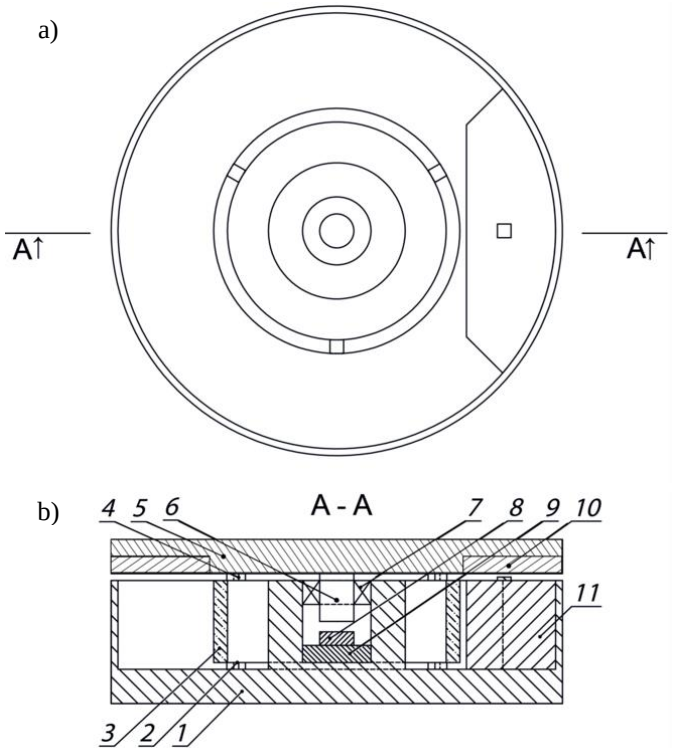

Fig. 2.1. The design of conceptual high-resolution piezoelectric rotary stage: a) top view (rotor is not shown); b) cross-sectional front view (rotor is shown). Parts: 1 – housing; 2 – supporting base elements (three units); 3 – piezocylinder; 4 – contact zone elements (three units); 5 – rotor; 6 – rotor shaft; 7 – precise bearing; 8 – magnet; 9 – non-magnetic material; 10 – incremental scale; 11 – optical head with a displacement read-out unit

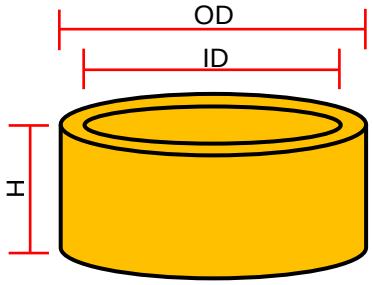

Fig. 2.2. A schematic depiction of the piezocylinder (OD/ID – outer/inner diameter, H – height)

The application of a single-phase high frequency electrical signal *Ucos(ωt)* via signal amplifiers to the given configuration of wiring connecting one group of three electrodes leads to the generation of standing-wave-type vibrations in the PC. The latter part is positioned on three equally spaced supporting base elements (see Fig. 2.1) firmly attached to the housing. The top surface of the PC is in contact with the rotor via three contact zone elements located in one plane and displaced equally with respect to the axis of rotation (Z direction). The rotational motion of the piezoelectric stage is initiated by the friction force acting between the contact zone elements and the rotor. The rotor shaft is rigidly mounted in precise ball bearing centring the rotor in a plane perpendicular to its rotational axis. A presence of neodymium magnet ensures a sufficient, even and constant pulling force between the housing and the rotor. Moreover, the magnet ensures the rotor to be centred with respect to its axis of rotation. This combination of the bearing and the magnet enables the required balance of both radial and axial load, resulting in uniform rotational motion. If another three electrodes are excited, the direction of rotational motion is reversed. Since travelling-wave vibrations are not exploited in this drive, the overall system design and structure becomes much simpler, because additional components associated with phase shifting of electrical signal are not necessary. In such a way, the potentially induced motion errors of the rotor are eliminated. The angular position of the rotor is determined by the optical encoder consisting of the glass-chromium incremental scale attached to the rotor, and a miniature optical reflection-based head with a displacement read-out unit fixed to the housing.

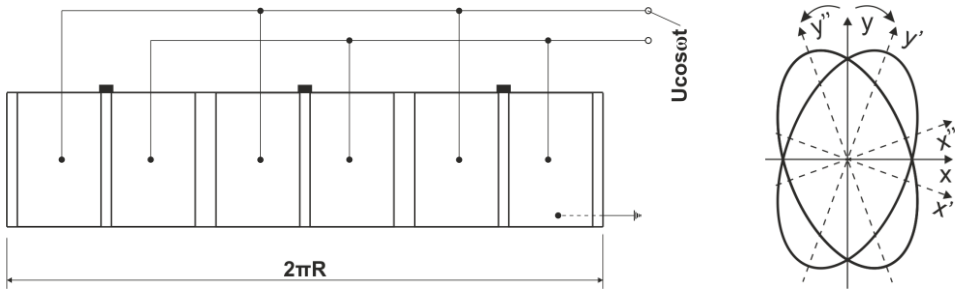

Fig. 2.3. A layout of the piezocylinder with sectioned electrodes (R – the external radius of a piezocylinder) (a) and induced symmetrical elliptical radial resonant oscillations of each contact zone element (b)

2.2. A geometric model of the piezoelectric stage

This section aims at providing some supplementary visual information meant to support the design of the rotary piezostage and its operation presented above. Therefore, the emphasis is placed on the generation of geometric model of the stage, with its major structural components described afterwards.

A virtual model of the proposed object was designed by using a commercial parasolid-based software SolidWorks applied in many engineering fields [110–111].

An enlarged assembly view of the designed piezoelectric rotary stage is given in Fig. 2.4. The dimensions of the actuator are Ø66 × 25 mm. The major structural

components are listed below, providing a short description of each part, including the size, role, and the motivation behind material selection.

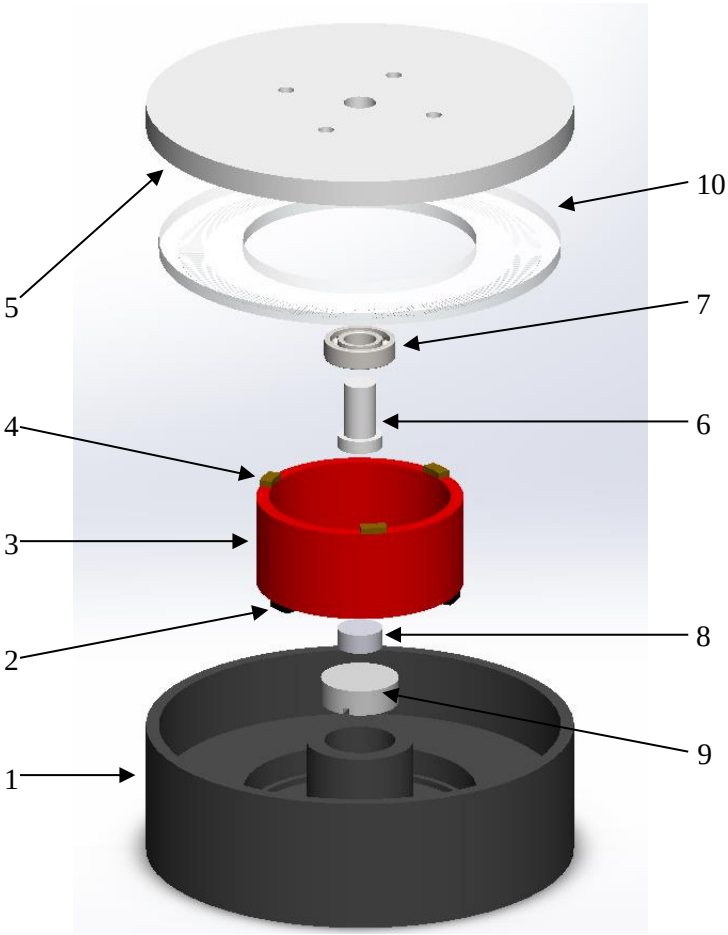

Fig. 2.4. An enlarged assembly view of the designed high-resolution piezoelectric rotary stage with indicated major parts: 1 – housing; 2 – supporting base elements (three units); 3 – piezocylinder; 4 – contact zone elements (three units); 5 – rotor; 6 – rotor shaft; 7 – precise bearing; 8 – magnet; 9 – non-magnetic material; 10 – incremental scale

1) Housing

The housing (Ø66 × 18 mm) is a cylindrical structure, on which all other system components rest. At the same time, it protects the internally located elements of the piezoelectric stage from external environmental effects. Anodised aluminium was selected for housing, since it is sufficiently strong light-weight material featured by significantly increased corrosion resistance, very low electrical and magnetic conductivity, easy machinability, and a variety of surface colours [112–114].

2) Supporting base elements

Three units of customized rectangular (4 × 2 × 2 mm^3) soft rubber characterised by high grip, damping and shock-absorbing were selected to act as

supporting elements between the piezocylinder and the housing. Furthermore, rubber is a strong dielectric, which makes it highly compatible with piezoceramics and anodised aluminium.

3) Piezocylinder

Piezoceramics PZT-401 (Ø32 × Ø28 × 14 mm) was chosen for the designed piezoelectric stage. More information about selection of the material was given in Section 2.1.

4) Contact zone elements

These are the essential components for generating sufficiently high friction between the PC and the rotor so that the latter part could receive oscillations transmittable from the piezocylinder, and exhibit the desired angular motion. This is ensured by combining three units of customized rectangular (4 × 2 × 1 mm^3) frictional material. Considering the reasons for the selection of material, sintered ceramics (composition of clay and porcelain bonded to copper flakes and filaments) was chosen as the best option. The same material can be found in many cars, where it is employed as a pad in the braking system.

5) Rotor

The rotor (Ø66 × 5 mm) functions as an output link of the piezoelectric stage and protects the internal constituents from external environmental effects. So as to transfer mechanical energy from the contact zone elements to the rotor, a constant and continuous interaction between these structural parts has to be ensured. For this reason, a sufficient pressing force has to be maintained, which requires a sufficient weight of the rotor. Consequently, the rotor was designed to be made of austenitic stainless steel, as it is very suitable for parts which are extensively exposed to abrasion and friction. Such properties as high Young's modulus, yield stress, tensile strength, low electrical and magnetic conductivity and easy processing make it particularly attractive and suitable for the given purpose [112, 115–116].

6) Rotor shaft

The rotor shaft (Ø5 × 11 mm) was designed to be made of the same steel as the rotor. The purpose of the shaft is to keep the rotor stable and centred with respect to its rotational axis and the plane perpendicular to it. This is achieved by the interaction of the shaft with the precise bearing and the magnet.

7) Precise bearing

As it was explained before, the precise ball bearing is applied to keep the shaft rigidly mounted and prevent from unnecessary motion in the direction perpendicular to the axis of shaft rotation. For this reason, the miniature (Ø10 × Ø5 × 4 mm) SKF bearing (type WBB1-8705-2RZ) made of stainless steel was chosen.

8) Magnet

The presence of the disc-shaped magnet ensures a sufficient and constant pulling force between the housing and the rotor. The magnet causes the rotor to be centred with respect to its rotational axis. In order to implement that, a neodymium magnet (Ø6 × 3 mm, grade N42) was employed.

9) Non-magnetic material

The piezoelectric stage also includes a screwed piece of disc-shaped (Ø12 × 4 mm) non-magnetic material to which the magnet is immovably and permanently

attached. By using a fine-adjustment screw, it is possible to adjust the gap between the magnet and the rotor shaft in order to increase/decrease the resulting pulling force. Referring to the application, austenitic stainless steel was selected, particularly because of the favourable material characteristics listed above.

10) Incremental scale

The primary goal of the incremental scale is to precisely and accurately register the angular displacement of a rotor. High-resolution periodic microstructure and very high reflection index of chromium rasters (optical reflection read-out principle is used) are two of the main challenges to be considered carefully. A well-known chromium-on-glass grating scale (Ø64 × Ø32 × 4 mm, period of 80 μm) was selected for this task, since it fully meets the mentioned criteria. In addition, the scale can be easily attached to the rotor. However, the cost-performance ratio of such scale is high, thus, being a significant limitation. That is why UV-casted polyethylene terephthalate (PET) substrates coated by acrylic photopolymer and aluminium are a very promising alternative which is considered and presented in this thesis as well (see Chapter 4).

It should be pointed out that since this section mainly deals with the piezoelectric stage from the mechanical point of view, electronic elements were not included in the figures and structural components description, provided above. Despite this fact, a miniature optical head with a displacement read-out unit (AEDR-8400, 3 × 3.2 × 1.3 mm^3) fixed to the housing plays a very significant role in determining the angular position of the rotor, data processing, etc. More details regarding the latter sub-system are given in Chapter 3 and Chapter 5.

2.3. A computational model of the piezocylinder

After creating the geometric model of the analysed object, the design process continues. The next step is to create a computational model of the piezocylinder and perform finite element (FE) analysis acting as the basis for corresponding experimental investigation explicitly discussed in the next chapter of this dissertation. If there is a match between the numerical and the experimental research results, it is proven that the generated FE model is suitable for solving dynamics-related problems of similar systems.

In this subchapter, harmonic and modal analyses of the piezocylinder are discussed, followed by a description of the effect of voltage on both displacements and motion trajectories of the contact zones of the PC.

Modelling steps in finite element analysis

The following steps were taken during FE modelling of the PC: 1) geometry development; 2) material and its properties assignment; 3) imposition of boundary and loading conditions; 4) mesh generation; 5) running analysis; 6) plotting the static or dynamic solution.

The FE analysis of the PC was executed using a versatile simulation software ANSYS which is widely applied in various areas of engineering [117–120].

The finite element method was employed to perform frequency response and modal analyses. In the initial step, a mathematical model evaluating the coupled

mechanical and electrical behaviour of the actuator was constructed. The basic dynamic equation for the piezocylinder is derived from the principle of minimum potential energy, piezoelectric equations, and can be written as [121]:

$$\begin{cases} [\mathbf{M}]\{\ddot{\mathbf{u}}\} + [\mathbf{C}]\{\dot{\mathbf{u}}\} + [\mathbf{K}]\{\mathbf{u}\} + [\mathbf{T_1}]\{\boldsymbol{\phi}_\mathbf{1}\} + [\mathbf{T_2}]\{\boldsymbol{\phi}_\mathbf{2}\} = \{\mathbf{F}\} \\ [\mathbf{T_1}]^{\mathbf{T}}\{\mathbf{u}\} - [\mathbf{S_{11}}]\{\boldsymbol{\phi}_\mathbf{1}\} - [\mathbf{S_{12}}]\{\boldsymbol{\phi}_\mathbf{2}\} = \{\mathbf{Q_1}\} \\ [\mathbf{T_2}]^{\mathbf{T}}\{\mathbf{u}\} - [\mathbf{S_{12}}]^{\mathbf{T}}\{\boldsymbol{\phi}_\mathbf{1}\} - [\mathbf{S_{22}}]\{\boldsymbol{\phi}_\mathbf{2}\} = \{\mathbf{0}\} \end{cases}; \quad (7)$$

here $[\mathbf{M}]$, $[\mathbf{K}]$, $[\mathbf{T}]$, $[\mathbf{S}]$ and $[\mathbf{C}]$ are the matrices of mass, stiffness, electroelasticity, capacity and damping, respectively, $\{\mathbf{u}\}$, $\{\mathbf{F}\}$, $\{\mathbf{Q_1}\}$ are the vectors of structural displacement nodes, external mechanical forces and charges coupled with the electrodes, respectively, and $\{\boldsymbol{\phi}_\mathbf{1}\}$, $\{\boldsymbol{\phi}_\mathbf{2}\}$ are the vectors of nodal potentials of the nodes associated with the electrodes. Index *1* denotes the electrodes connected to the signal generator. Index *2* denotes the free electrodes. The values of $\{\boldsymbol{\phi}_\mathbf{1}\}$ are known from the signal generator.

The natural frequencies and modal shapes of the piezocylinder are derived from the system solution which is expressed as [121]:

$$\det([\mathbf{K}^*] - \omega^2[\mathbf{M}]) = \{\mathbf{0}\}; \quad (8)$$

here $[\mathbf{K}^*]$ is the modified stiffness matrix, and ω is the natural frequency. In the analysed case, the modified stiffness matrix takes the following form [121]:

$$[\mathbf{K}^*] = [\mathbf{K}] + [\mathbf{T_2}]\left[\mathbf{S_{22}^{-1}}\right][\mathbf{T_2}]^{\mathbf{T}}. \quad (9)$$

To perform the actual analysis, the PC was divided into finite elements (Fig. 2.5). The model consists of piezoelectric hexahedral (brick) elements SOLID5; each element has 8 nodes, with each node having 6 DOF (i.e. translation in X, Y and Z directions and rotation about X, Y and Z axes) and electrical potential.

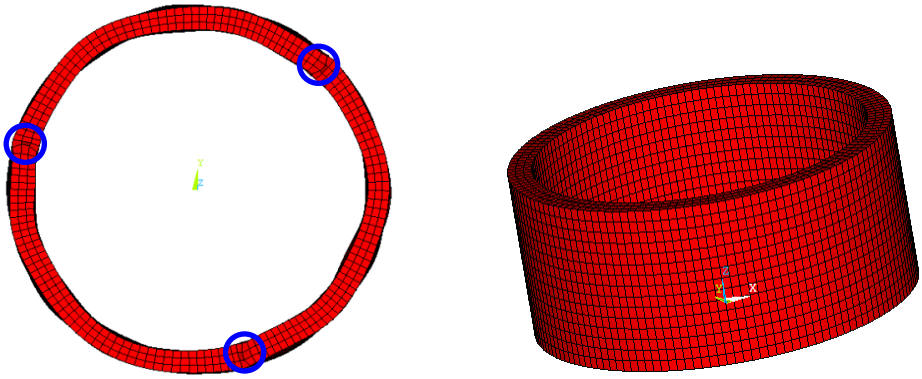

a) b)

Fig. 2.5. The finite element model of the analysed piezocylinder: a) fixed locations (at the bottom) representing imposed mechanical boundary conditions; b) isometric view

The mechanical displacements of fixed surfaces of the PC are equal to zero. These surfaces denote the locations of three equally displaced supporting base

elements (Fig. 2.5a), with each location coinciding with the intersection of two adjacent electrodes.The electric charges of the piezocylinder, which are not coupled with electrodes, are also equal to zero (i.e. the electrical boundary conditions were defined by the second and the third formula in Eq. (7)). The layout of electrodes corresponds to the topology shown in Fig. 2.3a. This represents the imposed boundary conditions. Damping applied in the given model was defined by the constant structural damping coefficient determined by material properties of the selected piezoceramics (i.e. an evaluation of the damping based on experimental dynamic characteristics of the PC is very complicated due to high frequency excitation signal inducing necessary vibration modes of higher orders which, in turn, lead to the displacement of the piezocylinder in three spatial directions).

2.3.1. Evaluation of resonant frequencies and vibration modes

In this study, harmonic analysis was conducted to check the dynamic behaviour of the piezocylinder within the range of 100–140 kHz. The investigated PC was subjected to cosinusoidal voltage of 60 V (peak-peak) in this case, as it is an intermediate level value for the used piezoceramics. The obtained amplitude-frequency plot is revealed in Fig. 2.6. It denotes the displacements of centres of the contact zones (see *A*–*C* in Fig. 2.8) and thus, the contact zone elements, in X (tangential), Y (radial), and Z (axial) directions. According to the constructed plot, the vibrations in the axial direction dominate in the entire frequency range. This represents an expected and desired tendency. The respective maximal displacement amplitude (*Az*) is registered at approximately 128.8 kHz. Nevertheless, the following aspects should be reminded and taken into consideration before choosing the operational resonant frequency for the designed piezoelectric rotary stage.

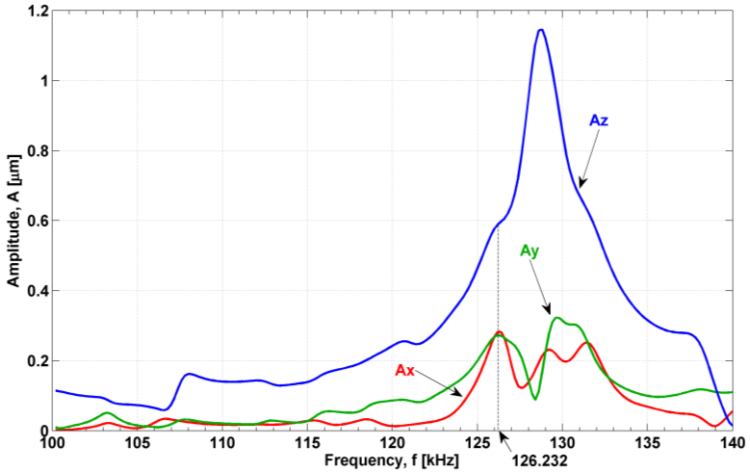

Fig. 2.6. Frequency response of piezocylinder, with denoted displacements of centres of the contact zones in different directions

1. Rotational motion generated by the piezocylinder has to be caused by oscillations in both axial and tangential directions, so the corresponding displacement amplitudes have to be as high as possible.

2. A suitable vibration mode does not necessarily correlate only with the maximal amplitudes of displacement.

3. Significant changes in frequency response curves commonly indicate such vibration modes which could possibly be used to generate uniform motion of the rotor.

Evaluating the plot more carefully, it can be observed that there is a need to analyse the range between 124 kHz and 134 kHz, showing potential operational frequency interval. Thus, in the second step, harmonic analysis plot is formed (Fig. 2.7), where three intervals denote the most characteristic changes in each curve, which were determined based on the three previously disclosed aspects. In the first interval (125.8–126.6 kHz), tangential displacement amplitudes (*Ax*) are slightly higher than those in the radial direction (*Ay*). The maximal values are 0.28 µm and 0.27 µm, respectively. A corresponding *Az* value is equal to 0.59 µm. It should be noted that *Ax* values in this range are the highest compared to the ones in the second and third intervals. The second interval should be split into two parts, i.e. 128.4–128.9 kHz and 129–129.4 kHz, with the tangential vibrations prevailing over the radial ones in the first interval; here the maximal values of *Ax*, *Ay* and *Az* reach 0.23 µm, 0.17 µm and 1.15 µm, respectively. The radial vibrations dominate over the tangential ones in the second part, so it is not very meaningful for further analysis. Similarly, in the third interval, there is also a difference between two sub-ranges, where 131–131.4 kHz range is treated as irrelevant due to the same reason as mentioned before, while the range of 131.5–132 kHz features a proper dynamic behaviour, with the highest values of *Ax*, *Ay* and *Az* being 0.25 µm, 0.24 µm, and 0.62 µm, accordingly.

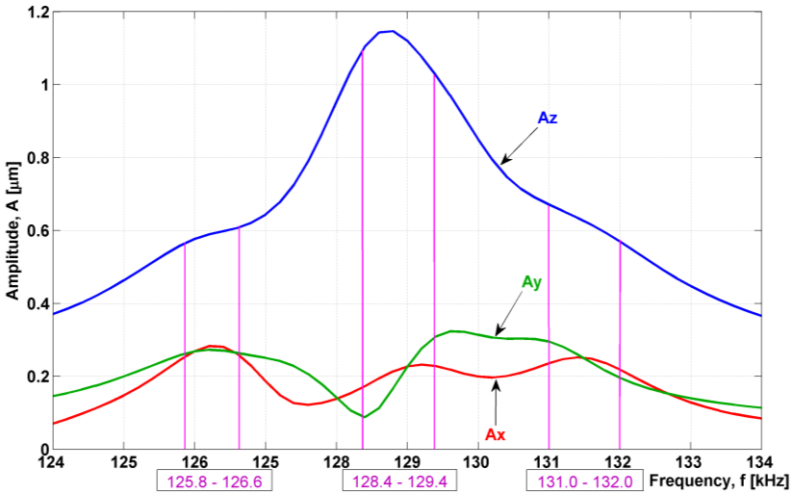

Fig. 2.7. Frequency response of the piezocylinder, with denoted displacements of centres of the contact zones in different directions within three potential operational frequency intervals: 1) 125.8–126.6 kHz; 2) 128.4–129.4 kHz; 3) 131–132 kHz

Taking into account the primary results of frequency response analysis, it is obvious that the potential operational frequency can lie in any of all three

characteristic intervals, which raises a demand for further investigation. To fulfil this requirement, modal analysis was conducted. It allowed to determine the exact resonant frequencies and the associated vibration modes. The most important result is given in Fig. 2.8 showing the vibration mode of the PC at 60 V in the axial direction, when the resonant frequency is 126.23 kHz (the range of 125.8–126.6 kHz). The latter direction represents the most characteristic displacement of the structure. This vibration mode results in three regular equally displaced zones (*A*–*C*) at the top surface, where the maximal positive displacements appear. By analogy, similar zones (*D*–*F*) displaced approximately by 60° are indicated at the bottom surface. They define the areas subjected to the maximal negative displacements. The minimal displacement occurs in the middle part of the PC with respect to its height. The resulting topology of displacement fields should lead to uniform motion of the rotor and thus, a successful operation of the rotary piezostage to be developed.

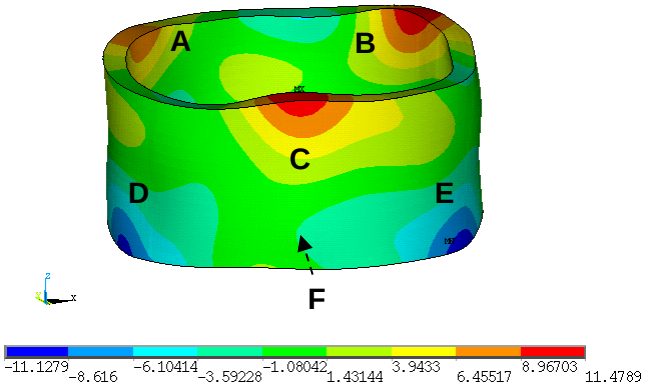

Fig. 2.8. Axial displacement of the piezocylinder (modal analysis) caused by the vibration mode at resonant frequency of 126.23 kHz (125.8–126.6 kHz interval; U = 60 V)

In the examined range of 128.4–129.4, there were three vibration modes found (128.61 kHz, 128.67 kHz and 128.78 kHz), with one mode (128.67 kHz) obtained in the range of 131–132 kHz (see Appendix C). However, all of them cause irregular distribution of the *A*–*C* and *D*–*F* zones. Hence, due to the exhibited behaviour, they are unacceptable for generating the rotor motion.

In order to verify this choice, it was necessary to calculate the domination coefficients. They enable one to identify the prevalent oscillation type (e.g., tangential, radial, axial, etc.) in a piezoactuator and distinguish the vibration modes more accurately. Generally, the need to determine the coefficients is caused by a tendency for the piezocylinder of the same geometry but different dimensions to attain a varying distribution of vibration modes with respect to a range of resonant frequencies commonly sorted in the ascending order. Sometimes the situation becomes even more complicated because domains of different frequencies overlap.

A solution to the indicated problem was proposed by Lithuanian scientists [121]. Assuming that the resonant frequencies and vibration modes of a piezoactuator have been calculated, the following sums can be formed for the n-th resonant frequency [121–122]:

$$S_{\tau}^{n} = \sum_{i=1}^{r}(A_{i\tau}^{n})^{2}, \quad (10)$$

$$S_{\phi}^{n} = \sum_{i=1}^{r}\left(A_{i\phi}^{n}\right)^{2}, \quad (11)$$

$$S_{\zeta}^{n} = \sum_{i=1}^{r}\left(A_{i\zeta}^{n}\right)^{2}, \quad (12)$$

$$r = \frac{l}{k}; \quad (13)$$

here $k = \tau, \phi, \zeta$ is the number of DOF in a node, l is the number DOF of nodes in the model, r is the size of vector of the vibration mode for the k-th coordinate, A_{ik}^{n} is the value of a vector of the vibration mode of the i-th element. Then the following ratios can be formulated [121–122]:

$$s_{\tau}^{n} = \frac{S_{\tau}^{n}}{S_{\tau}^{n}+S_{\phi}^{n}+S_{\zeta}^{n}}, \quad (14)$$

$$s_{\phi}^{n} = \frac{S_{\phi}^{n}}{S_{\tau}^{n}+S_{\phi}^{n}+S_{\zeta}^{n}}, \quad (15)$$

$$s_{\zeta}^{n} = \frac{S_{\zeta}^{n}}{S_{\tau}^{n}+S_{\phi}^{n}+S_{\zeta}^{n}}; \quad (16)$$

here s_{τ}^{n}, s_{ϕ}^{n}, s_{ζ}^{n} are the oscillation energy ratios of the n-th resonant frequency in the τ, ϕ and ζ coordinate directions, and S_{ζ}^{n}, S_{ϕ}^{n}, S_{ζ}^{n} are the oscillation energies of the n-th resonant frequency in the k-th direction.

s_{τ}^{n}, s_{ϕ}^{n} and s_{ζ}^{n} are also called partial domination coefficients, since they estimate the energy only in two coordinate directions. These coefficients have several drawbacks. Firstly, they are not normalised, so their values vary from zero to infinity. Secondly, there are six coefficients in the three-dimensional case, which makes the analysis very difficult.

To avoid the described issue, a change in algorithm was applied, according to which, it is necessary to find the sum of vibration amplitude squares of the piezoactuator in all directions with respect to DOF of a point, i.e. the overall energy of a system in all directions. Then the respective ratios become [121–122]:

$$s_{\tau}^{n} = \frac{S_{\tau}^{n}}{\sum_{i=1}^{k} s_{i}^{n}}, \quad (17)$$

$$s_{\phi}^{n} = \frac{S_{\phi}^{n}}{\sum_{i=1}^{k} s_{i}^{n}}, \quad (18)$$

$$s_{\zeta}^{n} = \frac{S_{\zeta}^{n}}{\sum_{i=1}^{k} s_{i}^{n}}; \quad (19)$$

here $s_{j}^{n}(j = \tau, \phi, \zeta)$ is the oscillation domination coefficient corresponding to the n-th vibration mode. The index j indicates the direction in which the vibration energy is the highest during analysis. j can be expressed in terms of notations written before (τ, ϕ, ζ), or any other symbols, including numbers (e.g., 1, 2 and 3), to stand for X,

Y, and Z directions. These coefficients are normalized, so their values vary within the range between zero and one. Therefore, a comparative investigation is easy to perform.

During the executed numerical study, the domination coefficients were calculated for the chosen vibration mode. It was determined that s_τ = 0.562, s_ϕ = 0.197, and s_ζ = 0.241. These results imply that the analysed PC mostly vibrates in the tangential and axial directions (i.e. coefficients are the highest) which coincide with the directions governing a well-defined and uniform rotational motion of the piezoelectric rotary stage. The results confirm that the resonant frequency and vibration mode (and thus, geometry) of the piezocylinder were selected correctly.

2.3.2. An evaluation of surface displacement

After the previously conducted studies of the piezocylinder, the evaluation of its surface displacement was performed using additional harmonic analysis in order to realise how the surface of the examined object is affected in different directions under the influence of operational resonant frequency. The view of the total displacement of the analysed PC subjected to harmonic electrical excitation signal (60 V) of 126.23 kHz is provided in Fig. 2.9; the top surface is divided into three nearly even in shape maximal displacement zones (*A*–*C*), on which the contact zone elements should be attached. When affected by induced vibrations, they should move in an elliptical trajectory and generate the motion of the rotor. The displacement of the middle zone with respect to the height of the piezocylinder is negligible. Meanwhile, the bottom surface is mostly displaced in three zones (*D*–*F*) similar in shapes and amplitudes to the ones observed at the top surface but slightly different in displacement locations. The latter phenomenon can be explained by the imposed mechanical boundary conditions (see Fig. 2.5). In the case of no constrains, the zones at both the top and bottom surfaces would be identical.

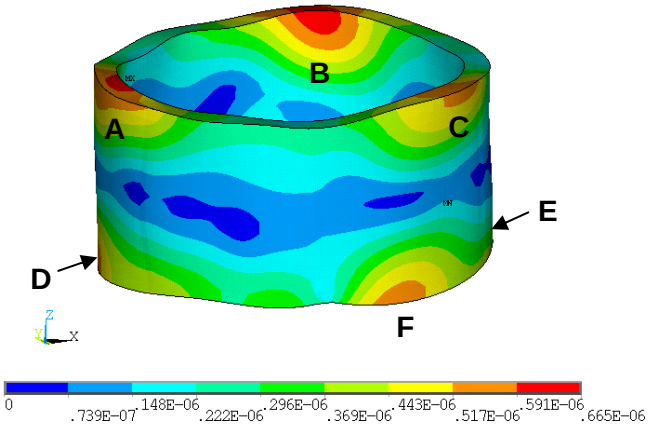

Fig. 2.9. The total displacement of the piezocylinder (harmonic analysis) caused by vibration mode at resonant frequency of 126.23 kHz (U = 60 V)

Displacement of the PC in the tangential, radial, and axial directions is provided in Appendix C. The zones of tangential and radial displacement are

distributed similarly, i.e. three highest positive displacement zones are registered at the top and bottom surfaces; the two maximal negative displacement areas are located at the top and bottom surfaces, with one zone at each surface, accordingly. In the case of axial displacement, the so called ‘pattern of three zones’ takes the most obvious form, with the three regularly distributed peak zones of positive displacement at the top surface, and three peak zones featured by negative displacement at the bottom surface. The axial vibrations prevail when compared to the ones in two other directions. The middle-region pattern indicates the lowest displacement of the PC in all inspected directions.

Another part of the evaluation of surface displacement is intended to ascertain what influence the applied voltage has on the displacements of the contact zones in different spatial directions. For that reason, the amplitude-frequency characteristics in tangential, radial and axial directions were obtained (Fig. 2.10) at the operational resonant frequency of 126.23 kHz. A general tendency for the amplitudes to increase with a rise of applied voltage is observed. The average increase rate is equal to 0.005 μm/V with respect to the tangential and radial directions and 0.01 μm/V with respect to the axial direction. It is also observed that the amplitudes attain the values of 0.28 μm, 0.27 μm, and 0.59 μm, respectively, at the operational voltage (60 V) in the mentioned directions. Similar differences in the amplitudes are noted under the effect of other values of the driving voltage. The maximal voltage amplitude of 80 V was chosen so as not to induce the overheating phenomenon in piezoceramics. It can be stated that an increase in driving voltage leads to linear rise in displacements of the contact zones. It should also be noted that there is a minor difference between the tangential and radial displacements at the same frequency and different voltage. However, the tangential displacements are slightly higher than the radial ones. The maximal displacements are registered in the axial direction. These results confirm the outcome of the modal analysis described earlier in this chapter, i.e. the investigated object vibrates most intensively in the tangential and axial directions.

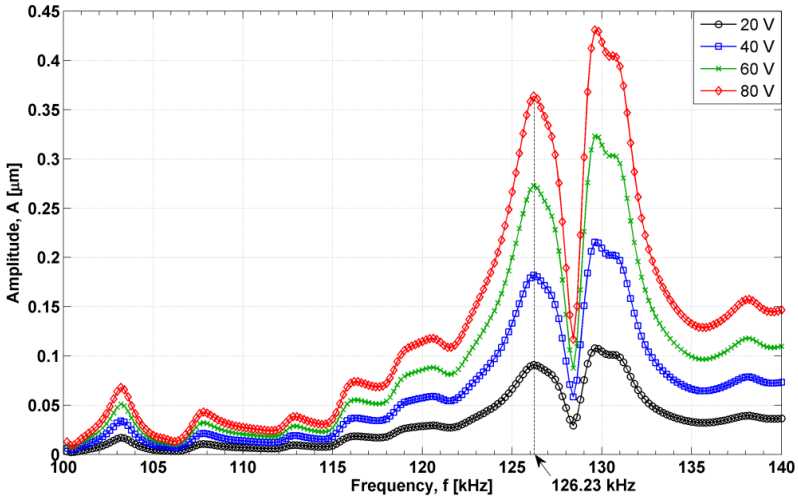

a)

b)

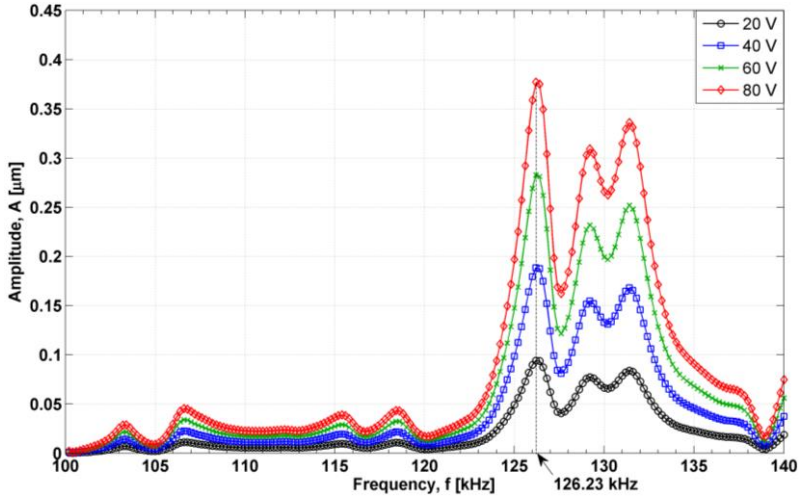

c)

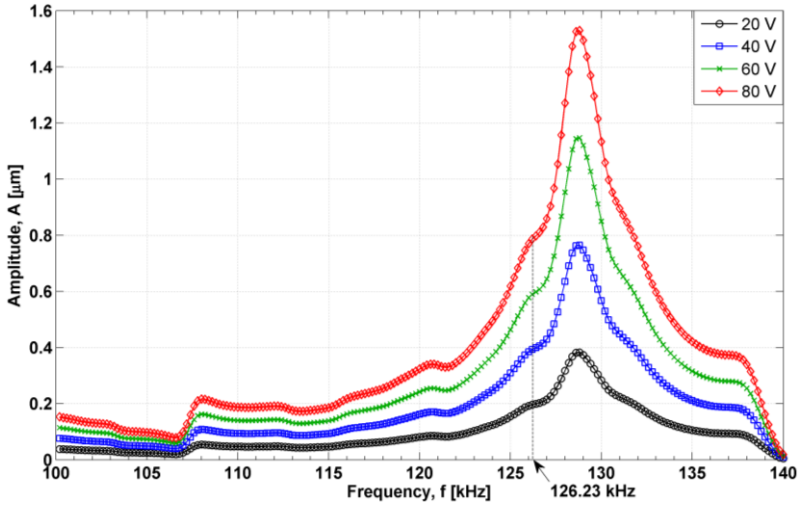

Fig. 2.10. Amplitude-frequency characteristics of the piezocylinder showing the influence of applied voltage on the displacements of contact zones in tangential (a), radial (b) and axial (c) directions (f_{res} = 126.23 kHz)

2.3.3. An evaluation of vibrational motion trajectories of contact zones

An elliptical motion trajectory is a well-known distinct feature of standing- and travelling-wave ultrasonic resonant-type motors and drives. If a shape of ellipse is regular, the motion of a rotor is uniform and can be used for various positioning applications. On the other hand, when the latter shape is distorted, the top surface of the piezocylinder is inappropriately deformed, causing irregular motion of the contact zones and thus, the rotor. This plays a very meaningful role when evaluating the dynamic properties of the system. Taking that into consideration, it was decided to examine the chosen PC in terms of generated vibrational motion trajectories of the contact zones in all XYZ planes. In addition, the influence of voltage amplitude on

the motion trajectory in each case was disclosed. As in the previously conducted investigations, the PC was subjected to harmonic electrical excitation signal at the operational frequency of 126.23 kHz. In Fig. 2.11a, the plot showing motion trajectories in XY plane is given. The obtained shapes of all curves in this plot are elliptical but quite contracted. Such tendency appears due to the dominating vibrations in the tangential direction. 0.09 µm (20 V) and 0.38 µm (80 V) are the lowest and the highest values of displacement amplitude in the latter direction, correspondingly. 0.09 µm and 0.36 µm are the respective amplitudes in the radial direction. Motion trajectories in the YZ plane are presented in Fig. 2.11b. Here the shapes of the curves become even more extended, which is caused mainly by the prevalent oscillations in the axial direction. The minimal and maximal amplitudes attributed to the axial direction are 0.2 µm (20 V) and 0.79 µm (80 V), respectively.

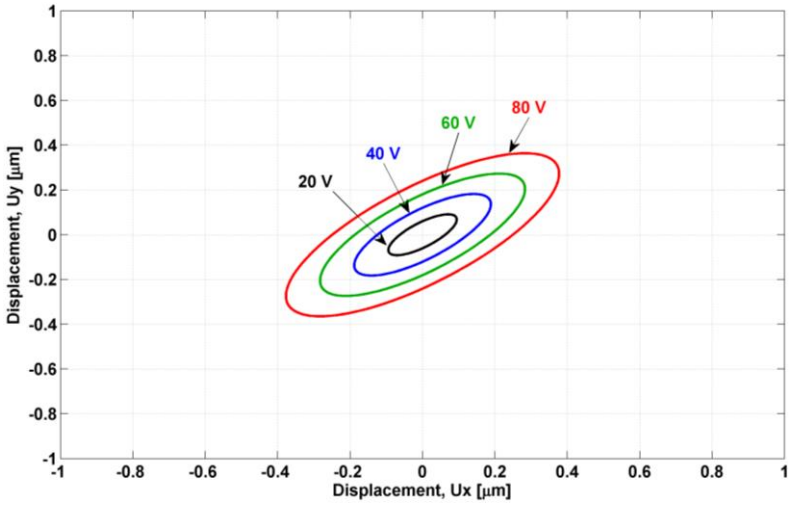

a)

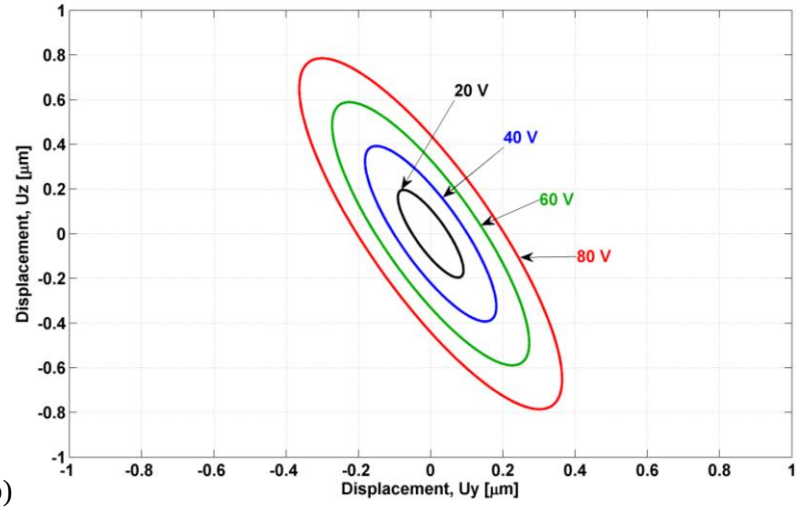

b)

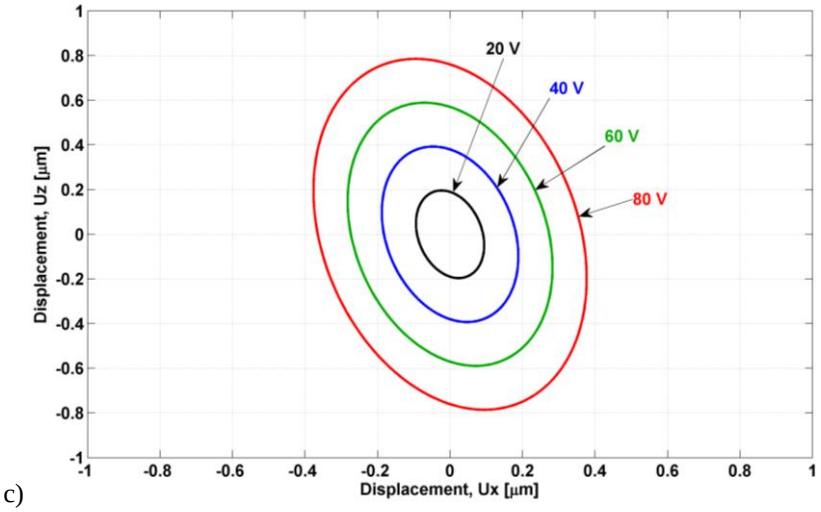

c)

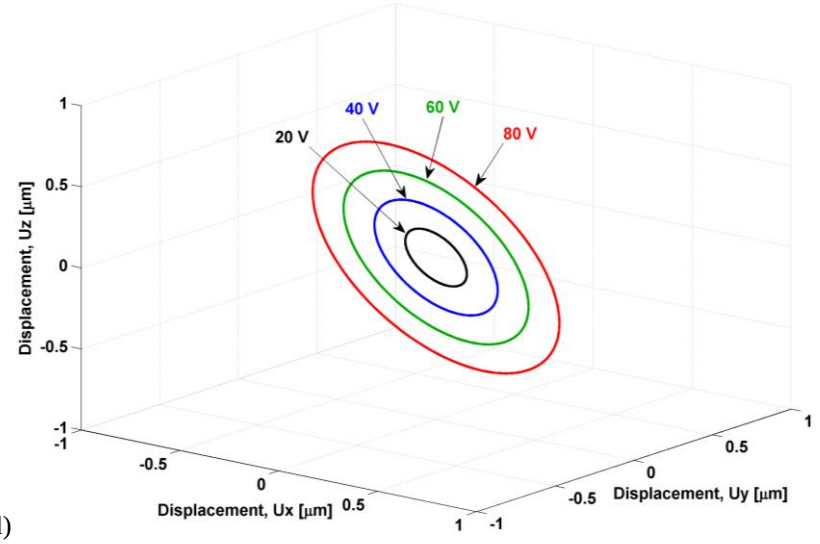

d)

Fig. 2.11. The relationship between applied voltage amplitude and motion trajectories of contact zones of the piezocylinder in XY (a), YZ (b) and XZ (c) planes and the 3D space (d)

Table 2.1 summarises all maximal displacement amplitude values. Fig. 2.11c presents the vibrational motion trajectories in the XZ plane. As explained in Section 2.3.2, tangential and axial oscillations contribute to the formation of the highest displacements. Therefore, the appropriate trajectories are defined by the most regular elliptical shape, leading to the generation of the most uniform motion of both the contact zones (and thus, the contact zone elements) and the rotor. In order to visualise better, all obtained resultant motion trajectories are provided in 3D space (Fig. 2.11d). Considering the constructed plots and results of the previously conducted numerical studies, it can be stated that the value of the adopted resonant frequency can be confirmed as suitable for application in the designed piezoelectric stage.

Table 2.1. The amplitude values of maximal displacement of contact zones under the effect of applied voltage

	20 V	40 V	60 V	80 V
X direction	0.09 μm	0.19 μm	0.28 μm	0.38 μm
Y direction	0.09 μm	0.18 μm	0.27 μm	0.36 μm
Z direction	0.20 μm	0.39 μm	0.59 μm	0.79 μm

The analysis of the influence of the applied voltage amplitude on the motion trajectories revealed the same tendency as the previous section, i.e. an increase in electrical potential initiates higher displacement amplitudes; that, in turn, provides more extended in shape elliptical motion trajectories of the contact zones.

2.4. A mathematical model of interaction between the piezocylinder and the rotor

In order to understand how the oscillations induced within the excited PC are transmitted to the rotor, a mathematical model describing the contact between these two structural elements has been developed and is presented further.

A lumped-parameter model defined by five DOF and representing the interaction between the PC with contact zone element (*1*) and the rotor (*2*) is depicted in Fig. 2.12. The contact zone element of the piezocylinder performs a forced motion in two orthogonal directions, causing the rotor to move in the clockwise or opposite direction. The two corresponding positions (points) of the interacting components are denoted as $A_1(x_1, y_1)$ and $A_2(x_2, y_2)$, where $x_1 = x_2 = x$; displacement of the rotor at the contact area in the normal direction is expressed as $v = l - y_2$.

It is assumed that the point of the rotor undergoes displacement in the tangential (u) and axial (v) directions when interacting with the contact zone element. The respective deformation forces acting on the PC and rotor are:

$$P_{y1} = m_1\ddot{y}_1 + H_{y_1}\dot{y}_1 + C_1 y_1 - B\cos(\omega t), \tag{20}$$

$$P_{y2} = H_{y_2}\dot{y}_2 + C_2(y_2 - l), \tag{21}$$

$$P_{x1} = m_1\ddot{x}_1 + H_{x_1}\dot{x}_1 + C_{x_1}x_1 - A\sin(\omega t), \tag{22}$$

$$P_{x2} = P_u = H_u\dot{u} + C_u u, \tag{23}$$

$$P_s = m_2\ddot{s} + D\dot{s}; \tag{24}$$

here m_1 is the mass of the piezocylinder with the contact zone element, m_2 is the mass of the rotor, H_{x_1} and H_{y_1} are the coefficients of viscous friction of the piezocylinder in the tangential and axial directions, respectively, H_u and H_{y_2} are the coefficients of viscous friction of the rotor in the tangential and axial directions, respectively, C_{x_1} and $C_1 = C_{y_1}$ are the coefficients of stiffness of the piezocylinder in the tangential and axial directions, respectively, C_u and $C_2 = C_{y_2}$ are the coefficients of stiffness of the rotor in the tangential and axial directions, respectively, $A\sin(\omega t)$ and $B\cos(\omega t)$ are the external (excitation) forces of the

piezocylinder, $\dot{s}$ is the velocity of the rotor, and $D\dot{s}$ is the force of resistance to the motion of the rotor. It should be noted that in the system of coordinates XOY, the equilibrium position of the piezocylinder with a contact zone element in the axial direction is observed, when $y_1 = 0$, and the respective position of the rotor is observed, when $y_2 = l$.

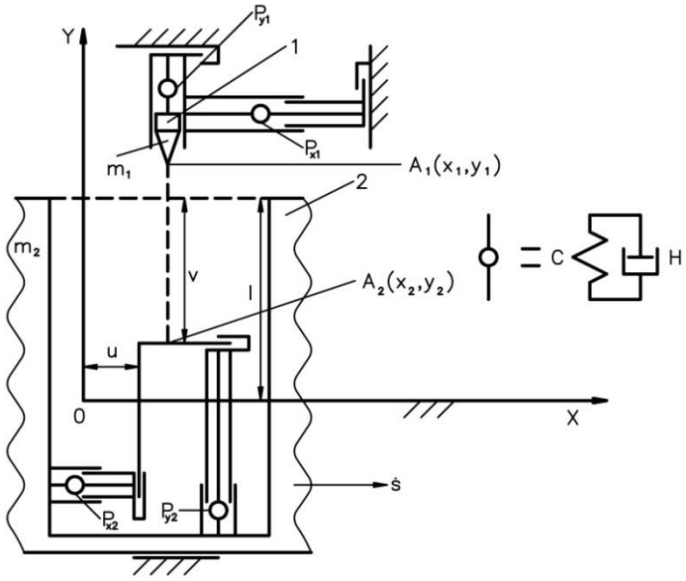

Fig. 2.12. Lumped-parameter model representing the interaction between the piezocylinder with a contact zone element (1) and the rotor (2)

The following substitutions of the terms are introduced so as to simplify the equations presented previously: $p^2 = \frac{C_1}{m_1}$, $\tau = pt$, $\dot{y}_1 = \frac{dy_1}{dt} = p\frac{dy_1}{d(pt)} = py_1'$, $\ddot{y}_1 = p^2y''$, $\dot{x}_1 = px_1'$, $\ddot{x}_1 = p^2x''$, $h_{y_1} = \frac{H_{y_1}}{\sqrt{m_1C_1}}$, $h_{y_2} = \frac{H_{y_2}}{\sqrt{m_1C_1}}$, $h_{x_1} = \frac{H_{x_1}}{\sqrt{m_1C_1}}$, $h_u = \frac{H_u}{\sqrt{m_1C_1}}$, $d = \frac{D}{\sqrt{m_1C_1}}$, $C_{21} = \frac{C_2}{C_1}$, $C_{x_11} = \frac{C_{x_1}}{C_1}$, $C_{u1} = \frac{C_u}{C_1}$, $\bar{P} = \frac{P}{C_1}$, $a = \frac{A}{C_1}$, $b = \frac{B}{C_1}$, $\mu = \frac{m_2}{m_1}$, $\nu = \frac{\omega}{p}$, and $T_\tau = \frac{2\pi}{\nu}$; here p and ω are the natural and angular frequencies of the piezocylinder, correspondingly. Then the Eq. (20–24) become:

$$\bar{P}_{y_1} = y_1'' + h_{y_1}y_1' + y_1 - b\cos(\nu t), \tag{25}$$

$$\bar{P}_{y_2} = h_{y_2}y_2' + C_{21}(y_2 - l), \tag{26}$$

$$\bar{P}_{x_1} = x_1'' + h_{x_1}x_1' + C_{x_11}x_1 - a\sin(\nu t), \tag{27}$$

$$\bar{P}_u = h_u u' + C_{u1}u, \tag{28}$$

$$\bar{P}_s = \mu s'' + ds'. \tag{29}$$

The following are the two cases describing the absence and presence of the interaction between the PC with a contact zone element and the rotor.

- Case 1 ($y_1 > y_2$)

In this case, the contact zone element does not interact with the rotor. Thus, the expressions of the forces take the forms: $\bar{P}_{y_1} = 0$, $\bar{P}_{y_2} = 0$, $\bar{P}_{x_1} = 0$, $\bar{P}_u = 0$, $\bar{P}_s = 0$.

- Case 2 ($y_1 = y_2$)

In this case, the contact zone element interacts with the rotor. Therefore, the following expressions are valid: $\bar{P}_{y_1} + \bar{P}_{y_2} = 0$, $\bar{P}_{x_1} + \bar{F}_f = 0$, $\bar{P}_u - \bar{F}_f = 0$, $\bar{P}_s - \bar{P}_u = 0$; here $\bar{F}_f$ is the friction force between the contact zone element and the rotor, and it is expressed as $\bar{F}_f = H_0|\bar{P}_{y_2}|\mathrm{sgn}(x' - (u' + s'))$. A more detailed form of the latter expression is provided further:

$$\bar{F}_f = \begin{cases} +H_0|\bar{P}_{y_2}|, when\ (x' - (u' + s')) > 0 \\ (-1, +1)\ \ H_0|\bar{P}_{y_2}|, when\ (x' - (u' + s')) = 0. \\ -H_0|\bar{P}_{y_2}|, when\ (x' - (u' + s')) < 0 \end{cases}$$

The obtained differential Eq. (25–29) were solved numerically by using the Newmark method, by means of software Borland C++ Builder 6, taking into account the expressions described in Case 2. The calculations were performed using such values of the relevant dimensionless parameters which would represent and characterise the real analysed system as much as possible: $h_{y_1} = h_{x_1} = 0.1$, $h_{y_2} = h_u = 0.1$, $C_{21} = 4$, $C_{x_1 1} = 1$, $C_{u1} = 4$, $\mu = 4$, $d = 0.1$, $a = b = 1$, $\nu = 1$; 1.25; 1.43, l = -0.8; 0; 0.8.

The responses of the analysed system were registered in the steady state of motion in the presence of varying excitation frequency of the piezocylinder (ν) and distance of the rotor from the equilibrium position in the axial direction (l). One of the most representative groups of the obtained responses is given below. In this case, resonant excitation frequency was applied, and the distance of the rotor from the equilibrium position was -0.8 (i.e. a small gap between the interacting parts). In order to provide a better understanding of the time-dependent plots (Fig. 2.13a–c), two periods of the respective motion in the negative (counter-clockwise) direction are shown. The positions of two contacting points in the axial direction versus time are observed in the first plot (a). In the beginning, the contact zone element of the piezocylinder moves according to the harmonic excitation law and does not interact with the rotor that stands still. Afterwards, interaction begins, and the contact zone element moves along with the rotor down and up in the axial direction due to respective deformation induced within the rotor. Then the contact zone element continues moving up (i.e. retraction takes place), while the rotor remaining at rest (i.e. equilibrium position) until the next repeated interaction. The second plot (b) illustrates the resulting corresponding tangential displacement of the rotor. When affected by the contact zone element, the rotor slightly moves forward because of acting friction force, which causes a little slip, and then moves backward due to acting sufficient deformation force in the normal direction. When the influence of this force decreases (i.e. due to specific motion trajectory of the contact zone element), a slip occurs, making the rotor slightly move forward again until the next repeated interaction. The third plot (c) shows the total angular displacement of the rotor versus time, and the last plot (d) provides the motion trajectory of the contact

zone element with in the tangential-axial plane. As it is observed, a nearly elliptical shape is formed, thus leading to a well-defined motion of the rotor.

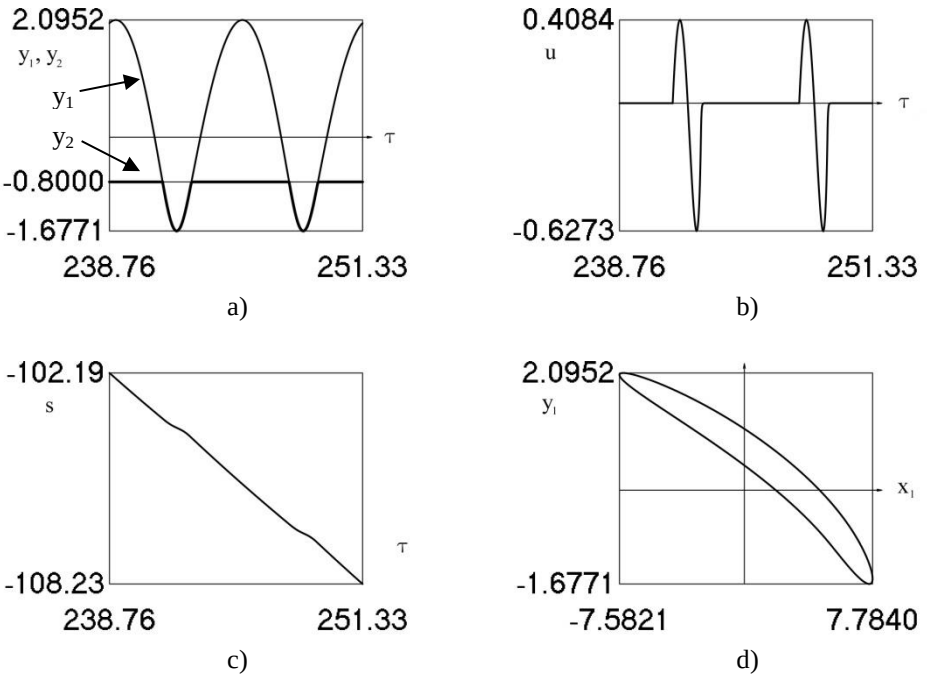

Fig. 2.13. Response characterising the interaction between the piezocylinder and the rotor via a contact zone element during steady state motions, when $\nu = 1$ and l = -0.8: a) the positions of two contacting points in the axial direction versus time; b) the tangential displacement of the rotor versus time; c) total angular displacement of the rotor versus time; d) the motion trajectory of the contact zone element in the tangential-axial plane

When comparing the described response with the other two ($l = 0$ and $l = 0.8$), it can be stated that the shorter distance (i.e. smaller gap) between the rotor and the contact zone element in the normal direction during the rotor motion is, the more distorted and non-uniform motion characteristics are obtained, when the resonant excitation frequency is applied to the PC. These two responses are given in Appendix D.

In addition to the performed investigation, the responses of the same type were analysed, with the excitation frequency of the PC increased with respect to the resonance ($\nu = 1.25$ and $\nu = 1.43$). Comparing the respective responses (see Appendix D), it was found that the higher shift of the excitation frequency from the resonant frequency causes more irregularities and non-linear motion properties. Hence, the recommended operational regime of high resolution piezoelectric rotary stage to be developed should be equal to or span in the vicinity of resonant excitation frequency (i.e. maximum up to $\nu = 1.25$). In addition, there should be a small (but sufficient) gap between the rotor and the contact zone element in the normal direction during the rotor motion.

2.5. Transient analysis of interaction between the piezocylinder and the rotor

In the last part of this chapter, the emphasis is placed on the transient analysis of interaction between the piezocylinder and the rotor, which allows one to determine the response of the latter element in time under varying external load.

A computational model of the contacting parts was composed (Fig. 2.14) with the boundary conditions being as follows: 1) gravitational force of the rotor (0.5 N) is present; 2) bearing-type fixture is applied to the shaft of the rotor; 3) friction coefficient between the contact zone elements and the rotor is equal to -0.5; 4) in the presence of external loading (0–2 kg), the central axis of the applied load coincides with the rotation axis of the rotor; 5) harmonic excitation signal (60 V, 126.23 kHz) is used to generate motion of the contact zone elements (i.e. it is assumed that the induced displacement and the resulting vibrational motion of the contact zone elements coincide with the behaviour of the excited piezocylinder at the contact zones, when the piezocylinder does not interact with any other structural elements, as it was presented in Subchapter 2.3).

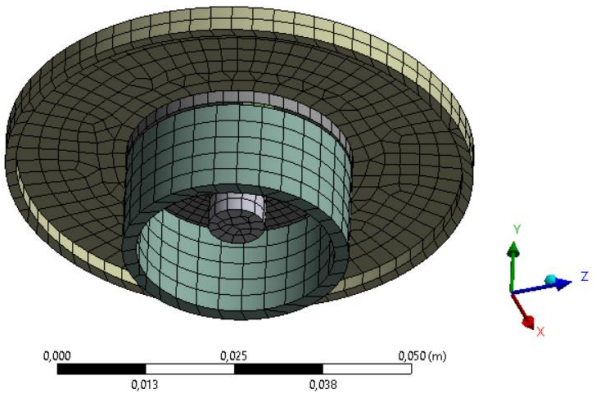

Fig. 2.14. FE model of the interaction between the piezocylinder and the rotor via three equally displaced contact zone elements

Vibro-impact interaction of the contacting surfaces in the analysed piezocylinder-rotor system was implemented by applying the penalty method (pure penalty formulation) which utilises the imaginary stiff springs placed in between the contacting elements (Fig. 2.15). In the given figure, the contact normal (F_n) and tangential (F_t) forces are exerted by the piezocylinder on the contact zone element which is pressed against the rotor. Both elements are treated as rigid bodies in this case. The pure penalty formulation is expressed by the first variation of potential energy of two interacting surfaces

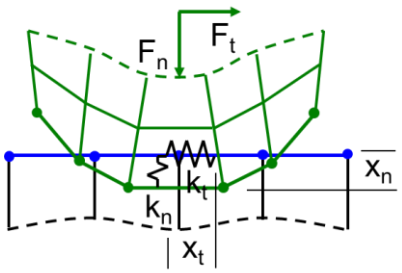

Fig. 2.15. The principle of penalty method applied for the analysis of two contacting surfaces

using the equation given below [123]:

$$\delta \prod = F_n \delta x_n + F_t \delta x_t = k_n x_n \delta x_t + \mathrm{sgn}(x_t) \mu k_n x_n \delta x_t; \quad (30)$$

here k_n is the contact stiffness in the normal direction, x_n is the penetration along the normal direction, x_t is the penetration along the tangential direction, and μ is the coefficient of friction between one contacting element with respect to another.

This investigation was separated into two parts – the first one was devoted to the analysis of transient response of the overall system with respect to tangential displacement, and the second one was devoted to the analysis of an arbitrary selected point in the outer radial surface of the rotor with respect to the tangential and axial displacements.

Firstly, the rotor was not subjected to any external load. The further views (Fig. 2.16) of total displacement indicate the response of a piezocylinder-rotor system at different moments of time after the start of applied electrical excitation. It can be observed that only the locations of the rotor undergoing the induced vibrations are affected (maximal displacement reaches 1.2 μm), when the time is 0.09 ms. Afterwards (at 0.25 ms), the displacement of the rotor is spread more widely, affecting the central part of the rotor (maximal displacement reaches 2.9 μm). At the last instant of time (2 ms), the major outer part of the rotor is displaced (4.6 μm). So, different zones of the rotor become affected over time after the start of electrical excitation. Fig. 2.17a provides the respective transient response of the analysed piezocylinder-rotor system, just in terms of the maximal tangential displacement at the centres of the contact zone elements. Parasitic vibrations of the rotor take place for 2 ms, with no actual rotational motion occurring. Fig. 2.17b illustrates one of the most characteristic responses of the same system, when the applied external load is 2 kg. In this case, the parasitic vibrations vanish after 0.4 ms (settling time), and the actual rotor motion starts; the displacement non-linearly rises until 2 ms and reaches the peak of 28.85 μm. The corresponding responses of the piezocylinder-rotor system under effect of other external loads (0.1–1 kg) are shown in Appendix E. In general, the time required for the actual rotor motion to start differs depending on the applied load; the higher the load is, the less time it takes for the rotor to start moving and the faster parasitic oscillations diminish (see Fig. 2.18).

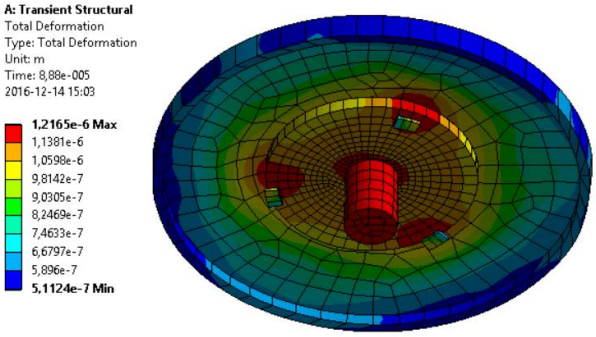

a)

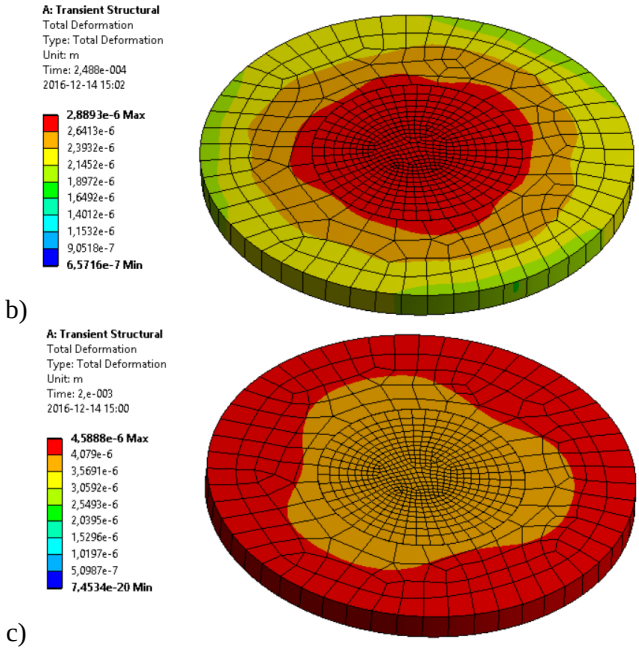

Fig. 2.16. Total displacement of the piezocylinder-rotor system (no external load applied) at different moments of time after the start of electrical excitation: a) at 0.09 ms; b) at 0.25 ms; c) at 2 ms

This non-linear tendency can be explained by the presence of inertia of the rotor, which is directly related to the applied load; hence, the investigated piezocylinder-rotor system is particularly sensitive to load ranging from 0 kg to 0.5 kg, as the settling time decreases significantly.

When analysing the transient response of an arbitrary selected point which is located in the outer radial surface of the rotor (i.e. all points behave in the same way) with respect to the tangential displacement under varying external load (0–2 kg) the characteristic responses were collected, summarised and are illustrated in Fig. 2.19.

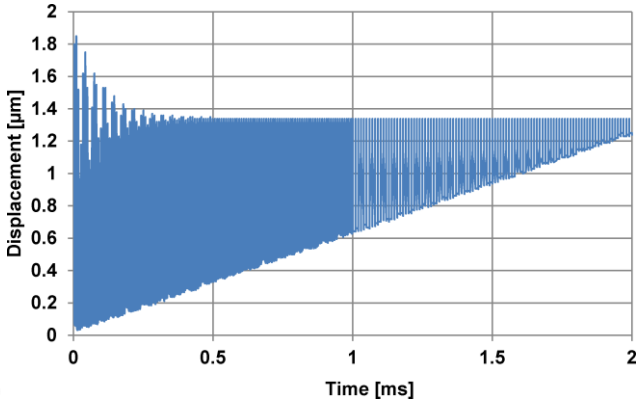

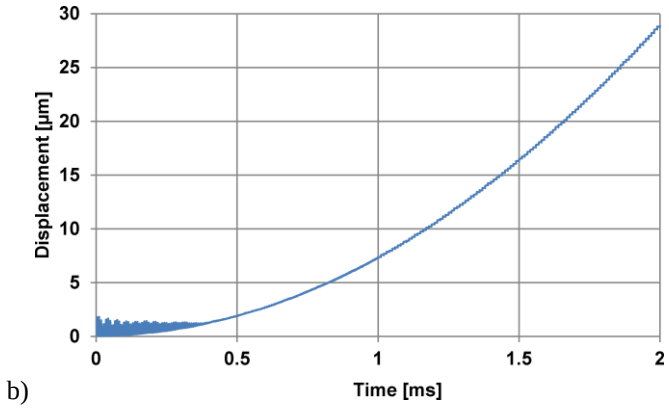

b)

Fig. 2.17. Transient response of the piezocylinder-rotor system in terms of tangential displacement at the centres of the contact zone elements after the start of electrical excitation when the applied external load is: a) 0 kg; b) 2 kg

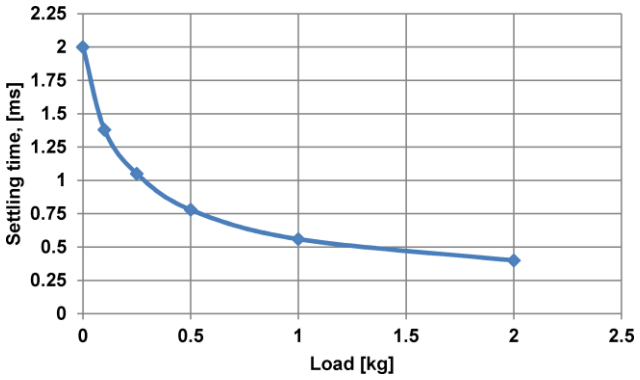

Fig. 2.18. The dependence of settling time (actual motion start) of the rotor on the applied external load

The application of low load (0–0.25 kg) causes a nearly linear increase in the displacement of the selected point. Nonetheless, the presence of higher loads results in a non-linear rise of displacement and a rather significant increase rate. The peaks are observed at the final moment of time (2 ms), with the lowest value of 1.24 µm (0 kg) and the highest value of 28.85 µm (2 kg). It should be noted that all obtained curves are uniform in shape and width, with no parasitic vibrations determined. They represent a well-defined motion of the rotor in the inspected direction.

In terms of axial displacement of the same point under identical loading conditions, the constructed most characteristic respective plots are provided in Fig. 2.20, and the remaining plots are given in Appendix E. It can be stated that the generated displacements are more irregular than the tangential ones which can be explained by the possible influence of design imperfection of the analysed piezocylinder-rotor system or the presence of inertia of the rotor. However, the overall tendency for the response curves to attain a more regular periodic shape is observed, when the used loads are higher. That is mainly due to the resulting higher pressure force causing a more frequent interaction between the rotor and the contact

zone elements. The dependence of the latter frequency on the applied external load is depicted in Fig. 2.21. It is evident that a rise in the applied load from 0 kg to 0.5 kg produces a substantial rise (1.92 kHz/kg) in the contact frequency values. 0.5 kg denotes the limiting (‘saturation’) value after which an increase in the load leads to a minor increase (0.17 kHz/kg) in the contact frequency.

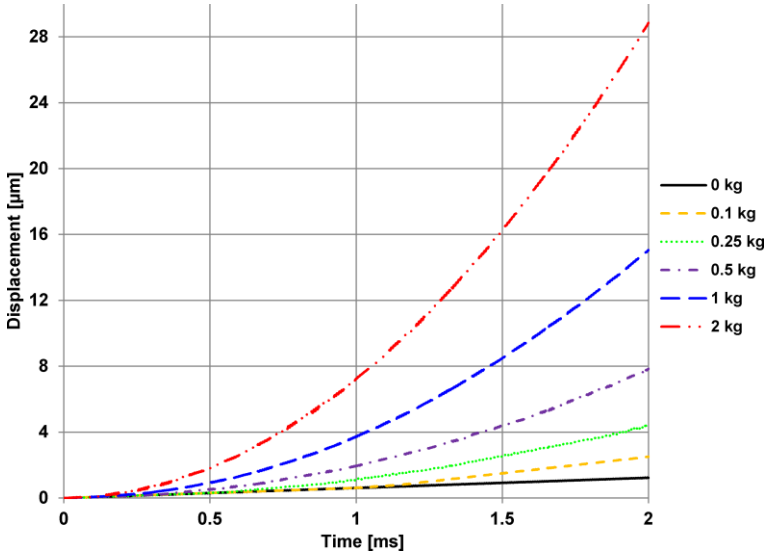

Fig. 2.19. The transient response of the arbitrary selected point of the rotor with respect to tangential displacement after the start of electrical excitation when applying external load

Referring to Fig. 2.19–2.20 and Appendix E, it should also be noted that the peak values of the tangential displacement of the arbitrary selected point of the rotor, which are related to the load-free condition and 0.1 kg, are lower than the corresponding axial displacement values; nonetheless, the tendency inverts significantly for higher loads (see Table 2.2). The application of the load beyond the indicated limit ensures a generation of higher pressure force; hence, the axial displacements decrease to a minimum, while the tangential displacements prevail and increase up to 28.85 μm.

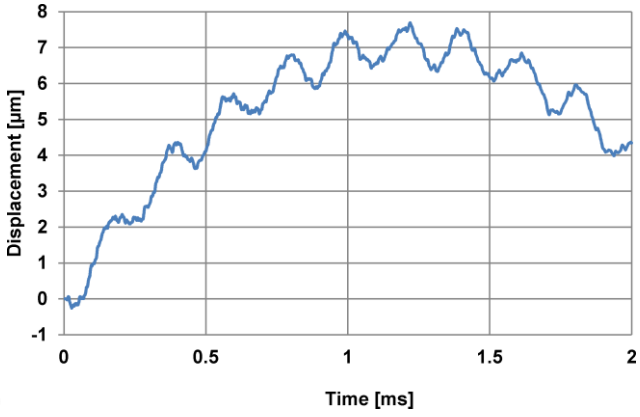

a)

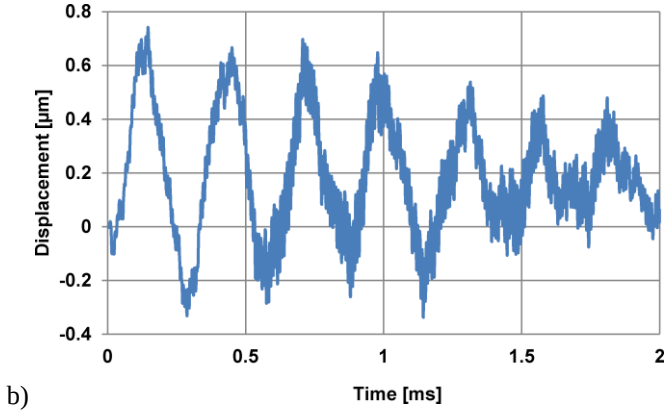

b)

Fig. 2.20. The transient response of the arbitrary selected point of the rotor with respect to axial displacement after the start of electrical excitation when applying an external load of: a) 0 kg; b) 2 kg

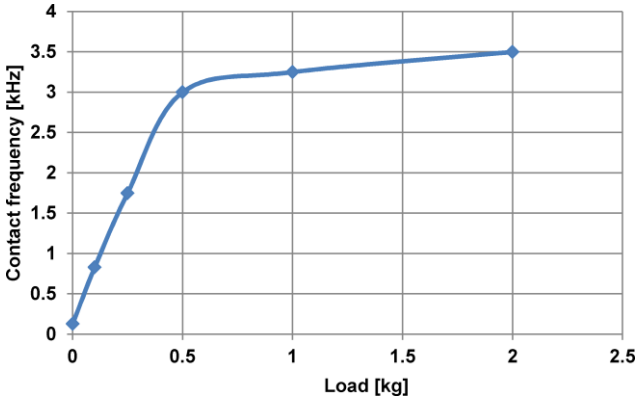

Fig. 2.21. The dependence of contact frequency in the axial direction between the rotor and contact zone elements on the applied external load

Considering all the aspects discussed in this subchapter, it is possible to assume that if no other conditions are changed, a load varying between 0.1 kg and 0.5 kg should provide the lowest minimal incremental step (highest resolution) of the investigated piezocylinder-rotor system.

Table 2.2. A comparison between the maximal tangential and axial displacements of an arbitrary point of the rotor under the effect of external load

	Applied external load					
	0 kg	**0.1 kg**	**0.25 kg**	**0.5 kg**	**1 kg**	**2 kg**
Tangential displacement [µm]	1.24	2.51	4.44	7.84	15.05	28.85
Axial displacement [µm]	7.70	4.12	2.31	1.61	1.21	0.74

2.6. Chapter conclusions

This chapter has presented the theoretical investigation of high-resolution piezoelectric rotary stage driven by resonant ultrasonic standing-waves. Relying on and summarising the obtained results, the following conclusions are made:

- Harmonic and modal analyses of the piezocylinder disclosed the operational frequency interval to fall in the range of 125.8–132 kHz, with the selected operational resonant frequency equal to 126.23 kHz. The research indicated that an increase in the applied driving voltage (20–80 V) leads to a linear rise in the tangential, radial and axial displacements of the contact zones. It was also identified that elliptical motion trajectories of the contact zones in the axial-tangential plane form a well-defined rotational motion of the rotor.
- Lumped-parameter analytical model defined by five DOF, which describes vibro-impact interaction dynamics between the piezocylinder and the rotor, was developed. The recommended operational frequency of the piezocylinder is equal to or span in the vicinity of resonant frequency, and there should be a small gap between the rotor and the contact zone element in the normal direction during the rotor motion. The model can be easily adapted to various piezoelectric friction-based rotary and linear motors.
- Transient numerical studies of the piezocylinder interaction with the rotor under varying external loading (0–2 kg) conditions revealed that the time needed for the actual rotor motion to start is inversely and non-linearly dependent on the applied external load. It was also determined that the tangential displacement of the arbitrary selected point of the rotor is much more uniform when compared to the displacement observed in the axial direction.

3. EXPERIMENTAL RESEARCH OF A HIGH-RESOLUTION PIEZOELECTRIC ROTARY STAGE

This chapter explores the high-resolution piezoelectric stage. Firstly, most of attention is paid to the main dynamic characteristics of the piezocylinder, followed by the motion trajectories of its contact zone elements, and the assessment of surface displacement demonstrated afterwards; properties related to the resolution and torque are determined further, with a possibility to generate torsional oscillations concomitant with rotational motion presented at the end.

In order to examine the operation and performance of the piezostage, an experimental prototype was produced and tested (Fig. 3.1).

Fig. 3.2 presents the design and structure of the system, both of which correspond to the ones thoroughly described in previous subchapters (2.1–2.2).

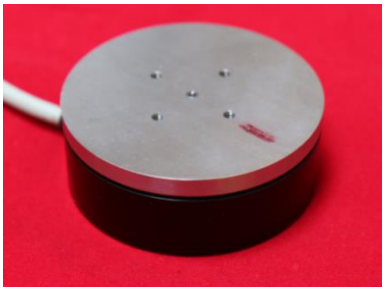

Fig. 3.1. An image of the experimental prototype of the piezoelectric stage

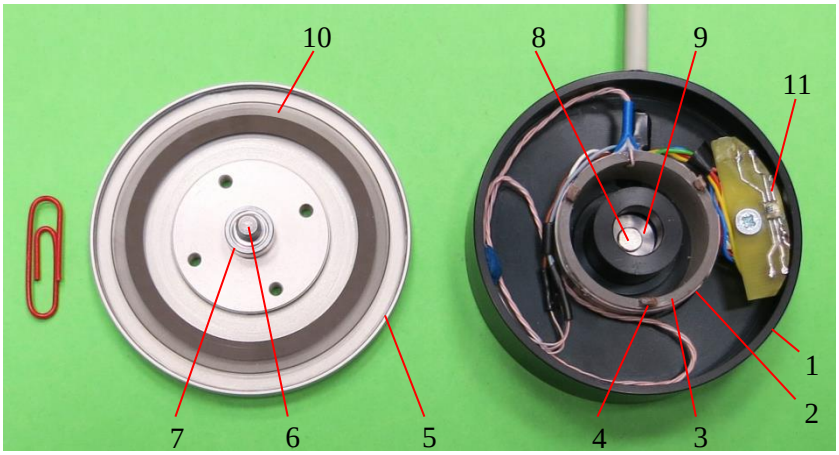

Fig. 3.2. Experimental model of high-resolution piezoelectric rotary stage with indicated components: 1 – housing; 2 – supporting base elements (three units; not visible from top view); 3 – piezocylinder; 4 – contact zone elements (three units); 5 – rotor; 6 – rotor shaft; 7 – precise bearing; 8 – magnet; 9 – non-magnetic material; 10 – glass-chromium incremental scale; 11 – optical head and displacement readout unit

3.1. Main dynamic characteristics

Impedance measurement

To verify the results of theoretical investigation related to the potential limits of the operational regime of the piezoelectric stage, it was initially subjected to impedance analysis. To carry out the aforementioned measurement, an impedance

analyser (Wayne Kerr 6500B) was used (see Fig. 3.3). In this particular case, the characteristics of the PC were explored. The obtained results are depicted in Fig. 3.4. In the beginning, a group of electrodes of the PC, which initiate a clockwise motion of the rotor, was excited. As it is observed in the spectrum (Fig. 3.4a), there are three resonant frequency intervals, where impedance and phase angle curves change mostly, with the most of distinction registered in 124–136 kHz range. Afterwards, the experiment was repeated when inspecting the response of the system in terms of the opposite motion. The formed spectrum (Fig. 3.4b) appears to be very similar to the one defining the clockwise motion in terms of number, shape and values of characteristic frequency intervals. However, the most significant change in the characteristic curves is observed in the range of 125–134 kHz. The differences between both of the mentioned intervals and the maximal and minimal values of impedance can be explained by the effect of tribological properties of contact pairs (i.e. interaction of contact zone elements and rotor) and transient processes occurring in the piezostage when the motion is reversed (i.e. mostly due to presence of inertia);

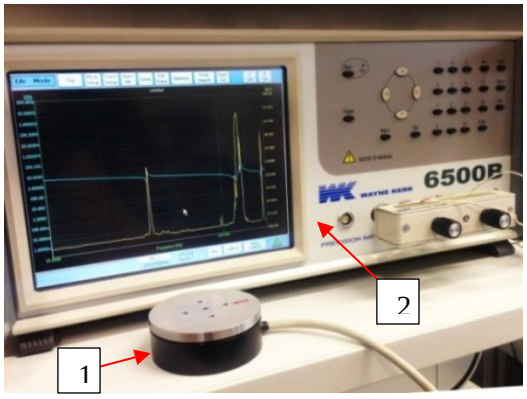

Fig. 3.3. Impedance measurement setup: 1 – investigated high-resolution piezoelectric stage; 2 – impedance analyser (Wayne Kerr 6500B)

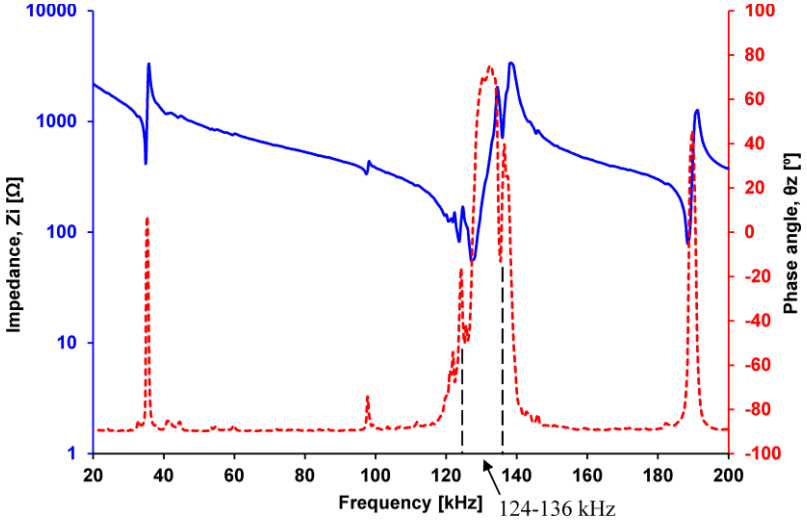

a)

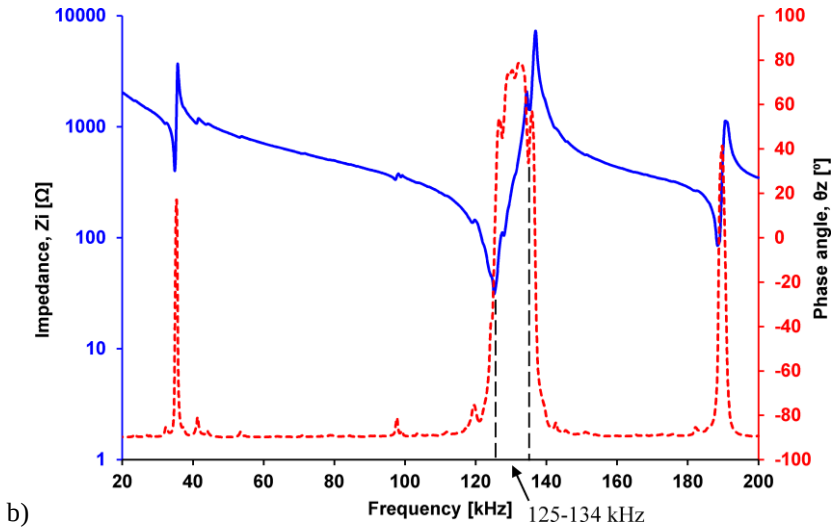

b)

Fig. 3.4. Impedance and phase angle as a function of PC excitation frequency generating motion of the piezostage in clockwise (a) and counter-clockwise (b) direction

the possible inhomogeneity of the piezoceramics impacts that as well. Nevertheless, considering such a close similarity between both spectra, it is possible to state that the determined range values of 125–134 kHz are treated as potential operational regime limits for the designed actuator. It should be reminded that FE analysis revealed the resonant frequency of the piezocylinder, which is the most suitable to induce the required vibration mode, to be 126.23 kHz.

Determination of the resonant frequency and vibration mode

So as to clarify, if the impedance-revealed values are correct and to extend the understanding of the main dynamic properties related to the investigated piezostage, it was necessary to validate the results of theoretical harmonic and modal studies (see Chapter 2). This was achieved by applying the 3D scanning LDV technique. A simplified structural scheme of the laser Doppler vibrometer is given in Fig. 3.5. It contains three computer-controlled optical sensors (X, Y, Z scanning mirrors) and a video camera inside an optical head. The surface of the vibrating object to be analysed is scanned point-by-point by three lasers to provide a large number of very high spatial resolution measurements which allow for accurate dynamic movement detection of the object in different directions in space. As a consequence, the obtained structural vibration data can be used to compute and animate body vibration modes and deflection shapes in frequency and/or time domain upon request. The typical operational steps of 3D scanning vibrometry encompass the definition of measurement points, the investigated structure excitation, a scan to acquire vibration response at each point, visualisation, and data export for post-processing analysis [125–127].

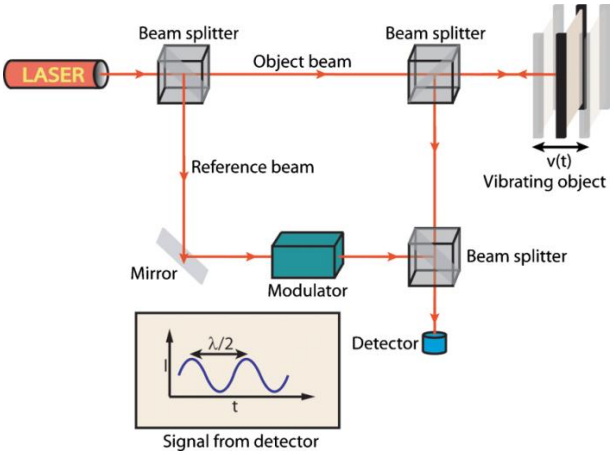

Fig. 3.5. A simplified structural scheme of laser Doppler vibrometer [124]

The experimental equipment employed in this research is presented in Fig. 3.6. At the heart of the setup there is a full-field 3D scanning LDV system Polytec PSV-500-3D-HV with PSV 9.2 software. In order to make an adequate comparison with the FE simulation results, the PC was separated from the housing of the piezoelectric stage, with the bottom surface of the PC immovably fixed (by means of double-sided sticky tape) to a stand. The PC was analysed from clockwise and counter-clockwise rotational motion point of view. The resonant frequencies inducing vibration modes which are most suitable for generating the well-defined rotational motion, were determined. In both experimental cases, the excitation signal frequency varied within 50–150 kHz interval. Amplitude-frequency characteristic in the clockwise direction (see bottom of Fig. 3.7a) indicate that there are seven possible operational resonant frequency values (56.1 kHz, 96 kHz, 123 kHz, 125.8 kHz, 126.26 kHz, 132.9 kHz, 135 kHz) in the spectrum. Referring to the impedance measurement results discussed before (see Fig 3.4), the operational resonant frequency range lies between 125 kHz and 134 kHz. Therefore, just three of the obtained values were examined in detail. The operational frequency was determined on the basis of the same three criteria which were adopted when evaluating the FE simulation results in Section 2.3.2. Considering all the aforementioned aspects, 126.26 kHz was approved as the most suitable frequency to generate clockwise rotational motion of the piezoelectric stage. The resulting displacement of the top surface of the PC at the initial time instant with respect to the non-displaced surface (represented by black mesh) at the selected vibration mode is shown in the upper part of Fig. 3.7a. There are three zones (*A*–*C*), where the displacements attain the maximal values; these zones correspond to the actual locations of contact zone elements. The experiment was repeated for the counter-clockwise case (Fig. 3.7b), with the operational resonant frequency found to be the same as in the previous case. The displacement of the top surface of the PC is slightly more regular when compared to the previous result, but the pattern of the maximal displacement zones (*A'*–*C'*) remains the same. From harmonic analysis point of view, the spectrum almost coincides with the one related to the clockwise direction; the curves

corresponding to tangential, radial and axial displacements are very similar in terms of the shape of curves and the maximal amplitude values. Generally, the vibration mode selected in both investigated cases indicates a close similarity to the one chosen in FE analysis (see Fig. 2.9).

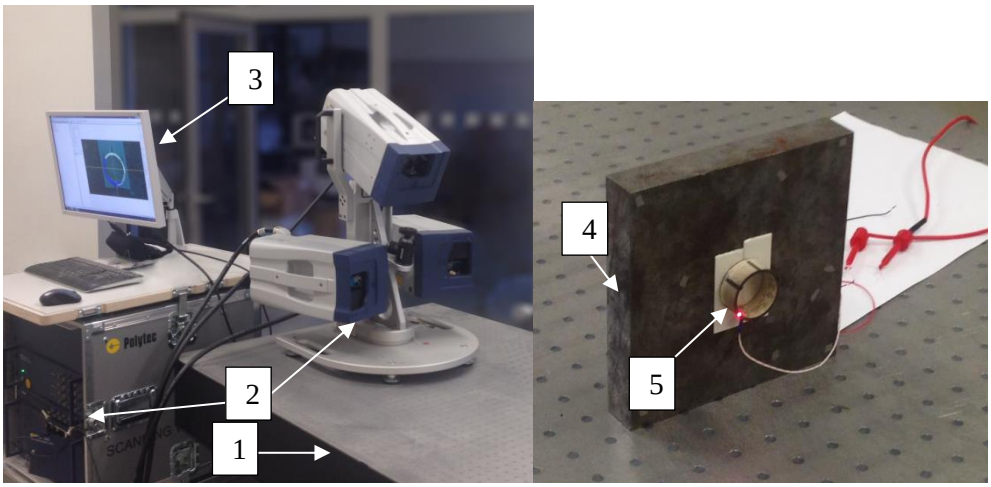

Fig. 3.6. Experimental equipment to determine the operational resonant frequency and vibration mode of the piezocylinder: 1 – optical table (1HT15-20-20, Standa Ltd); 2 – 3D scanning LDV system (Polytec PSV-500-3D); 3 – computer with PSV software; 4 – stand; 5 – piezocylinder

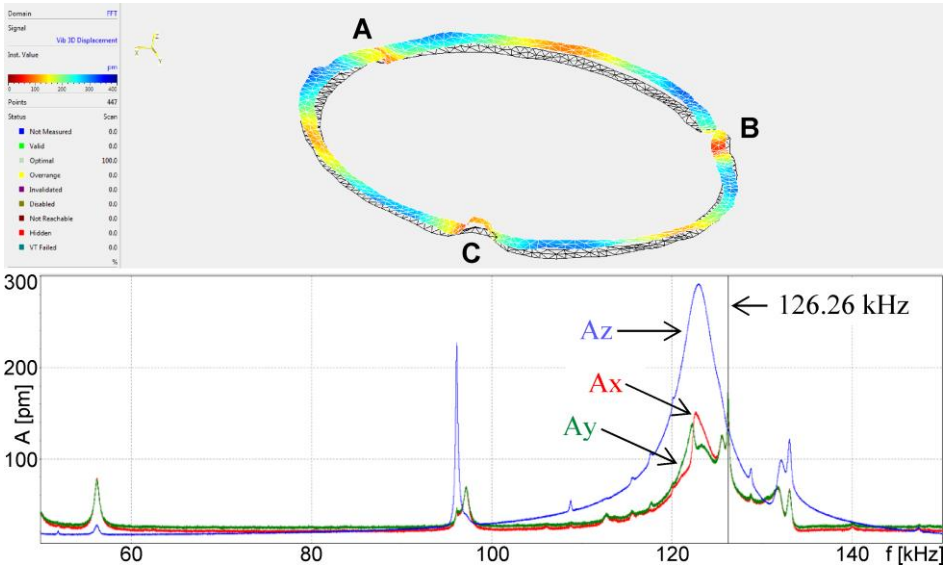

a)

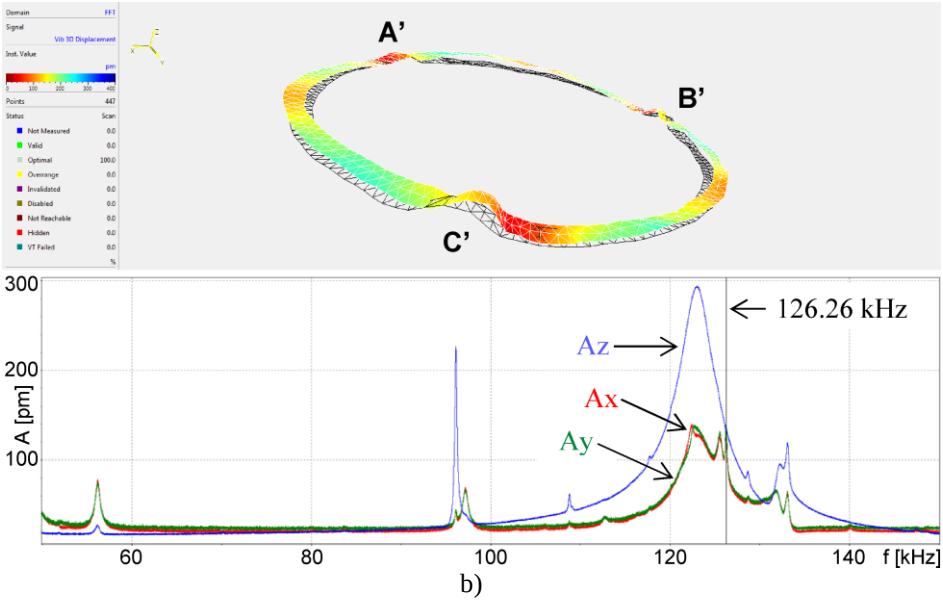

Fig. 3.7. Displacement of the top surface of piezocylinder at selected vibration mode and the corresponding amplitude-frequency characteristics in clockwise (a) and counter-clockwise (b) directions (Ax, Ay, Az are the tangential, radial and axial displacement amplitudes)

Continuing the experiment, the displacement of the top surface of the analysed PC in different spatial directions was inspected. The results given in Fig. 3.8 were obtained under excitation of electrodes at 126.26 kHz to induce rotational motion of the piezoelectric stage. Fig. 3.8a,c,e denote the displacements of the PC in the tangential, radial and axial directions, respectively, in case of clockwise motion. The resulting displacements attributed to the opposite direction of motion are observed in Fig. 3.8b,d,f, accordingly. In Fig. 3.8a, there are two maximal (red), two minimal (blue), and four intermediate (green and yellow) displacement zones; their exact locations are not highly important, because this is only a one-directional (tangential) displacement component. Referring to Fig. 3.8c, it is obvious that the maximal displacement zones are 'shifted' by 90° with respect to the axis of rotation which can be explained by perpendicularity between axes X and Y. Also, there are no minimal displacement zones, which implies that the radial vibrations are exhibited by nearly the entire structure. The most characteristic maximal displacement pattern is visible in Fig. 3.8e. Three equally displaced zones are located exactly at the top of the excited electrodes. It should be reminded that the axial and tangential oscillations have a pronounced influence on the generation of a well-defined motion of the piezostage. Analysing the views attributed to the counter-clockwise motion (Fig. 3.8b,d,f), the number of the maximal, minimal and intermediate displacement zones is nearly the same for each respective vibrational direction compared to the previously discussed figures. The only difference is the opposite locations, i.e. the characteristic zones are 'shifted' by 90° for the tangential and radial displacements with respect to the axis of rotation and 60° correspondingly for the axial displacement. This is governed by the excitation of a group of three other electrodes.

To sum up, it can be stated that the selected resonant frequencies induce such oscillations in the piezocylinder which cause the formation of regular displacement of the top surface in all spatial directions. Based on that, the operational frequencies are confirmed to be chosen correctly.

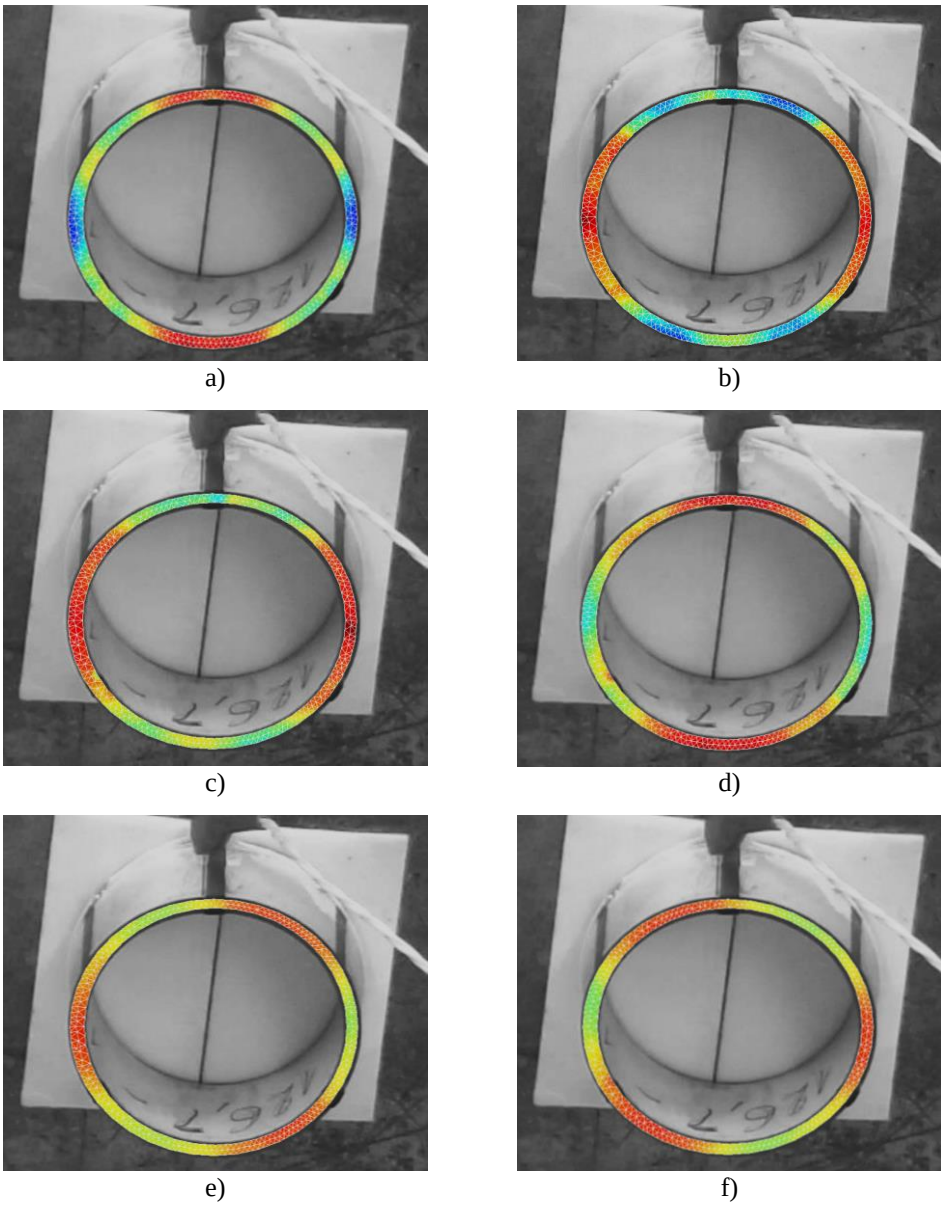

Fig. 3.8. Displacements of the top surface of PC in the tangential (a, b), radial (c, d) and axial (e, f) directions under the excitation of electrodes (f = 126.26 kHz) to induce clockwise (a, c, e) and counter-clockwise (b, d, f) rotational motion of piezoelectric stage [red zones indicate maximal displacements, while blue zones correspond to minimal displacements]

3.2. Motion trajectories of contact zone elements

As it was already discussed in Chapter 2, elliptical motion trajectory plays a crucial role in standing- and travelling-wave ultrasonic resonant-type motors, since it determines how uniform the generated motion is. Therefore, in order to conduct a more in-depth research of the designed system dynamics and validate the FE modelling results, it was essential to form the vibrational motion trajectories of contact zone elements in all spatial planes. Moreover, the relationship between the applied voltage amplitude and induced motion trajectory was identified in each case. The experimental setup (including the piezocylinder) used in this investigation was the same as presented in the previous subchapter (see Fig. 3.6). Initially, 126.26 kHz harmonic electrical excitation signal was supplied to the PC to generate a clockwise motion of the contact zone elements. Fig. 3.9a shows a plot containing a series of motion trajectory curves in XY plane. All curves are characterised by a regular and even elliptical shape, which reveals a similarity between the tangential and radial oscillations. However, the amplitudes of displacements disclose the tangential vibrations to be predominant. In the latter direction, the minimal displacement amplitude value is 0.12 μm (20 V), while the maximal value is 0.45 μm (80 V). In the radial direction, the corresponding values are equal to 0.11 μm (20 V) and 0.41 μm (80 V). Motion trajectories in the YZ plane are given in Fig. 3.9b. Here, the shapes of the curves are also elliptical but narrower when compared to the curves in the XY plane, because the axial oscillations are not as strong as the tangential and radial ones. The lowest and highest amplitudes of the vibrations in the axial direction reach 0.07 μm (20 V) and 0.29 μm (80 V). All maximal displacement amplitude values are summarised and presented in Table 3.1. Vibrational motion trajectories attributed to the XZ plane are plotted in Fig. 3.9c. The constructed shapes are very similar to the shapes of the YZ-related trajectories, just the amplitudes are higher. The contact zone elements move uniformly in the XZ plane, thus indicating the suitability of the chosen resonant frequency for successful generation of the rotor motion of the piezoelectric stage in a clockwise direction.

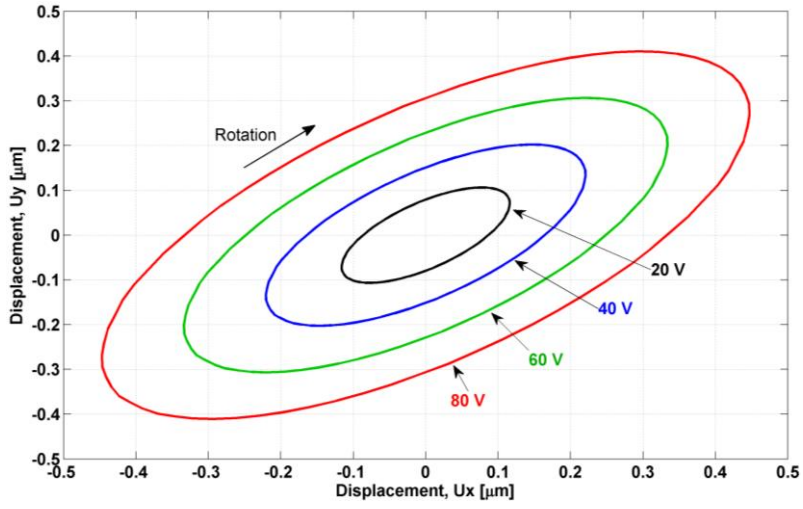

a)

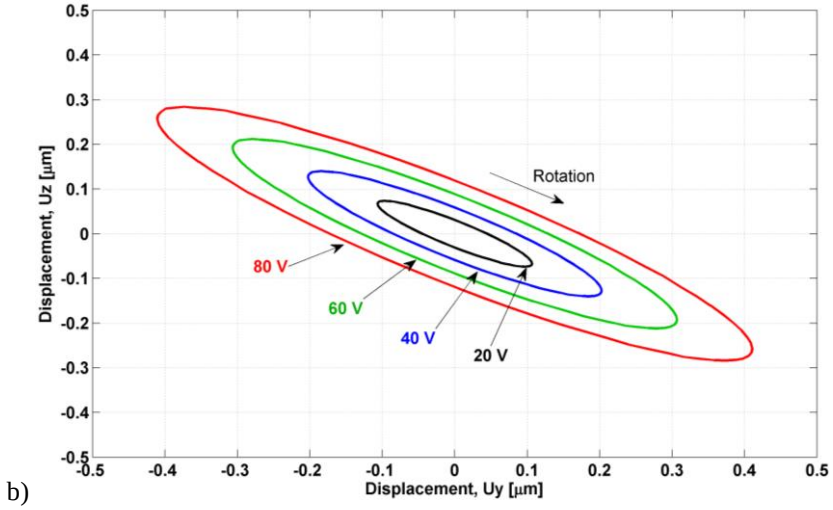

b)

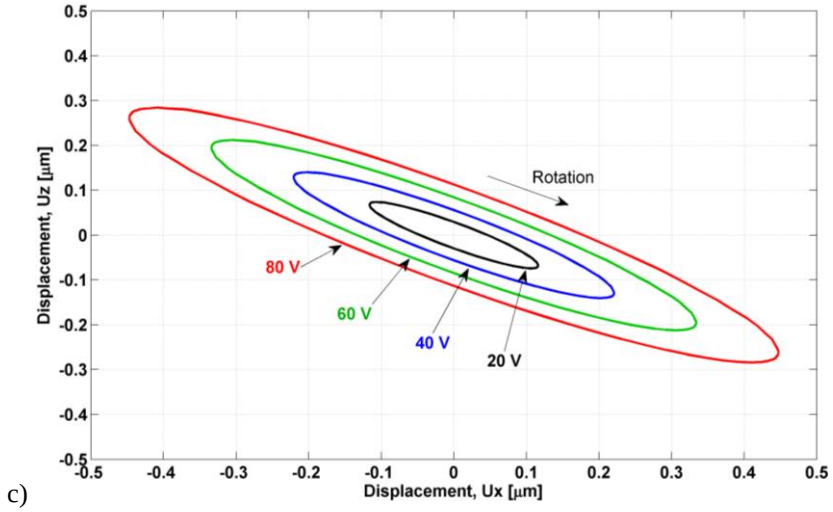

c)

Fig. 3.9. The relationship between applied voltage amplitude and induced clockwise rotational motion trajectories of contact zone elements in planes: XY (a), YZ (b), and XZ (c)

Observing the relationship between the applied voltage amplitude and induced motion trajectory in each case, it can be stated that a supply of higher electrical potential to the PC leads to a higher displacement amplitudes of the contact zone elements. This results in more extended elliptical motion trajectories.

Table 3.1. Maximal displacement amplitude values of contact zone elements for clockwise rotational motion in the presence of applied voltage

	20 V	**40 V**	**60 V**	**80 V**
X direction	0.12 μm	0.22 μm	0.33 μm	0.45 μm
Y direction	0.11 μm	0.20 μm	0.31 μm	0.41 μm
Z direction	0.07 μm	0.14 μm	0.21 μm	0.29 μm

In the next step, the same experimental study was conducted with respect to the opposite rotational direction. As well as in the clockwise case, the PC was subjected to 126.26 kHz harmonic electrical excitation signal. At first, the curves, which define the motion in the XY plane, were plotted (Fig. 3.10a). The trajectories attain uniform elliptical shapes, so the amplitudes of the tangential and radial vibrations are very similar. The minimal tangential displacement (at 20V) is approximately 0.09 µm, and the relevant maximal displacement (at 80 V) is 0.35 µm. The respective values for the radial oscillations reach around 0.09 µm and 0.33 µm, accordingly. In the case of the YZ plane (Fig. 3.10b), the elliptical shapes are retained but they are contracted compared to the plot provided in Fig. 3.10a. That is caused by stronger radial vibrations than the axial ones. The lowest and highest amplitudes of these oscillations are equal to 0.08 µm and 0.29 µm, correspondingly.

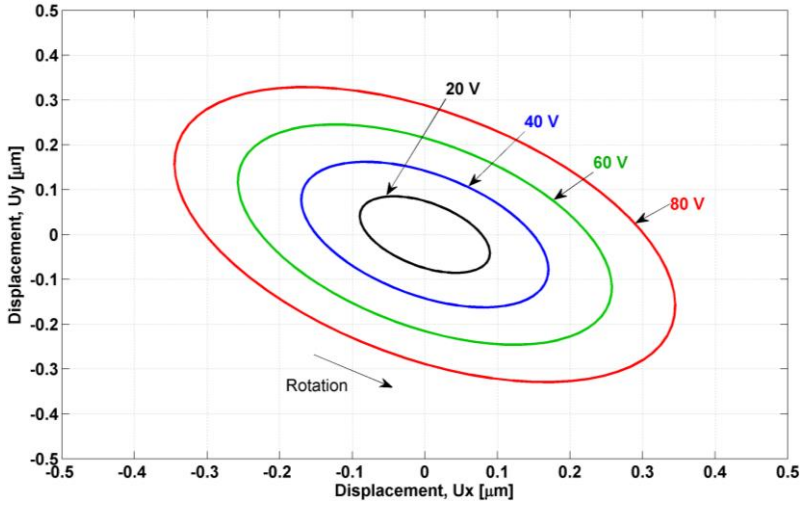

a)

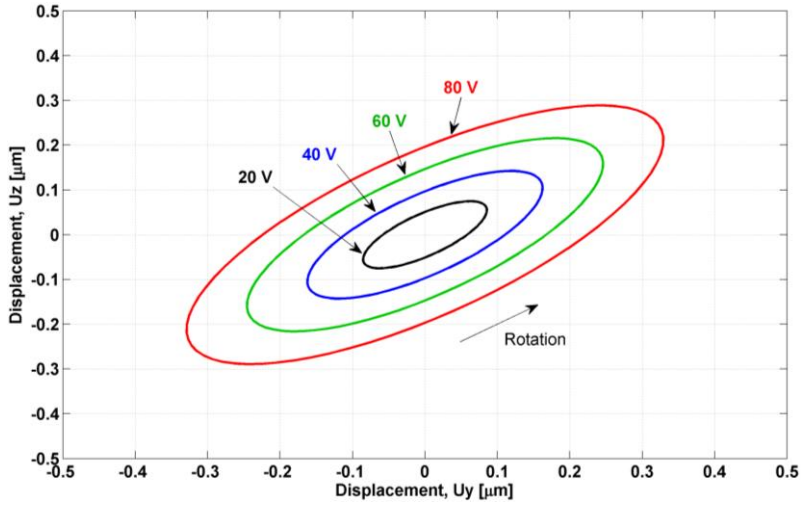

b)

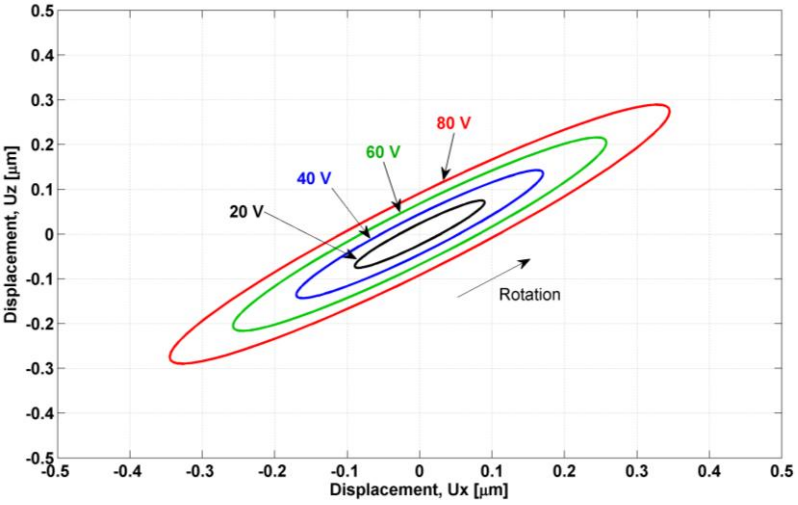

c)

Fig. 3.10. The relationship between applied voltage amplitude and induced counter-clockwise rotational motion trajectories of contact zone elements in planes: XY (a), YZ (b), and XZ (c)

Table 3.2 provides all summarised maximal displacement amplitude values related to the counter-clockwise direction. Fig. 3.10c illustrates the motion of the contact zone elements in the XZ plane. The tendency for elliptical trajectories to become narrower remains, with the tangential vibrations being prevalent. However, the obtained shape leads to well-defined motion, making the selected resonant frequency suitable to move the rotor of the piezoelectric stage in the analysed direction.

The dependence of applied voltage amplitude on the induced motion trajectory with respect to all analysed planes shows the tendency for the displacement amplitudes of the contact zone elements to rise under the effect of voltage increase, causing the formation of more extended elliptical motion trajectories.

Table 3.2. Maximal displacement amplitude values of contact zone elements for counter-clockwise rotational motion in the presence of voltage

	20 V	**40 V**	**60 V**	**80 V**
X direction	0.09 µm	0.17 µm	0.26 µm	0.35 µm
Y direction	0.09 µm	0.16 µm	0.25 µm	0.33 µm
Z direction	0.08 µm	0.14 µm	0.22 µm	0.29 µm

In summary, comparing the results associated with clockwise and counter-clockwise direction, it should be said that vibrational motion trajectories of the contact zone elements attain regular and well-defined elliptical shapes in all spatial planes. The only difference is a change in the values of displacement amplitude, i.e. the clockwise motion-based values associated with the tangential and radial directions are higher than the corresponding values attributed to the counter-clockwise motion on average by 28% and 25%, respectively; the opposite tendency is identified for the axial direction, with an average difference of 1.6%. The highest amplitudes are also registered in the tangential and radial directions (for both

rotational cases). As a consequence, the plotted trajectories become wider compared to situation, when the axial displacements are involved. This tendency is valid for all range of applied voltage. Considering all discussed aspects and experimental results, 126.26 kHz was proven to be the operational resonant frequency for generating bi-directional rotational motion of the designed piezoelectric stage.

3.3. Assessment of surface displacement of piezocylinder

For systems characterised by high-frequency vibrations with amplitudes lying in a nano-/micrometer ranges, one of the most efficient and effective relevant methods is digital holographic interferometry. It is a powerful full-field real-time optical characterisation technique enabling a mapping of changes in the shape of 3D objects with high accuracy [128–129].

To investigate the piezoelectric stage with respect to surface displacement of the piezocylinder, the PRISM (Precise Real-time Instrument for Surface Measurement) holography system was applied [130–131]. PRISM is composed of the control block, an object beam splitter, and a camera. The overall experimental equipment used in the analysis is depicted in Fig. 3.11.

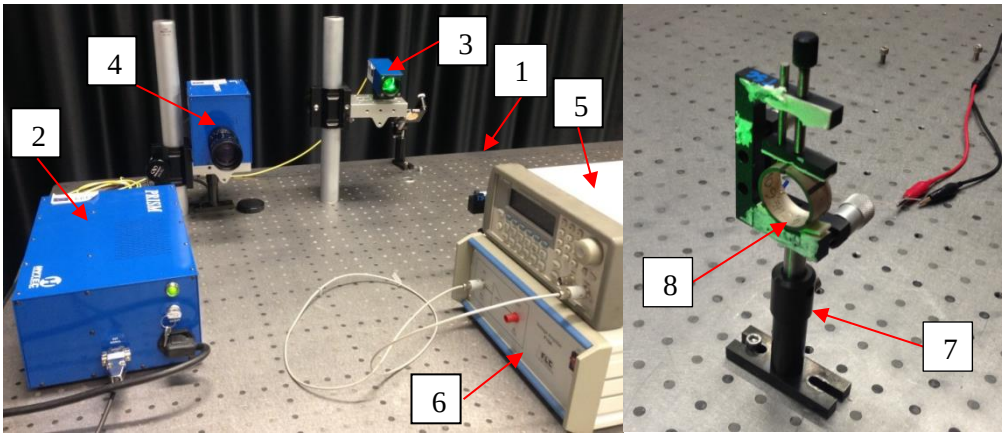

Fig. 3.11. Experimental setup for investigating the surface displacement of piezocylinder by holographic interferometry: 1 – optical table (1HT15-20-20, Standa Ltd); 2 – control block (PRISM); 3 – object beam splitter (PRISM); 4 – camera (PRISM); 5 – signal generator (Agilent 33220A); 6 – amplifier (P-200); 7 – holder; 8 – piezocylinder; computer (not shown in the figure)

The operation of the system is explained with reference to Fig. 3.12. A 20 mW laser (λ = 532 nm) is used as a coherent light source. Initially, the object beam is supplied from the control block to the beam splitter (lenses) and directed towards the main object. At the same time, the second (reference) beam is supplied to the camera (recording medium), where it is spread by lenses as well, thus interfering with the object beam reflected from the analysed vibrating PC. The generation of both beams is governed by the control block which also regulates/changes the ratio between these beams in order to achieve the best possible resolution of interference fringes. The ratio is usually about 1:2.2. A signal generator and an amplifier are applied to

ensure that the piezoelement vibrates at a necessary frequency. After an image is constructed in the camera, it is sent to a computer and processed with the specialised software PRISMA-DAQ allowing the user to observe the processes occurring inside and outside (surface) of the target. The influence of various internal and external causes on the object of investigation is registered in real time; so, if the piezoceramics is subjected to even a small deformation, relative phases of the two light fields alter, which leads to a corresponding change in the interference pattern and, consequently, the amplitude of surface displacement.

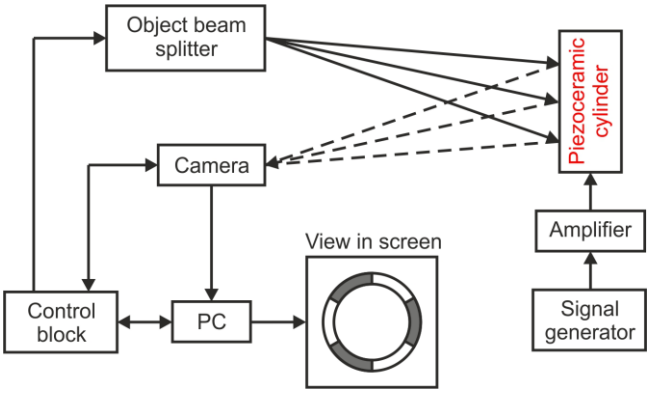

Fig. 3.12. A structural scheme of holographic interferometry-based system for investigating the surface displacement of a piezocylinder

The interference pattern (i.e. fringes) of an investigated oscillating element is registered using time-averaged holography. Using this technique, all views of the vibrating surface are registered over certain period of time. Let us assume that harmonic vibration of a vibrating body is defined by

$$Z(x)\sin\omega t; \tag{31}$$

here $Z(x)$ is the amplitude of vibrations of a the body with respect to coordinate x, ω is the angular frequency of oscillations, t is the time. According to [129, 132], the characteristic function, which defines the complex amplitude of the laser beam in the plane of the hologram, takes the form of

$$M_T = \lim_{T\to\infty}\frac{1}{T}\int_0^T \exp\left(i\left(\frac{4\pi}{\lambda}\right)Z(x)\sin\omega t\right)dt; \tag{32}$$

here M_T is the relevant time function, T is the exposure time of the hologram ($T \gg 2\pi/\omega$), and λ is the wavelength of laser light. After a rearrangement of terms, the following equation is valid:

$$M_T = J_0\left[\left(\frac{4\pi}{\lambda}\right)Z(x)\right]; \tag{33}$$

here J_0 is the Bessel function of the first kind and zero order. Then the resulting light intensity of illuminance I of a single point (coordinates(x, y)) on the hologram is

$$I(x,y) = A^2(x,y)|M_T|^2; \tag{34}$$

here $A(x, y)$ is the distribution of the amplitude of the incident laser light beam. As a result, the midpoints of the formed bright fringes coincide with such points of the surface and such amplitude of vibrations $Z(x)$ where the squared Bessel function J_0^2 attains the maximal values. When the values of the latter function are minimal or equal to zero, the pattern of dark fringes appears.

As it was presented at the beginning of the section, this experiment is devoted to analyse the displacement of surface of the PC from the point of view of quality. The results of this investigation should allow not only to observe the maximal and minimal displacement zones of different surfaces, but also to verify whether the locations of three contact zone elements were chosen correctly.

In order to induce ultrasonic standing-wave vibrations in the piezocylinder, electric wiring was prepared in the same manner as it was when measuring displacement of the top surface of the PC and vibrational displacements of the contact zone elements. The view of the PC with marked electrodes is given in Fig. 3.13. High frequency electrical signal defined by Ucos(ωt) was used to excite one group of electrodes (*1, 3, 5*) at a time to initiate the oscillations required to generate clockwise motion of the rotor. Afterwards, another group of electrodes (*2, 4, 6*) was excited to cause the counter-clockwise rotational motion. In both cases, the common inner side of the piezocylinder was used for electrical grounding. During this investigation, the PC was mounted in a special holder in such a way that only its outer surface would be fixed (as shown in Fig. 3.11 and Fig. 3.14) so as the PC would be able to become deformed in the axial direction. Fig. 3.14 illustrates the holographic view of the top surface of the piezocylinder when it is not subjected to any voltage. In the figure, the added numbers denote the local elements of the experimental sub-setup. Fig. 3.15a indicates the effect of applied voltage (30 V) and operational harmonic excitation frequency of 126.26 kHz on the first group of PC electrodes to induce clockwise motion, as well as on the second group of electrodes to generate the opposite motion (Fig. 3.15b). In each case, the interferential pattern of bright and dark zones is well observed, though separate characteristic fringes are not clearly distinguished and visible because of relatively small vibrational amplitudes and limited sensing capability (i.e. resolution) of the applied equipment.

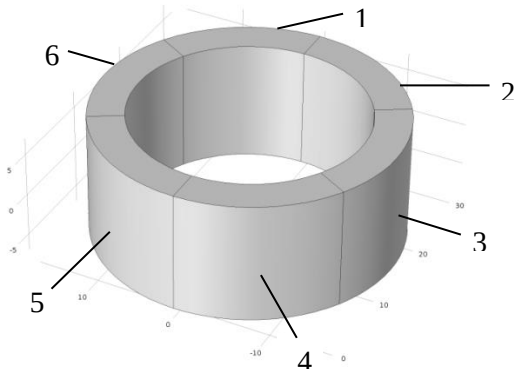

Fig. 3.13. The investigated piezocylinder, with indicated sectioned electrodes equally displaced by every 60°

Three dark zones coincide with a group of electrodes affected by the electrical potential, and three bright areas indicate the unexcited electrodes. Comparing the presented figures, a ‘shift’ of 60° is observed between the interferential zones. Afterwards, the performed experiment was repeated under the effect of electrical potential of 40 V (Fig. 3.16). The interferential pattern becomes more ‘intensive’ in terms of colours, showing an increase in strength of induced oscillations and thus, attained higher displacement.

Since there was a need to have a more explicit understanding of how the PC is deformed, the object was rotated by 90° and mounted in the same holder in parallel to Z axis. Afterwards, the experiment was repeated exciting one electrode at a time. The applied voltage was 30 V for all measurements. The obtained holograms are shown in Fig. 3.17. In general, the dark fringes of standing wave represent constructive interference and are responsible for the rotational motion generation. Bright fringes of the wave indicate destructive interference making certain locations to remain at rest, when a body oscillates. For the analysis of clockwise rotational motion, section *1* was examined (Fig. 3.17a); the observed fringes partially represent the selected operational vibration mode. The four dark fringes at the top and bottom of the electrode indicate even displacement (anti-nodes) zones. The two thickest bright lines correspond to two nodal zones, where no displacement occurs.

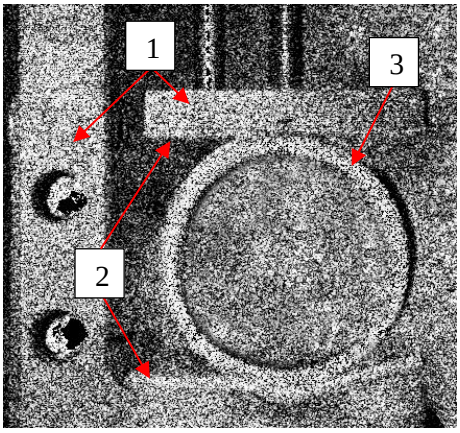

Fig. 3.14. Holographic view of the top surface of the piezocylinder, when harmonic excitation signal is not applied; the structural elements: 1) holder; 2) double-sided sticky tape; 3) analysed piezocylinder

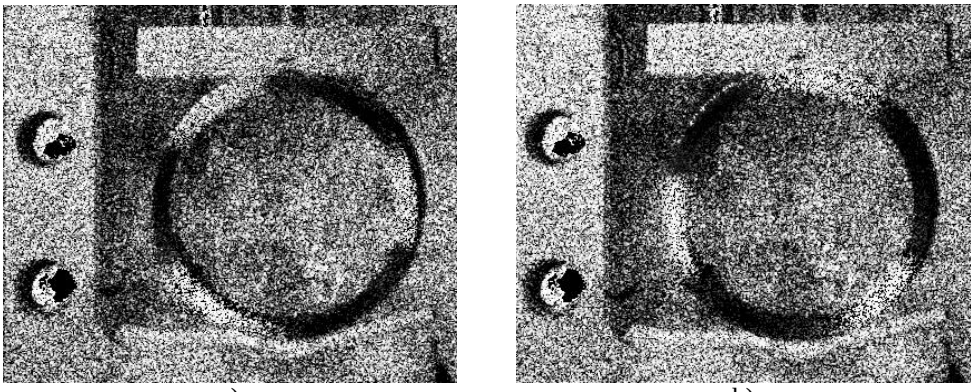

a) b)

Fig. 3.15. Holographic views of the top surface of piezocylinder when exciting (U = 30 V, f = 126.26 kHz) a group of electrodes for motion in clockwise (a) and counter-clockwise (b) direction

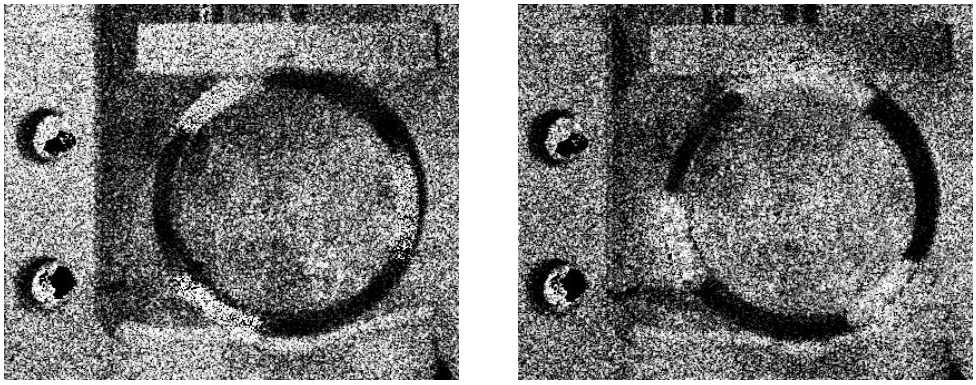

a) b)

Fig. 3.16. Holographic views of the top surface of piezocylinder when exciting (U = 40 V, f = 126.26 kHz) a group of electrodes for motion in clockwise (a) and counter-clockwise (b) direction

Since sections *3* and *5* were excited simultaneously with section *1*, the relevant characteristic fringes were distributed nearly identically compared to the revealed figure and thus, not given here. Fig. 3.17b shows how the adjacent electrode *2* behaves under the effect of voltage supplied to electrode *1*. Interferential fields are formed here as well. The amount, width and uniformity of lines are different in this case, but it can be stated that the generated standing-wave oscillations are passed to the adjacent (i.e. not excited) electrodes as well. The same tendency is valid for sections *4* and *6*. A reversal of rotational motion direction imparts an interchange of patterns on electrodes *1* (also *3* and *5*) and *2* (also *4* and *6*). This is confirmed by the holograms provided in Fig. 3.17c and Fig. 3.17d. Analysing the excited section with regards to characteristic fringes, it is necessary to note that the pattern is very similar to the one described in the first figure. However, all zones are slightly changed, considering their shifted positions and shapes.

The performance of the PC indicates the suitability of both the selected topology of electrodes and excitation type for a uniform displacement of the top and side surfaces. That, in turn, can potentially lead to the generation of the well-defined motion of the rotor of the designed piezoelectric stage in both rotational directions.

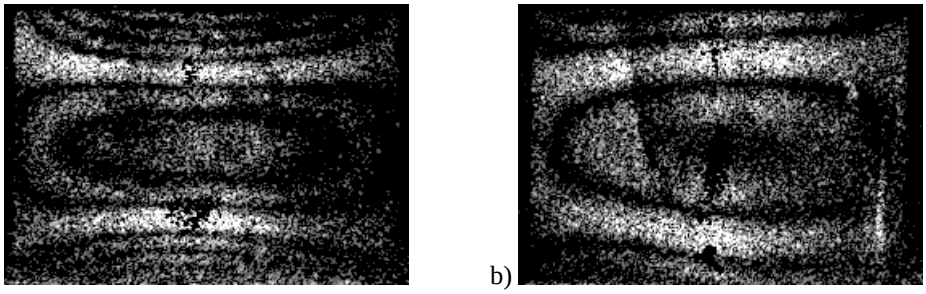

a) b)

c) 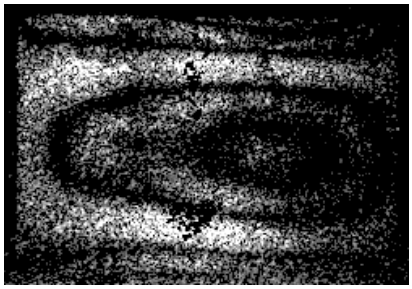 d) 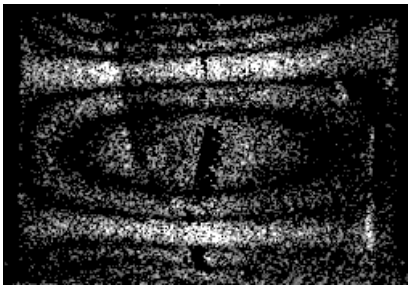

Fig. 3.17. Holographic views of side surfaces of piezocylinder in case of clockwise rotational motion (electrode 1 (a), electrode 2 (b); f = 126.26 kHz, U = 30 V) and counter-clockwise rotational motion (electrode 1 (a), electrode 2 (b); f = 126.26 kHz, U = 30 V)

Nonetheless, due to the slightly shifting nodal zones (caused by motion reversal) in the excited electrodes, the exact constant positions for three contact zone elements and supporting base elements cannot be precisely determined; therefore, the most suitable positions were approved based on the results of FE analysis and 3D LDV already discussed in the thesis.

3.4. Resolution measurement

In a wide range of applications related to modern science and technology, resolution plays a very significant role [133–135]. According to [84, 136], resolution is the smallest increment of input step that can be reliably detected. In case of an actuator, it describes the smallest possible increment of movement (i.e. microstep).

Since precise and accurate positioning of any object pertains to resolution of an applied system, the actuator presented in this thesis was designed to be characterized by as minimal as possible rotational unit step size.

The experimental setup for piezoelectric stage analysis with respect to resolution is revealed in Fig. 3.18, and the simplified structural scheme of the corresponding equipment configuration is demonstrated in Fig. 3.19. The process started with a feed of high frequency harmonic signal, which was obtained from signal generator, to the piezocylinder. The required voltage was gained by using a voltage amplifier. Then the rest of the system was incorporated. At the heart of it, there was a laser Doppler vibrometer (LDV) consisting of a fibre-optic interferometer (connected with a laser sensor head) and a vibrometer controller. Having the latter components set, a very small cylindrical target was placed on the top surface of the rotor in a place which would ensure the best reflectance of the optical signal received from the laser sensor head. The head was directed to the target in such way that it would be manageable to identify the incremental motion of the rotor in the tangential direction. The obtained feedback signal indicating step displacement was passed to the vibrometer controller. Being connected to the controller, the oscilloscope acted as an analogue-to-digital converter and expressed the characteristic signal as voltage. The collected data were transferred, processed, and took the form of graphical representation. Afterwards, the output data were extracted and converted to angular displacement resolution.

The main component of the experimental setup is Polytec LDV system, with the main features of the applied initial analytical regime as stated below:

- Type of signal supplied to the piezocylinder – burst;
- Number of trigger cycles per second – 3;
- Voltage of signal – 40 V;
- Frequency of signal – 126.26 kHz;

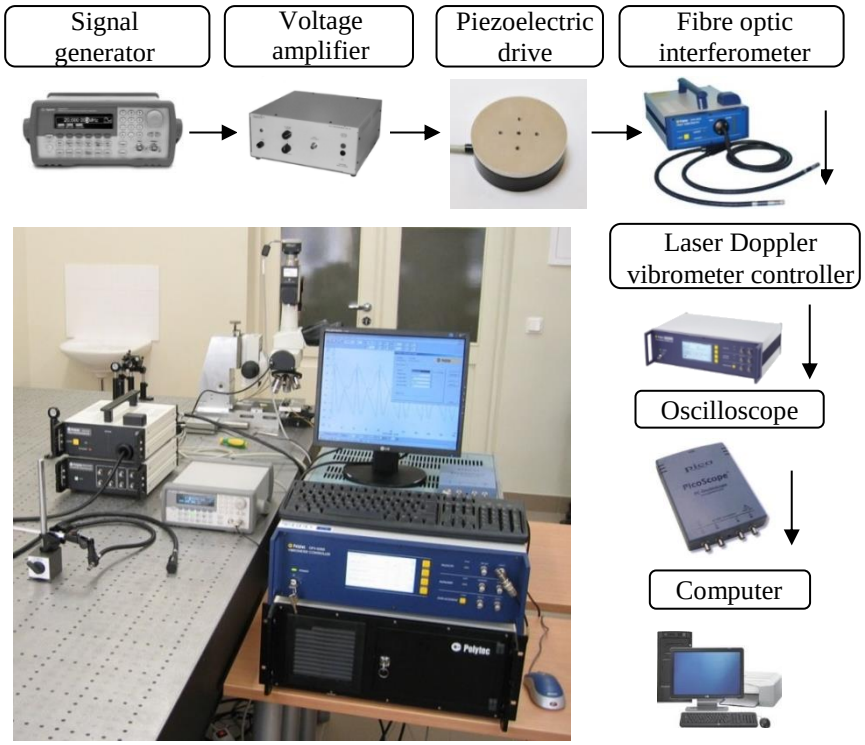

Fig. 3.18. The experimental setup for analysing the resolution of the piezoelectric rotary stage. Components: an optical table (1HT15-20-20, Standa Ltd); a signal generator (Agilent 33220A); a voltage amplifier (EPA-104); the piezoelectric stage; a fibre optic interferometer (Polytec OFV-512); a laser Doppler vibrometer controller (Polytec OFV-5000); an oscilloscope (PicoScope-3424); a computer

When determining the resolution of the piezoelectric stage, two parameters are significant; the first one is the number of trigger cycles per second, and the second one is the supplied voltage. Decreasing either of them to a minimum (or both, in the best case) provides a minimal incremental angular displacement of rotor. Knowing that the PC is capable of generating standing-wave vibrations at 20 V (see Subchapter 3.2), this value was adopted as the lowest constant limit, with the trigger cycles being gradually decreased from 50 to 0. As a consequence, no motion was observed within the given range. The same result was maintained after increase in voltage up to 30 V. A further enhance of voltage up to 40 V translated into the least detectable incremental motion, when the amount of trigger cycles was equal to 3. The constructed resulting curve is shown in Fig. 3.20. It should be noted that the

initially obtained response signal was filtered and interpolated. The stepped rise of the plot (0–16 s) denotes a clockwise motion followed by a transient process (16–19 s) indicating a change in the rotational direction. That explains the appearance of some micro-irregularities at the top of the curve. A counter-clockwise motion featured by a stepped fall occurs from 19 s to 34 s until the rotor stops. The average resolution (i.e. single incremental step) value attributed to the clockwise rotation is 0.250 μrad, with 0.258 μrad related to reverse motion. Thus, the resolution in the clockwise direction differs from that in the opposite direction only by about 3%.

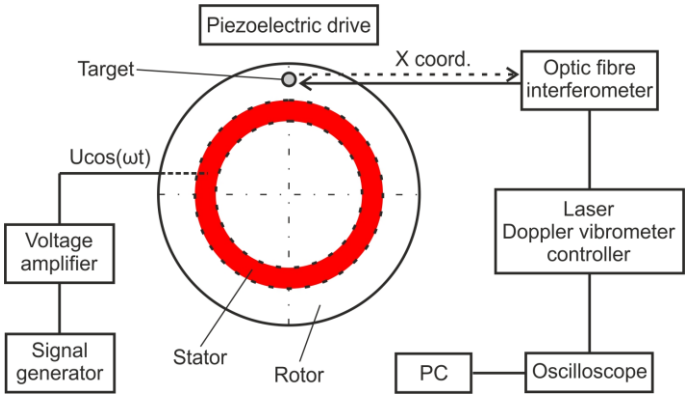

Fig. 3.19. Simplified structural representation (top view) of experimental setup for investigation of resolution of piezoelectric rotary stage

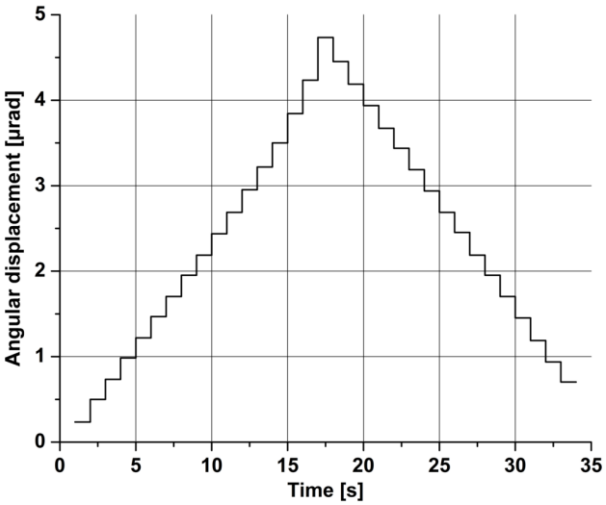

Fig. 3.20. The resolution of piezoelectric stage depending on time and direction of motion: 0.250 μrad in the clockwise direction (0–16 s) and 0.258 μrad in the counter-clockwise direction (19–34 s)

During resolution analysis, the rotor dynamics is of critical importance. The mass of the rotor directly pertains to its inertia and thus, the overall performance, i.e. the higher the mass, the higher the inertia, the more complicated transient processes

are to handle. These processes cover not only the reversal of rotational motion, but also the start-stop moments inevitably repeating many times in precise and accurate positioning. As a sample, the single incremental step of the rotor is provided for a better understanding (Fig. 3.21). The red line represents the signal supplied by the generator, whereas the blue line stands for the displacement of the rotor. At the initial time instant (0 ms), the driving burst-type voltage signal was supplied to the piezocylinder. That immediately imposed the generation of high-frequency torsional oscillations of the rotor, when it was actually still not rotating. This behaviour is represented in the plot within the time interval of 0–1 ms. Afterwards, the amplitudes of torsional vibrations decreased, and the rotor started moving (1–2 ms). At 2 ms the driving voltage signal was terminated, but it should be highlighted that the rotor continued moving because of inertia. The stop of the motion is registered at 7 ms. After this point is reached, the piezocylinder must be supplied with another burst-type voltage signal in order to activate the rotor for the second minimal incremental motion step. The opposite tendency is observed if there is a need to halt the rotor or reverse the motion, while the rotor is still running.

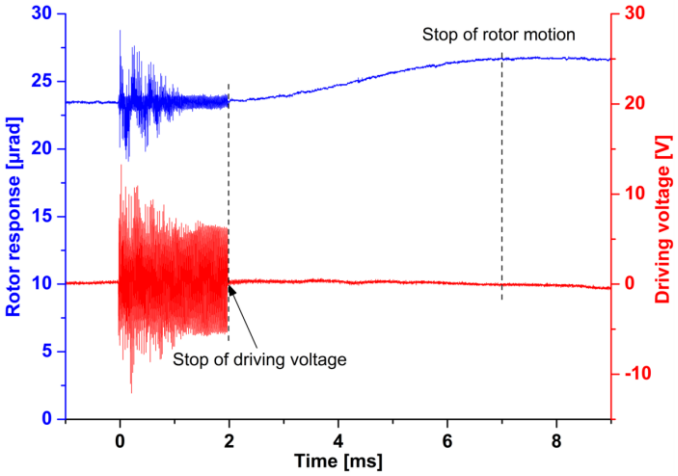

Fig. 3.21. Single minimal incremental motion step of the rotor of piezoelectric stage under the effect of driving voltage

When discussing the resolution of the piezoelectric stage, the final aspect is how this parameter is influenced by the applied external load. Because the piezostage is intended for precise and accurate positioning applications, the imparted load varied from 0 kg to 2 kg, as the absolute majority of objects potentially to be positioned will fall in this range. In this experiment, the number of trigger cycles of the driving signal was 5, and the voltage amplitude was 60 V. These values were retained for every inspected load in order to determine the response of the piezostage under identical excitation conditions. The selected values were chosen, as they are the minimal ones which induce the smallest incremental motion step. The characteristic plot (Fig. 3.22) reveals a tendency that manifests as a non-linear response of resolution with respect to applied external load. When no load is introduced, resolution is 25.7 µrad. An increase of the load to 0.1 kg leads to a

decrease in the resolution (16.3 μrad). In the presence of 0.25 kg load, the corresponding resolution equals 13.5 μrad, which is the highest value within the entire range of the applied loads. With further rise in the load (0.5 kg), the resolution decreases to 17.1 μrad. A continued rise in the applied load (1–2 kg) translates to dramatic decreases in resolution (56.6–147.3 μrad). It should be explained and concluded that the load of 0.25 kg exerts the most favourable pressure force ensuring the most uniform interaction between the rotor and the piezocylinder. That results in the appearance of the smallest incremental motion step.

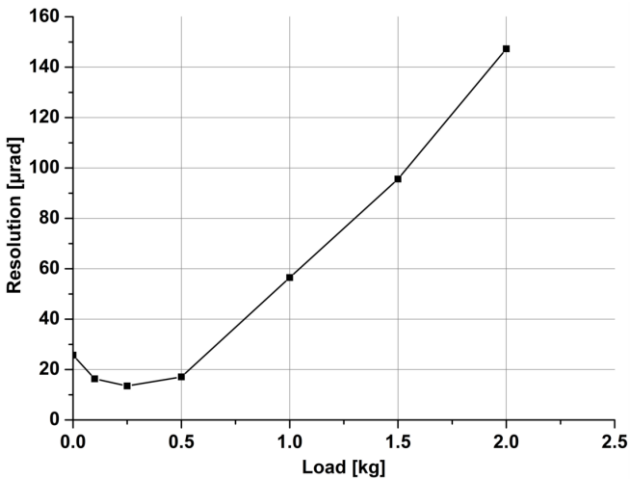

Fig. 3.22. The dependence of resolution of piezoelectric stage on the applied external load

3.5. Torque-related properties

Torque-related properties furnish one with a more explicit insight into the performance of the investigated piezostage from the point of view of system dynamics.

The experimental setup for identifying the associated characteristics is shown in Fig 3.23. As well as in the previous study, the operational resonant frequency (126.26 kHz) signal was employed to initiate the motion of the rotor. The latter component was in contact with the tension and compression force sensor of the force gauge to detect the applied compression force (load). Since it was connected to the sensor, the force gauge provided a possibility to indicate and display the values of the force, which, in turn, were utilised to find appropriate torques.

During the first experiment, the dependence of angular speed of rotor of the piezoelectric stage on the voltage supplied to the piezocylinder was analysed. External loads of 0–2 kg were imposed on the rotor. The result is depicted in Fig. 3.24. The lowest voltage allowing for a visible motion of the load-free rotor (28 rpm) reaches 20 V. A further uniform increase in the supplied voltage until 50 V entails a gradual increase in the angular speed of the rotor. The average increase rate is 0.73 rpm/V. Afterwards, this rate diminishes to 0.33 rpm/V. It means that the saturation phenomenon (i.e. a raise in the voltage provides no increase in the angular speed) is already partially observed. The same tendency manifests under the effect

of each load, but the increase rates of the rotor speed are slightly different. In the presence of the highest voltage (80 V), angular speed attains the maximal value for every given load; nonetheless, the overall top value (66 rpm) is attributed to 0.5 kg. The latter load exerts an additional pushing force ensuring even better interaction between the rotor and the PC than the load-free regime (60 rpm).

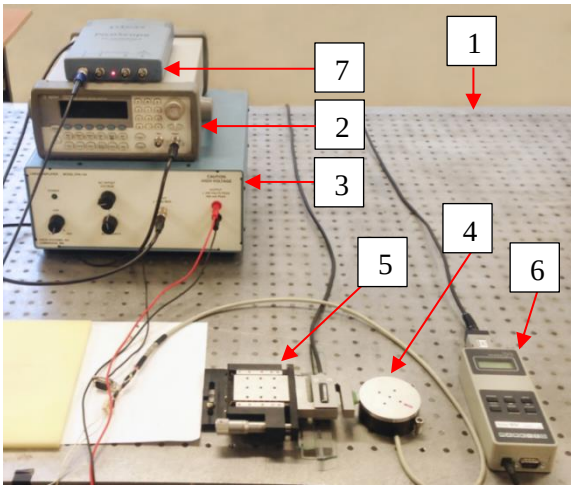

Fig. 3.23. The experimental setup for investigating torque-related characteristics of the piezoelectric stage: 1 – an optical table (1HT15-20-20, Standa Ltd.); 2 – a signal generator (Agilent 33220A); 3 – a voltage amplifier (EPA-104); 4 – the piezoelectric stage; 5 – a tension/compression force sensor (SS50); 6 – a force gauge (MARK-10, BGI series); 7 – an oscilloscope (PicoScope-3424) connected to a computer (not shown in the figure)

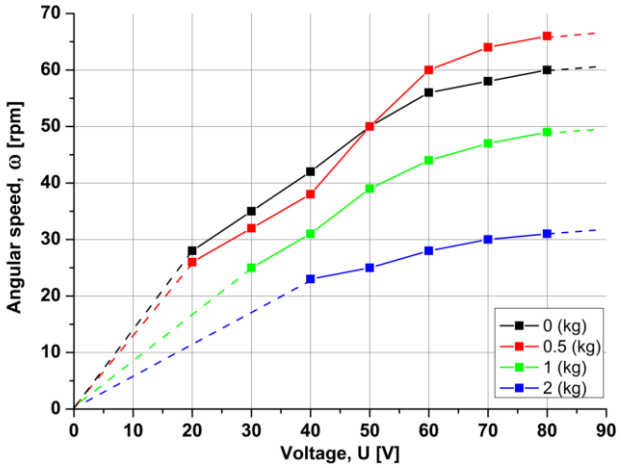

Fig. 3.24. The dependence of angular speed of the rotor of the piezoelectric stage on the driving voltage under the effect of varying external load

Attention should also be paid to the fact that speed variations in the positioning mode depend on tribological parameters of contact pairs between the contact zone elements and the rotor (see Fig. 3.2). These parameters (including surface

roughness) can be obtained by processing the signal received from the free electrodes of the piezocylinder after filtering the main signal which generates standing-wave oscillations within the PC [137].

The second investigation was concentrated on the determination of the rotor torque. In the process of measurements, the tension/compression force sensor was moved manually (i.e. by means of a special screw) back and forth in the direction perpendicular to the axis of the rotor motion. After registering the induced force values, the collected data were employed to calculate the corresponding torque values. A well-known formula [138] given below was utilised for the stated purpose.

$$T = rF\sin\theta; \tag{35}$$

here T is torque, r is the distance from the axis of rotation to force application point, F is the applied force, and θ is the lever arm angle. In order to illustrate the calculation of torque, a simplified structural scheme showing the interaction of tension/compression force sensor with the rotor is presented in Fig. 3.25.

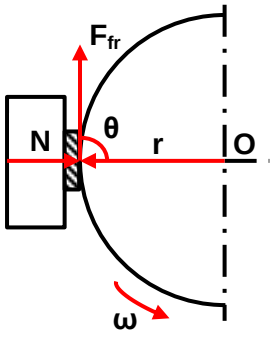

Fig. 3.25. A simplified structural scheme showing the interaction of tension/compression force sensor with the rotor

The following information was taken into account when determining the torque values. The force, which generates torque in the investigated case, is actually a friction force. All in all, a frictional resistance to the relative motion of two solid objects is usually proportional to the force pressing the surfaces together as well as the roughness of the surfaces [138]. With that in mind, the measured values of the compression force had to be respectively recomputed using the following equation [138]:

$$F_f = \mu N; \tag{36}$$

here F_f is the friction force, μ is the coefficient of friction between two contacting materials, and N is normal force exerted by one surface on the other.

The exploited tension and compression force sensor has a small tip, which contacts with the steel rotor. The end of the tip is covered with polytetrafluoroethylene (PTFE) which is better known as teflon. The friction coefficient of this material interacting with steel is, on average, equal to 0.1 [139]. This value was kept constant in all measurements of the performed analysis.

As it was stated (Eq. 36), normal force stands for the force pressing the surfaces together. Referring to this definition, it is obvious that the identified values of the discussed compression force were involved in the final calculations.

Referring Eq. (35), it is obvious that only the angle θ of the lever arm has not been considered yet. The experimental setup was prepared so that it would be possible to figure out the values of torque. Thus, the tension and compression force sensor tip was set to fully (i.e. by full surface area of the tip) contact the rotor in the direction perpendicular to the axis of the rotor motion. The adopted conditions ensured the angle θ to be equal to 90° in the analysed case.

Combining equations (35) and (36) and considering the torque calculation scheme, the next equation for determining the torque values was obtained [138].

$$T = r\mu N; \tag{37}$$

It should be noted that the distance r was maintained at 0.033 m in both of the two following experimental tests.

The characteristic plot representing the influence of the driving voltage on the rotor torque is disclosed in Fig. 3.26. Similarly to the previous plot, a uniform increase in the driving voltage from 20 V to 50 V translates into a gradual rise in exerted torque from 0 Nm to 0.0043 Nm. The average increase rate is 0.000143 Nm/V. Subjecting the piezocylinder to more than 50 V generated the torque values which on average increased by 0.000043 Nm/V. Such behaviour of the system can also be explained by the partial saturation phenomenon (see description of the previous experiment). A supply of maximal allowable electrical potential (80 V) to the PC generates the maximal torque (0.0056 Nm) of the piezoelectric stage.

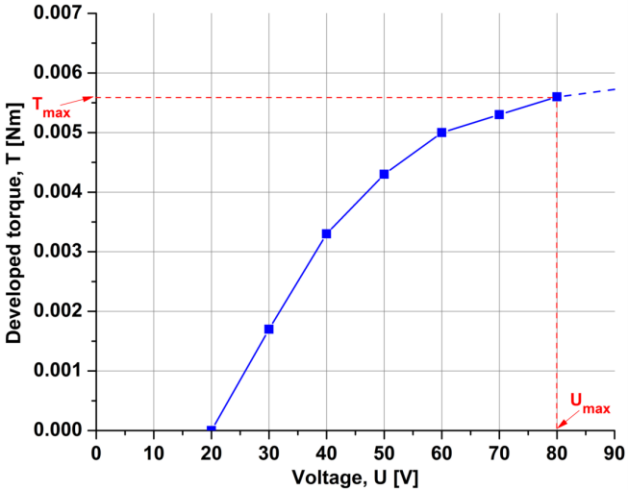

Fig. 3.26. The dependence of torque of piezoelectric stage on the driving voltage

The last inspection was executed to see how the change of the torque load affects the angular speed of the rotor, when the driving voltage is constant (Fig. 3.27). The torque load values registered during the second investigation were used for this experiment. The driving voltage was equal to 50 V. In the given plot, the

initial part of the curve (at 0 Nm) represents the starting point of the rotor motion with the angular speed reaching its peak (50 rpm). A further rise in the torque load until 0.0056 Nm imposes a gradual decrease in the angular speed. The rotor halts completely under the influence of the highest torque load at 0.006 Nm.

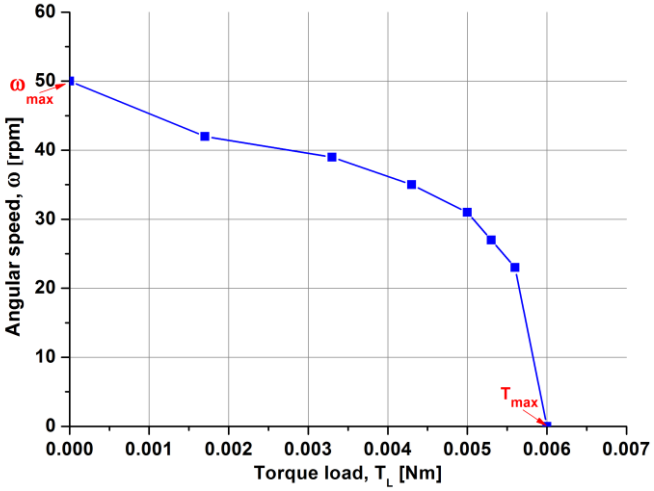

Fig. 3.27. The dependence of angular speed of rotor of piezoelectric stage on the applied torque load (U = 50 V)

3.6. Generation of torsional oscillations concomitant with rotational motion

Piezoelectric rotary positioning stages are mostly driven by ultrasonic standing- and/or travelling-wave vibrations, and there is a very limited amount of information about the generation of torsional oscillations concomitant with the rotational motion, as well as their positive influence on both the performance and use of the mentioned positioning devices. Therefore, this subchapter is intended for a concise presentation on the stated aspects.

Torsional oscillations concomitant with rotational motion can be considered as a unique dynamic operation mode attributed to a rotor of piezoelectric stage upon request. This regime should be explained in two parts; so as to illustrate both contributing components, a simplified scheme showing the topology of electrodes of the PC and two types of generated motion is provided in Fig. 3.28.

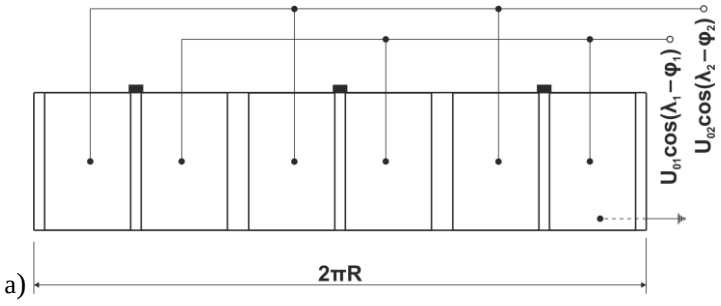

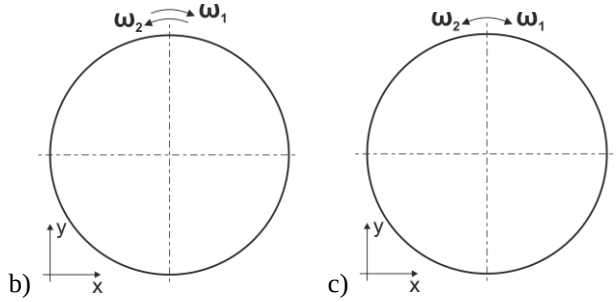

Fig. 3.28. A layout of topology of electrodes of piezocylinder (a) and a schematic representation of the rotor in two possible motion types: rotational (induced by standing-wave oscillations) (b) and scanning-type (induced by torsional oscillations) (c)

Let us assume that there is an opportunity to supply two harmonic electrical signals ($U_1(t)$ and $U_2(t)$) of certain amplitudes and frequencies to a desired group of electrodes. Signal expressions are presented in (38) and (39) [70]:

$$U_1(t) = U_{01}\cos(\lambda_1 t - \varphi_1), \tag{38}$$

$$U_2(t) = U_{02}\cos(\lambda_2 t - \varphi_2); \tag{39}$$

here U_{01}, U_{02} are the voltage amplitudes, λ_1, λ_2 are the angular frequencies, t is the time, and φ_1, φ_2 are the phases of harmonic signals. Let us assume that one signal at a time (say, $U_1(t)$) is supplied to a randomly chosen group of electrodes. The ordinary standing-wave vibrations are formed, imposing continuous rotor motion in the clockwise/counter-clockwise direction (Fig. 3.28b). If both signals of the same amplitudes but different frequencies ($U_{01} = U_{02}$, $\lambda_2 > \lambda_1$ and $\lambda_2 - \lambda_1 \ll \lambda_1$) are applied to both groups of electrodes at the same time, the torsional oscillations are induced, generating scanning-type rotor motion (Fig. 3.28c). Combining the mentioned types of motion, torsional oscillations concomitant with the rotational motion are formed. This can be achieved by using two signals of different amplitudes ($U_{01} \neq U_{02}$) and frequencies (the same conditions as previously). In such situation, the moving member (rotor) performs a periodic motion defined by the following law [70]:

$$A = A_{max}\cos\left(\frac{\lambda_2 - \lambda_1}{2}t\right); \tag{40}$$

here A_{max} is the maximal amplitude and t is the time of torsional vibrations with rotational motion. Harmonic oscillations are excited in the frequency range starting from 0 Hz, when $\lambda_2 = \lambda_1$ ($A = A_{max}$). The frequency of vibrations is controlled by the value $\lambda_2 - \lambda_1$.

The mode defined by Eq. (40) could be used in diverse precision shakers designed for calibrating optical transducers and optoelectronic devices (e.g., laser beam scanners) or stirring liquid chemical substances in a laboratory vessel. Another application might be orthodontics, where there is a need to dense a liquid plaster cast mass (i.e. to vanish pores inside the mass) filled into a special dental imprint form placed on the vibrotable. However, the value of A_{max} should be increased from

order of 10^{-6} m to 10^{-3} m so as to achieve the desired effect.

In order to demonstrate the feasibility to generate torsional oscillations concomitant with rotational motion, an additional rotary piezostage based on the same operation principle as the major one was produced. A schematic design of the actuator is given in Fig. 3.29, with the working description elaborated herein. The stage (Ø66 × 15 mm) contains a rotor (*1*) (Ø66 × 5 mm) contacting with the piezoring (*3*) (Ø40 × Ø32 × 5 mm, Ferroperm Pz26) via contact zone elements (*2*) (three equally displaced units) and (*5*) (two units displaced by 120°). When rotational motion takes place, these five supporting points become vibroactive which reduces the resisting moment of friction forces significantly. Axial attraction magnets (*4*) (three equally displaced units) and the radial attraction magnet (*6*) ensure the necessary contact between the piezoring and the rotor in the respective directions. In addition, the exact position of the rotor with respect to both its axis of rotation and the plane perpendicular to its axis of rotation is maintained. The piezoring is composed of two groups of sectioned electrodes, the topology of which coincides with the one that was implemented in the main designed rotary stage (see Fig. 2.3). A supply of operational high-frequency harmonic excitation signal to one group of electrodes initiates rotational motion in the clockwise direction; the excitation of the other section generates reverse motion.

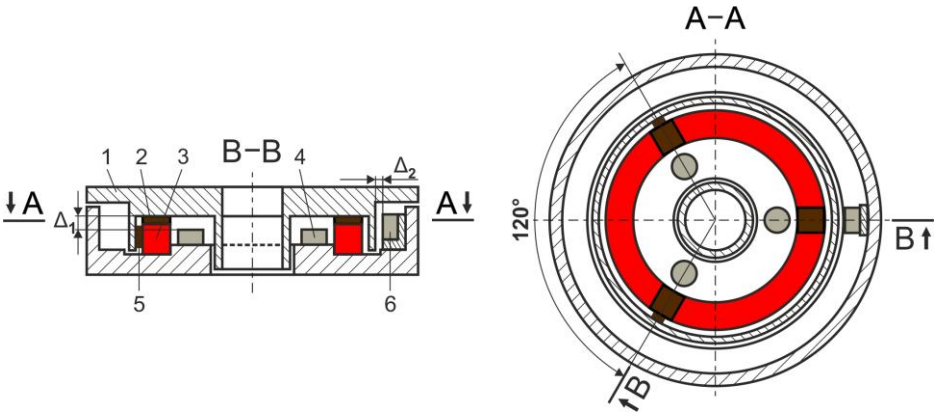

Fig. 3.29. A schematic design of the piezoelectric rotary stage powered by two high-frequency harmonic excitation signals: 1 – the rotor; 2, 5 – contact zone elements; 3 – a piezoring; 4 – axial attraction magnets; 6 – a radial attraction magnet; Δ_1, Δ_2 – air gaps of axial and radial attraction magnets, respectively

In order to determine the operational AC frequency of the investigated object, the Wayne Kerr 6500B (Fig. 3.30) impedance analyser was employed. The obtained response of electric impedance and phase angle of the piezoring within the measured frequency range is shown afterwards (Fig. 3.31). There are two resonant frequency intervals (around 45 kHz and 99 kHz) at which the curves of impedance and phase angle undergo remarkable changes in terms shape and values. In this case, the resonant frequency of 45.5 kHz was found to lie in the first examined range and was confirmed as the operational one. Nevertheless, it should be noted that the rotary piezostage can also operate in the range of approximately 45–47 kHz.

The experimental setup given in Fig. 3.32 was utilised to analyse the dynamic properties of the stage with respect to induced torsional oscillations-related motion.

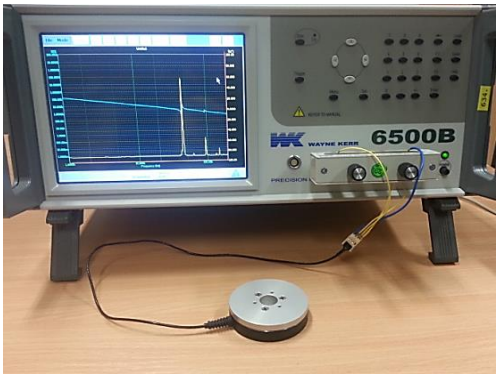

Fig. 3.30. Determining the operational frequency of the piezoelectric rotary stage (by impedance analyser Wayne Kerr 6500B) required to generate torsional oscillations

Initially, two harmonic excitation signals ($U_1(t)$ and $U_2(t)$) of equal amplitudes but different frequencies (i.e. $U_{01} = U_{02}$, $f_1 \neq f_2$) were supplied to both groups of electrodes of the piezoring at the same time. Three waveforms of rotor vibrations of the tested piezostage were obtained in the presence of constant voltage amplitudes ($U_{01} = U_{02}$ = 60 V). All of them denote the scanning-type motion generated by torsional oscillations, with no rotational motion present. The first one (Fig. 3.33a) exhibits the maximal vibration amplitudes (peak-peak) approximately equal to 161.7 mrad when the difference in applied frequencies is 2 Hz. The waveform is rather uniform, but there exists a slight discrepancy in shape of the curve at the top right side of every positive peak denoting the moment after reversal of motion direction. It can be explained by an imperfection in system design, tribological properties between the contact zone elements and rotor, and the resonance of piezostage. In Fig. 3.33b, a response of the rotor is illustrated, when the difference in excitation frequencies reaches 74 Hz. The vibration amplitudes (peak-peak) achieve 0.051 mrad; that is much less compared to the result described before.

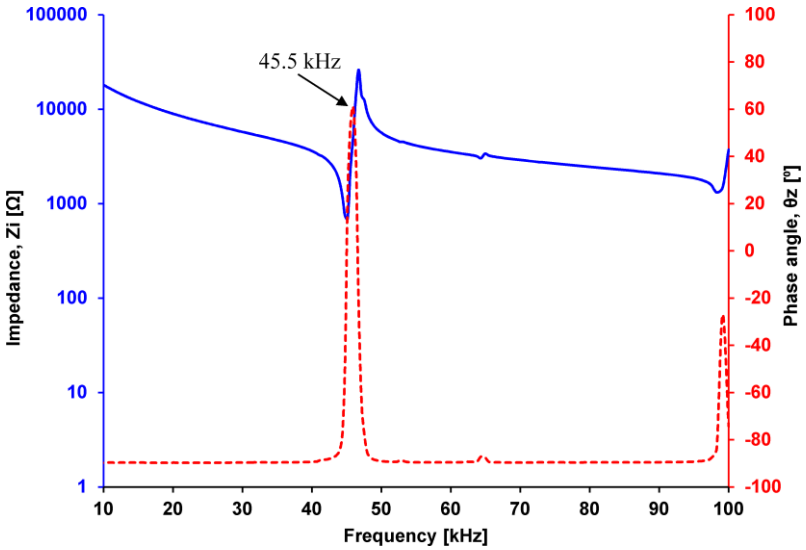

Fig. 3.31. The impedance and phase angle of the piezoring vs excitation frequency (operational resonant frequency is 45.5 kHz)

The plot is characterised by the same discrepancy as in Fig. 3.33a, just of a higher extent. The minimal vibration amplitudes (peak-peak) of 0.028 mrad are attributed to the last plot (Fig. 3.33c). They are induced by the difference of 500 Hz in the employed frequencies. Though periodic motion is retained, the resulting curve is featured by a wave-type trajectory due to the highly increased influence of the structural resonance of the piezoelectric stage. On the other hand, it should be noted that the effect of the discussed discrepancies is reduced to a minimum here.

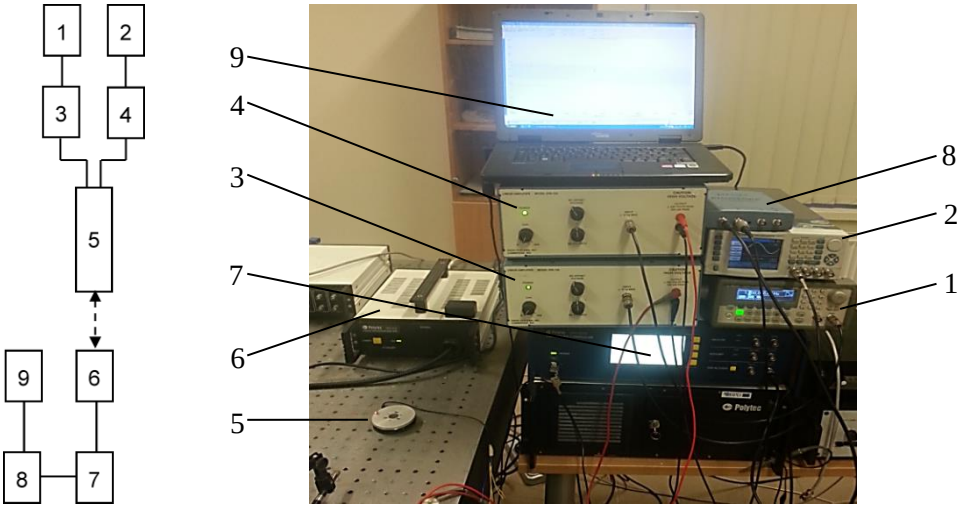

Fig. 3.32. The experimental setup for investigating the rotary dynamic characteristics of the piezostage with respect to induced torsional oscillations concomitant with rotational motion: a) a simplified structural scheme; b) actual components (1, 2 – signal generators (Agilent 33220A, Tabor WW5064); 3,4 – voltage amplifiers (EPA-104); 5 – the piezoelectric stage on an optical table (1HT15-20-20, Standa Ltd); 6 – a fibre optic interferometer (Polytec OFV-512); 7 – laser Doppler vibrometer controller (Polytec OFV-5000); 8 – an oscilloscope (PicosScope-3424); 9 – a computer)

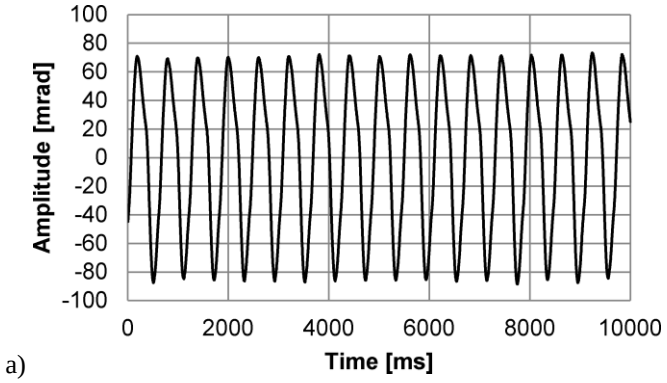

a)

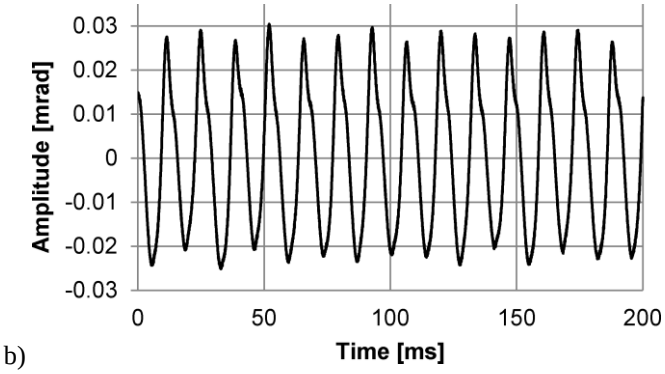

b)

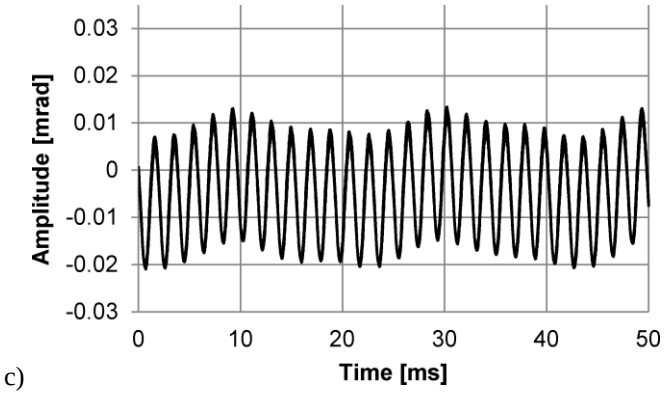

c)

Fig. 3.33. The waveform of torsional oscillations of rotor: a) maximal, at frequency of 2 Hz (f_1 = 44100 Hz, f_2 = 44102 Hz, $U_{01} = U_{02}$ = 60 V); b) intermediate, at frequency of 74 Hz (f_1 = 44100 Hz, f_2 = 44174 Hz, $U_{01} = U_{02}$ = 60 V); c) minimal, at frequency of 500 Hz (f_1 = 44100 Hz, f_2 = 44600 Hz, $U_{01} = U_{02}$ = 60 V)

A possibility to generate the torsional vibrations concomitant with rotational motion of the rotor is illustrated in the Fig. 3.34. As it was mentioned at the beginning of this subchapter, the latter regime is only feasible if both the amplitudes and frequencies of two simultaneously supplied harmonic excitation signals are not the same, i.e. $U_{01} \neq U_{02}$, $f_1 \neq f_2$. The following values of signals were chosen for this inspection: $U_{01} = 25$ V, $U_{02} = 30$ V, f_1 = 44100 Hz, f_2 = 44130 Hz. As a result, a slow (approximately 0.0065 mrad/s) rotor motion was obtained. This characteristic is very preferable in precise and accurate positioning systems. If there is a need to change the speed, it can be achieved by setting higher/lower values of voltage amplitudes. By increasing/decreasing the difference in frequencies, it is possible to reduce/raise the amplitudes of angular displacement. The emphasis should also be placed on the capability of bidirectional rotational motion in this case.

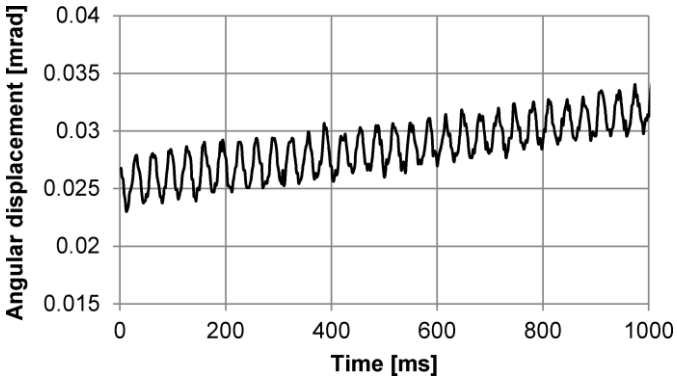

Fig. 3.34. The waveform of torsional oscillations concomitant with the angular displacement of rotor; the frequency of vivrations is 30 Hz (f_1 = 44100 Hz, f_2 = 44130 Hz, U_{01} = 25 V, U_{02} = 30 V); the angular speed of rotor is 0.0065 mrad/s

3.7. Chapter conclusions

The main conclusions of this chapter are:

- Impedance measurement revealed potential operational regime limits of the piezoelectric stage to be equal to 125–134 kHz for both rotational directions. 3D scanning LDV showed that the operational resonant frequency of 126.26 kHz induces tangential and axial displacements of the top surface of the piezocylinder, thus generating elliptical motion trajectories of the contact zone elements in clockwise and counter-clockwise directions; the trajectories attributed to other spatial planes also attain well-defined shapes. The relationship between applied voltage amplitudes (20–80 V) and induced motion trajectories demonstrated that a supply of higher electrical potential to the PC leads to higher displacement amplitudes of the contact zone elements. The highest displacement amplitudes are registered in the tangential direction (for both rotational cases), so the respective oscillations are confirmed to be the driving ones in all range of applied voltage amplitudes.
- The assessment of surface displacement of the PC by holographic interferometry indicated the suitability of both the selected topology of electrodes and excitation type for a uniform displacement of the top and side surfaces. That, in turn, can potentially lead to the generation of well-defined motion of the rotor of the designed piezoelectric stage in both rotational directions. Due to slightly shifting nodal zones (caused by motion reversal) in the excited electrodes, the exact constant positions for three contact zone elements and supporting base elements cannot be precisely determined.
- The values of average resolution of the developed piezoelectric stage are 0.250 μrad (clockwise rotation) and 0.258 μrad (opposite motion); that makes the device superior to most of competitive products on the market. The dependence of resolution on the applied external load (0–2 kg) was found to be non-linear, with the maximal resolution observed at 0.25 kg; a

further increase in the load until maximum results in the generation of about 11 times lower resolution.

- The inspected torque-related properties firstly showed the influence of driving voltage (20–80 V) on angular speed (28–66 rpm) of the rotor under effect of varying external load (0–2 kg); the non-linear tendency for the speed to rise, when the supplied voltage increases, was determined. Afterwards, a tendency for rotor torque to non-linearly increase with the increase in the driving voltage was defined. Lastly, the dependence of the angular speed on the induced torque load under constant driving voltage disclosed a non-linear tendency for the rise in the torque load to impose a decrease in the angular speed.
- The dynamic operation mode characterised by the generation of torsional oscillations concomitant with rotational motion of the rotor was exhibited. The novel mode was elaborated using an additional piezostage based on the same operation principle as the major one but with lower excitation frequency (44–46 kHz). The generated mode is featured by slow bidirectional rotational scanning-type motion of rotor, thus very preferable in high-precision positioning systems.

4. FABRICATION AND CHARACTERISATION OF POLYMERIC ROTARY INCREMENTAL SCALES

Although it is well-known that glass-chromium rotary incremental scales are considered as the most suitable option for angular displacement measurement in precise positioning systems, modern micro- and macro-applications often require readily-available materials and cutting-edge techniques, since conventional means cannot always satisfy the constantly growing commercial demands, where the reduction of production costs is among the top priorities. Companies representing the high-precision sector (e.g., Precizika Metrology, Lithuania) are constantly trying to solve this problem and seeking for potential alternatives. In this case, a combination of polymeric material and bulk microfabrication technology was proposed by Kaunas University of Technology. The exploited method provides a possibility to obtain novel periodic microstructures featured by compactness, high quality, and low cost. The replacement of glass-chromium grating scales used in conventional high-precision rotary interferential and/or moiré-type encoders (see Subchapter 1.5) by the proposed polymeric ones could potentially offer a more favourable cost-performance ratio. An appropriate modification of scales (i.e. metallisation of surfaces of gratings) would enable them to fulfil the functions of reflective gratings as well. Thus, they could be adapted to the newly designed high-resolution piezoelectric rotary stage, where angular displacement is determined by a reflective optical encoder.

This chapter provides the information regarding the fabrication and characterisation employed in the research of polymeric rotary incremental scales.

Determination of geometric and material data for analysed objects

It was decided to fabricate two identical polymeric scales, with each one on separate square-shaped PET substrate (50 × 50 mm^2). The outer diameter of the scales was aimed to be 20 mm, with the corresponding diameter of raster (strip) pattern of the scales being 19 mm, the internal diameter being 17 mm, and the width of strips equal to 10 μm (according to the pattern of an employed photomask). PET was selected as a substrate material due to the acceptable combination of optical and mechanical properties, such as optical clarity, lightness, mechanical strength, etc. (for a more detailed motivation, please refer to Section 1.6.2). The thickness of PET film was selected to be 200 μm to ensure the simultaneously necessary mechanical stability and compactness of the scales.

The decision was also made to produce the same scales of increased diameter and different strip period later on, if the quality of the obtained ones was high enough. In particular, from the point of view of application, the following tasks for each fabricated polymeric scale were formed:

1) The dimensions of the strips of periods should be as equal as possible.
2) The surface profile of the grating should be as even as possible.
3) The optical transmittance should be as high as possible.
4) The values of diffraction intensity should be highest in the -1, 0, +1 orders.

4.1. The fabrication process and its peculiarities

The fabrication of polymeric incremental scales was divided into two steps: 1) the formation of a silicon master mould by using optical microlithography and reactive ion etching (RIE); 2) the formation of an angular raster pattern in the polymeric substrate by employing the UV imprint technique. The latter method was presented in greater detail in Section 1.6.1. The fabrication process is revealed in Fig. 4.1, with the steps separated in parts (a) and (b), respectively.

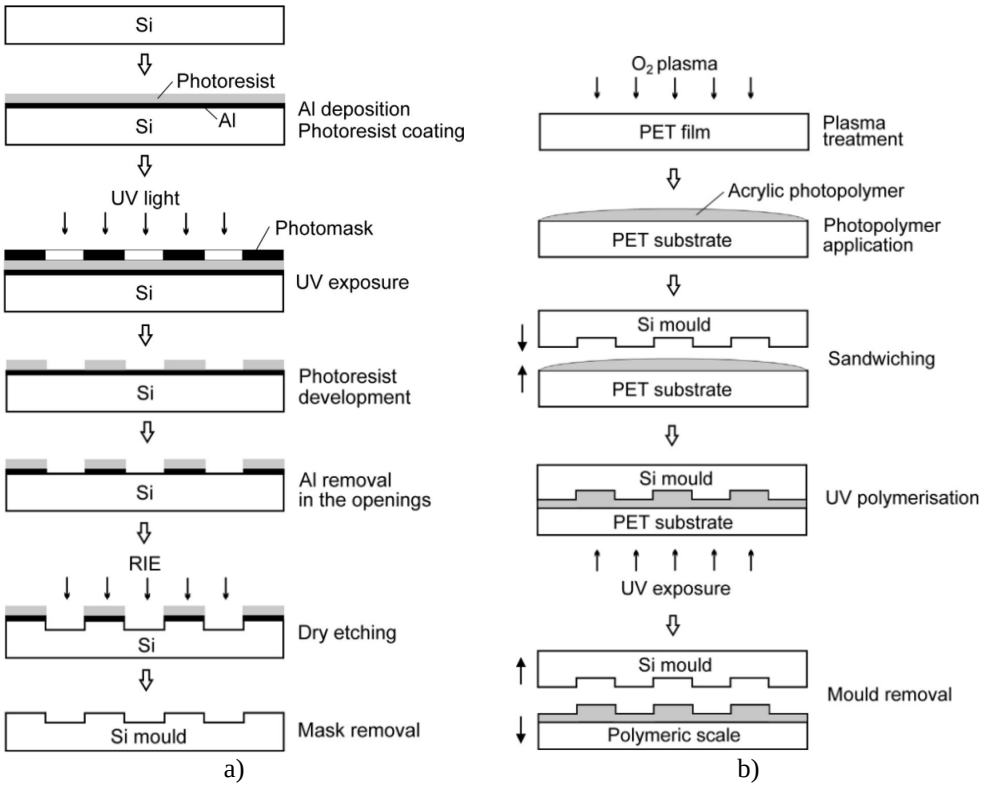

Fig. 4.1. The fabrication of polymeric incremental scales divided into steps: a) the formation of a silicon master mould by using optical microlithography and reactive ion etching; b) the formation of an angular raster pattern in the polymeric substrate by using the UV imprint technique

The formation of a silicon master mould

To start with, a single-crystal <100> Si wafer (30 × 30 mm^2) of thickness equal to 500 μm was used as the substrate when forming the master mould. For this purpose, optical microlithography was mainly employed. Generally, 'microlithography' is a term used to describe various techniques for creating incredibly small structures usually ranging in size between 1 μm and 100 μm. These include many integrated circuit-related elements, microelectromechanical (MEM) and microoptoelectromechanical (MOEM) systems [140–141].

The formation of the Si master mould was carried out following these steps:

1) A proper cleaning of substrate was performed in the beginning. The substrate was treated chemically (i.e. immersed in a vessel of boiling acetone and kept for about 2 min) and by RF (13.56 MHz, 0.3 W/cm^2) O_2 plasma in a specialised vacuum chamber for approximately 7 min.

2a) The second operation was coating of specimens with a sacrificial layer of aluminium (100 nm) formed utilising a vacuum vapour deposition device YBH-71D3. This was done due to the need to form an effective mask for the RIE executed at the end of the master mould fabrication.

2b) Photoresist coating took place by using a Dynapert Precima spin coating machine (Fig. 4.2a). The cleaned Si wafer was placed on the milliporous filter laid onto the main plate of the centrifugal device (Fig. 4.2b). Then a positive photoresist (ma-P 1225) was dispensed on the wafer (Fig. 4.2c). Spinning the substrate at 3000 rpm for 20 s led to the formation of a uniform thin film (about 2.5 μm) of photoresist over the entire surface of the specimen. A constant position of the filter and specimen with respect to the rotating platform is ensured and retained by air suction through the very small nozzle at the centre of the platform.

2c) 'Soft baking' was carried out to make the photoresist more viscous. That was achieved using infrared rays by using the conveyor-type furnace LADA. The desiccation system was adjusted to affect the sample at the temperature of approximately 100°C for about 10 min. When the wafer was taken out of the machine, it was kept to cool down until the next operation.

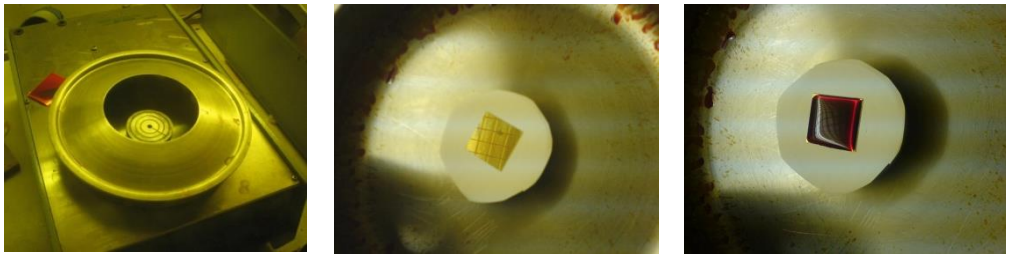

a) b) c)

Fig. 4.2. Preparation of Si wafer for coating by photoresist: a) the spin coating machine Dynapert Precima; b) a milliporous filter and a Si wafer on the rotary platform; c) the Si wafer with a dispensed photoresist ready for spin coating

3) The photomask was aligned and exposed using UV light. It is one of the critical steps in optical microlithography, particularly, because of both the quality of the photomask, and the accuracy of the photomask superpositioning with respect to the specimen. These factors directly relate to the quality of the final structure to be formed in the required location of the wafer. Chromium-on-glass photomask (Fig. 4.3a), which is common in the production of glass rotary incremental scales, was used in this work as a template of raster pattern. The external diameter of the photomask pattern was 30 mm. The external and internal diameter of raster pattern of the photomask was 19 mm and 17 mm, correspondingly. The thickness of chromium evaporated on the glass was 70 nm. Black areas in this picture represent zones fully coated by chromium. Light areas are zones of uncoated float glass. The

dark grey ring stands for the raster pattern formed of chromium strips. A detailed analysis of the raster zone carried out by using an optical microscope revealed that the width of the strips was fixed and equal to 10 μm, while the value of gaps between the strips varied from 10 μm to 14.2 μm when approaching from the centre of pattern to its outer edge. A fragment of the photomask pattern near the inner edge of the raster zone is presented in Fig. 4.3b.

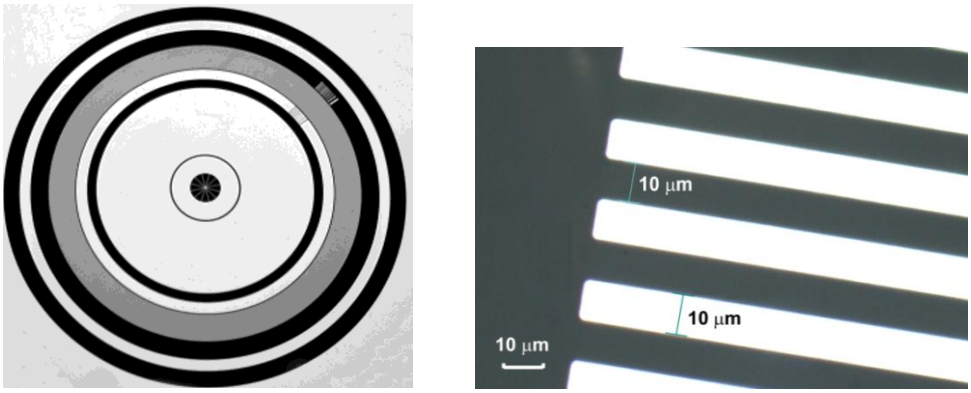

a) b)

Fig. 4.3. Optical microscope images of: a) glass photomask; b) fragment of raster zone (dark grey colour denotes chromium strips; white colour denotes gaps between the strips)

The alignment of the given photomask and UV exposure was achieved using the specified JUB 76G system (Fig. 4.4). The wafer was affected with UV light (wavelength of 365 nm) for approximately 15 seconds.

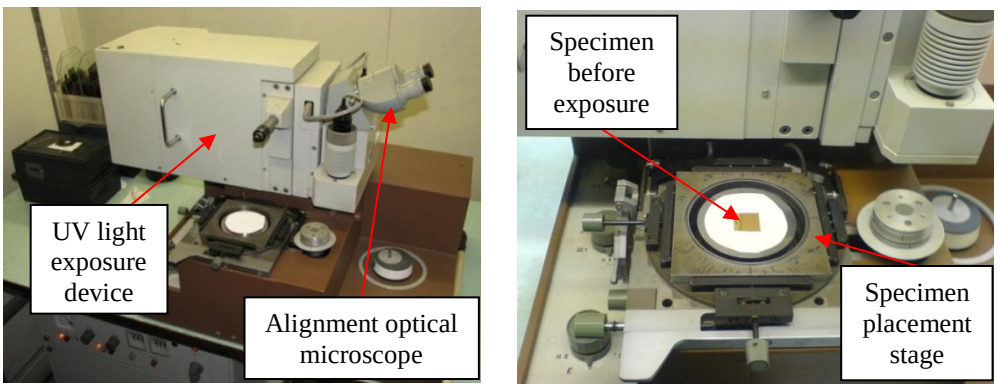

Fig. 4.4. Photomask alignment and JUB 76G UV exposure system

4a) During the next operation (photoresist development), the wafer was immersed into a vessel containing developer (ma-D351), kept for about 25 s, taken out, thoroughly rinsed in deionized water, and dried with a stream of compressed air. This process allowed to remove the areas of photoresist affected by the UV light.

4b) Thermal hardening (‘hard baking’) of the wafer was executed using the already presented LADA desiccation system in the presence of the same technical regime parameters as in the ‘soft baking’ step. This provided the remaining

photoresist with supplementary firmness and conditioned the reduction of standing-wave phenomena caused by destructive and constructive interference patterns of the incident light during UV exposure.

5a) Then the thin effective masking layer resulting from the previous operation was removed. In this experiment, thin Al film was etched by Cr_2O_3:NH_4F:H_2O solution, with the specimen being put into a low-profile vessel containing the liquid.

5b) The last step before proceeding to the dry etching process was the elimination of photosensitive material domains. For that reason, a Si wafer was submerged into the vessel with the developer (mr-Rem 660) for about 1 min. Then the specimen was washed with deionized water and taken for visual quality inspection.

6) In order to etch the bulk of Si at low rates and thus, form the periodic microstructure of required low-depth, reactive ion etching was employed. This method can be defined as an influence of high-frequency low-temperature gaseous plasma and ions on the substance (wafer) to be etched [140]. The plasma is generated by an electromagnetic field in the presence of vacuum. Being one of the most applied dry etching methods, RIE is often exploited in diverse process steps of surface/bulk micromachining to form simple or complex micro-/nanostructures. The etching operation was performed utilising the PK-2420RIE equipment that is capable of generating reactions necessary to produce a constant physical and chemical etching environment in the vicinity of wafer surface. During the experiment SF_6, gas enabled the generation of RF (13.56 MHz) plasma, with the power density equal to 0.3 W/cm^2, to obtain the grooves of grating in Si substrate. Pressure in the vacuum chamber was 40 Pa.

7) Finally, the residual Al thin film was removed. By repeating the process described earlier, Cr_2O_3:NH_4F:H_2O mordant helped in vanishing the sacrificial layer completely.

The formation of an angular raster pattern in the polymeric substrate

The second part of fabrication of polymeric scales is the formation of an angular raster pattern in the polymeric substrate by using the UV imprint technique; its benefits were emphasised in Section 1.6.1.

In order to obtain the scales, a commercial acrylic photopolymer (trimethylolpropane ethoxylate) was employed for imprint experiments, since it is characterised by sufficiently high optical transparency and a refractive index akin to that of PET, thus reducing the possibility for light reflection to occur at the interface of PET-photopolymer. The applied photopolymer also offers a superior hydrolytic stability, as well as acceptable balance between hardness and flexibility.

Firstly, the substrates were treated by O_2 gas plasma (frequency of 13.56 MHz, plasma power density of 0.45 W/cm^2) in a vacuum chamber for 1 min so as to clean the surfaces and improve the adhesion of coating. Then the substrates were coated with a photopolymer forming a layer of 3 μm. The polymeric replicas of the Si master mould were made by using UV light irradiation (curing) of the photopolymer layer sandwiched between the mould and PET substrates. For this to be accomplished, a high-pressure DRT-230 mercury lamp (wavelength of 360 nm,

luminous emittance of 10^4 lx) was used as a source of UV irradiation. The distance from the lamp to the exposed photopolymer layer was equal to 10 cm. Each replica underwent 60 s of UV exposure before separating it from the Si master mould.

4.2. Characterisation of the fabricated polymeric scales

4.2.1. Visual inspection and moiré phenomenon

For finding out whether the fabrication process was successful, several pictures of the obtained grating structures were taken using an optical microscope as a primary visual inspection tool.

Visual inspection is one the most significant and powerful ways to determine the quality of fabricated microstructures (including periodic ones) relatively fast even during their massive production.

Taking into account the stated facts, a computer-controlled optical upright metallurgical microscope Optika B-600MET with a c-mount 2560 × 1920 resolution (5.0 Mpixel) camera (Optikam Pro 5LT) was used to evaluate the formed scales and measure the periods of their gratings.

Arbitrary fragments of two scales were elected to examine the quality of the formed raster pattern (Fig. 4.5). As the visual inspection reveals, the fabrication process resulted in periodic microstructures, with the edges of strips being thin, sharp, and uniform. Nevertheless, some minor defects (micro-irregularities and microdots) can be visible as well. The grating period of both scales was defined to be approximately 21 μm. In spite of that, the values of width of both of the imprinted strips and gaps between them are different; the width of strips is about 11 μm, and the gap is about 10 μm for Scale (1). When inspecting Scale (2), these values were found to be 12 μm and 9 μm, respectively. However, one should be aware of the fact that the registered values are attributed to the tops of the strips (hills) and bottoms of the gaps (grooves), since the microscopic images are formed when observing perpendicularly with respect to the specimen position.

When analysing the presented images, it can be observed that fabrication was quite successful, although some micro-irregularities and defects are observed. Taking into consideration the theoretical and practical knowledge, the most probable reasons for that could be as follows:

1) A microdistorted surface of Si master mould.
2) Dust that appeared on the surface of the photopolymer during the formation process.
3) Technological limitations of UV imprint equipment.

Fig. 4.6 gives a comparative view in terms of quality between the angular raster patterns of chromium-on-glass photomask, formed Si master mould, and the fabricated polymeric scale. It can be observed that the strips are mostly uniform in case of the photomask. The quality of the raster elements slightly degrades when the pattern is transferred to Si substrate. Nonetheless, nearly no difference in terms of the pattern is determined between the master mould and the polymeric scale. Therefore, it can be preliminary stated that the PET-based grating scales were formed properly.

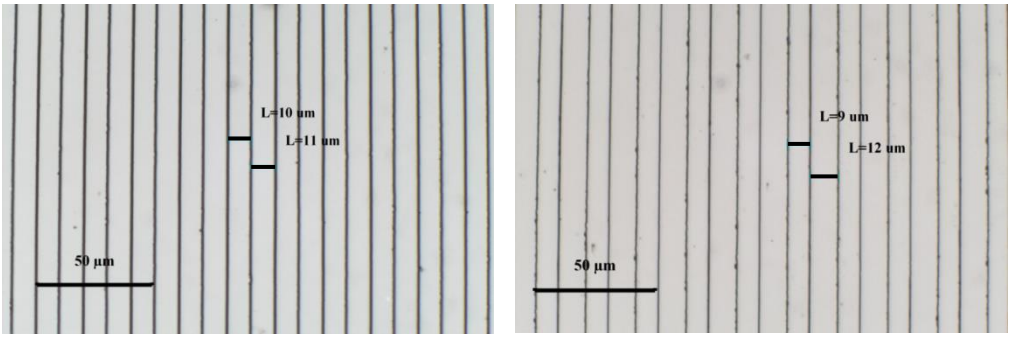

a) b)

Fig. 4.5. A fragment of an angular raster pattern of: a) polymeric incremental Scale (1); b) polymeric incremental Scale (2); (Periods – 21 µm); (Magnification – 750x)

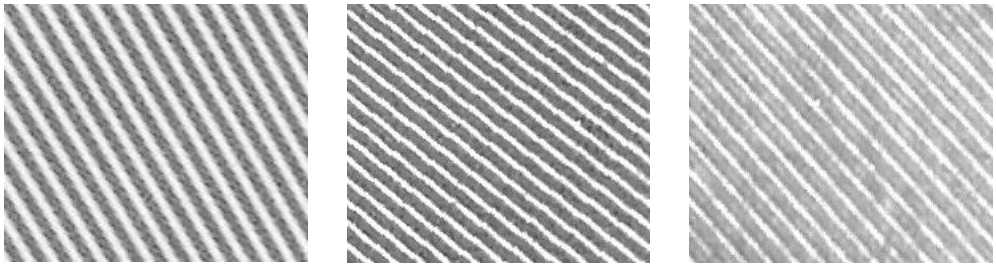

a) b) c)

Fig. 4.6. Images of fragment of angular raster pattern of: a) a chromium-on-glass photomask; b) a formed single-crystal <100> Si master mould; c) the fabricated polymeric scale

As it was discussed in Subchapter 1.6, one of the ways to detect angular displacement in high-precision rotary stages and positioning systems is the moiré effect. Although the fabricated polymeric scales were intended for interferential or reflective-type encoders (the latter option will be disclosed at the end of this subchapter), an opportunity to make use of the moiré fringes is briefly presented here, because the formed periodic microstructures are fully suitable for that purpose. By replacing the optical head and appropriately modifying the existing unit of displacement read-out, it would be also possible to adapt such principle in the developed high-resolution piezoelectric rotary stage presented in this thesis.

During the visual inspection of the fabricated scales, a proper combination (overlay with a shift) of gratings led to the formation of moiré fringes (Fig. 4.7). If the accurate distance between two dark zones was identified and registered correctly, it could be utilised to indicate a precise (micrometer or higher order) angular displacement of a system upon request.

For a more obvious illustration of possible moiré application, two radial gratings (Fig. 4.8) were modelled with the MATLAB software, assuming that one of them (20 µm period, 3140 lines per all circle) is fixed to the rotating part of positioning system, and another one (21 µm period, 2990 lines per all circle) acts as a reference (i.e. remains stationary). A fragment of the simulated moiré pattern is given at the bottom of Fig. 4.8a. In this case, the distance between the dark zones is

equal to 430 μm. Depending on the sensitivity and accuracy of the sensor used in the positioning system, this distance could be changed by applying different period gratings. When Grating (*1*) is rotated (e.g., clockwise) with respect to Grating (*2*), the appearing moiré fringes 'move' in the same direction (Fig. 4.8b). Observing the pattern at 0.215 s shift, it is clear that every dark zone is 'displaced' by 100 μm, and the distance between the dark zones pertains to be 430 μm. When a 0.43 s shift takes place, the white zones appear instead of the dark ones comparing to the no-shift image. The same tendency in terms of both 'displacement' of each dark zone and the distance between the neighbouring dark zones is retained in the presence of 0.645 s shift. After 0.86 s of rotation, the dark fringes are observed at the initial (no-shift) position, and at exactly the opposite zones comparing to the 0.43 s shift. It means that using a sensor which is sensitive enough to bright and dark zones, the accuracy of 0.43 s could be reached.

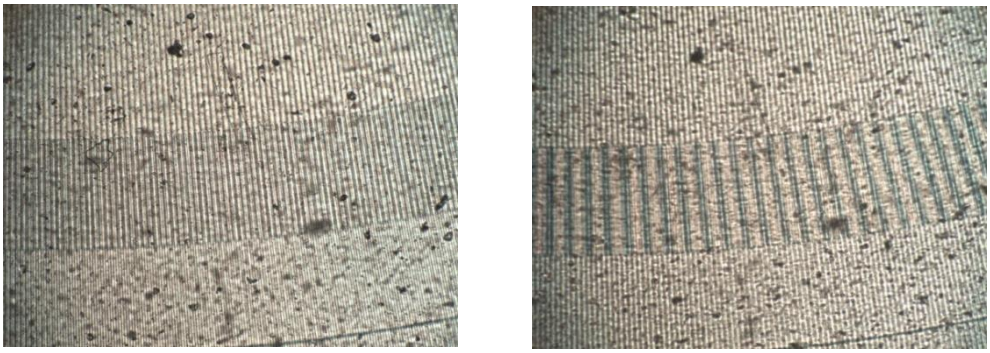

a) b)

Fig. 4.7. a) Fragments of two overlaid polymeric incremental scales with no moiré pattern; b) a fragment of moiré pattern appearing when two scales are overlaid and one of them is rotationally shifted with respect to another; (Magnification – 75x)

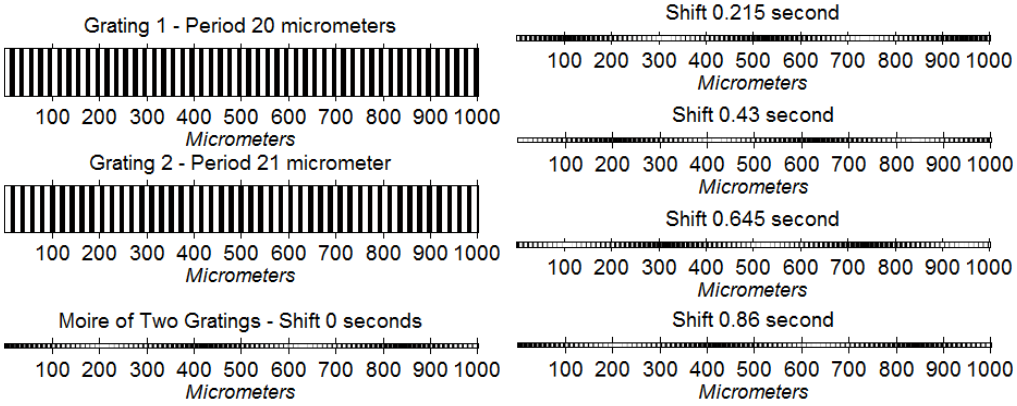

a) b)

Fig. 4.8. Images of: a) two modelled gratings (periods of 20 μm and 21 μm) and their geometrical moiré pattern at 0 s; b) geometrical moiré patterns of respective gratings when Grating (1) is overlaid and rotated by 0.215 s, 0.43 s, 0.645 s and 0.86 s with respect to Grating (2)

It should be emphasised that measurement accuracy is not influenced by a place where the appropriate optical signal reaches the scales, i.e. e.g., distances of 6 mm, 7 mm or 8 mm from the centre of the system lead to the same results. Such property is determined by the radial grating itself. Only the distances between dark fringes vary. For instance, this distance is 406 μm at 8.5 mm from the centre, and distance of 454 μm is observed at 9.5 mm, correspondingly.

4.2.2. Surface morphology analysis

Because the fabricated polymeric scales are meant to be used as one of the substantial elements devoted to registering angular displacement in high-precision rotary encoders, stages or positioning systems, their surface should be as smooth as possible in order to obtain the desired optical characteristics.

In this experimental investigation, an atomic force microscope (AFM) was employed to analyse the surface morphology of the specimen down to the atomic level with a high resolution. The mean height of the surface, the average roughness, root mean square roughness, valley depth, peak height, peak-valley height, etc. was measured to evaluate various micro-irregularities of surfaces upon interest.

Surface morphology of the silicon master mould and fabricated polymeric scales was analysed by AFM Nanosurf easyScan 2 (Fig. 4.9). All measurements were carried out in the static force operating mode, with the scanning resolution being 256 × 256 points, the value of controller set point equal to 10 nN, and the mounted cantilever ContAl-G (contact mode probe with Al reflex coating). So as to reduce the generation of measurement artefacts, the probe scanning direction was selected to be perpendicular to the top surface of formed step-profile structures. A heavy stone table and a special box were applied to decrease the effect of external vibrations, noise, and light. Nanosurf Easyscan 2 software was used for data processing, visualization, and analysis.

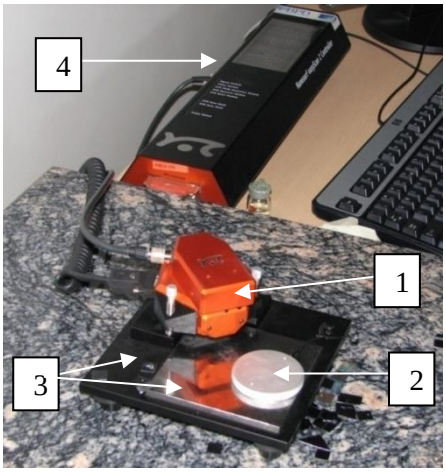

Fig. 4.9. AFM Nanosurf easyScan 2. Parts: 1 – a scanner with a video camera; 2 – a sample holder; 3 – a a sample stage; 4 – the controller

The views of both AFM 3D topography and the profile of the PET surface, with no plasma treatment and after O_2 plasma treatment, are presented in Fig. 4.10, respectively. When comparing the given images, it is observed that plasma treatment has increased an effective surface area of the PET substrate by introducing the needle-like micro-irregularities of the surface. The average roughness (R_a) and root mean square roughness (R_q) for the 5 x 5 μm^2 area of PET substrate after the plasma treatment decreased. Together with peak-valley height (Z), the summarised relevant data is given in Table 4.1. The plasma treatment was useful for both cleaning of surface contamination and roughening of the surface, thus ensuring a better adhesion

of the coating. If lateral dimensions of plasma-induced micro-irregularities are much smaller than the wavelength of optical radiation, the roughening of the surface will also serve for the increase of optical transmittance at PET-photopolymer interface.

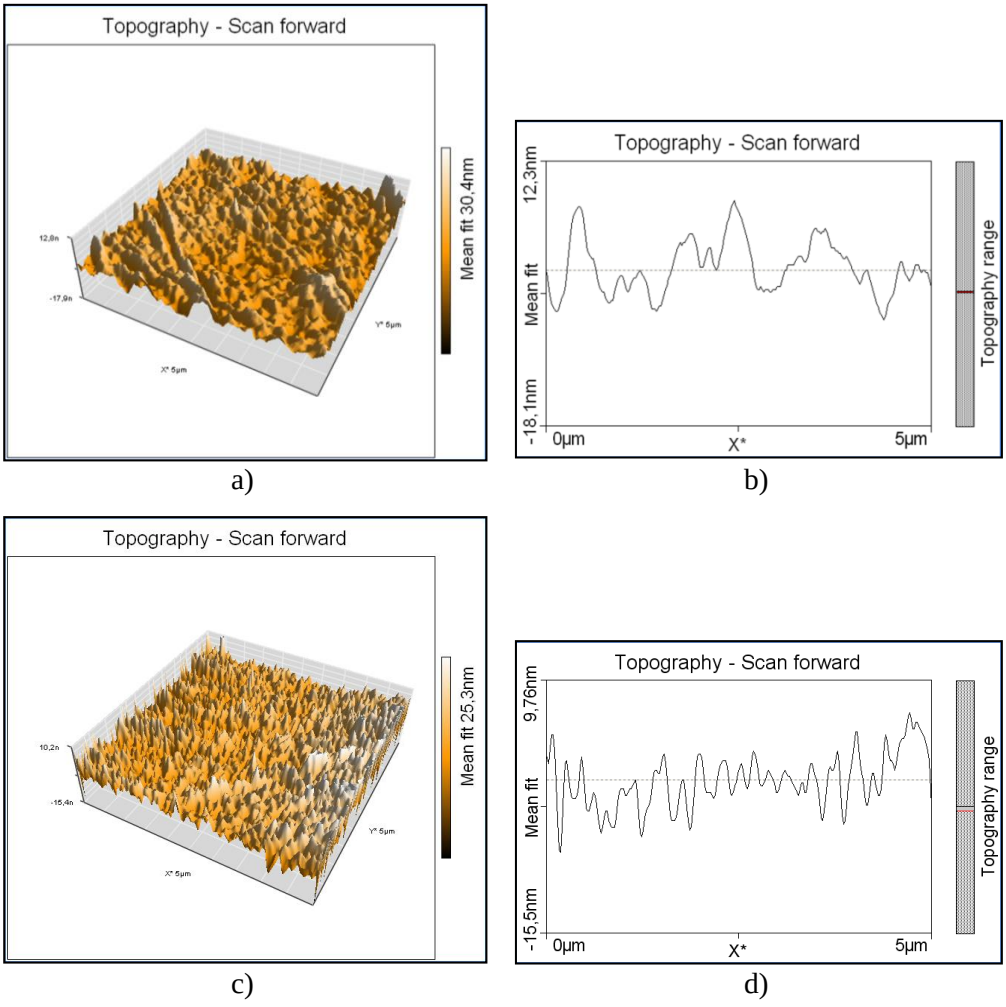

Fig. 4.10. AFM images (a, c – 3D topography; b, d – profile) of PET surface, with no plasma treatment applied (a–b) and treated by O_2 plasma (c–d)

Table 4.1. Values of surface roughness of PET substrate

	Uncleaned by O_2 plasma	**Cleaned by O_2 plasma**
R_a, nm	4.67	2.46
R_q, nm	5.83	3.21
Z, nm	20.21	60.13

The process of UV imprinting was successful and caused no technical problems concerned with contamination of mould or sticking to the polymer. A visual inspection has revealed a high uniformity of the replicated polymeric scales

and the absence of macro-defects. Fig. 4.11 shows the representative AFM image (30×30 μm^2) of polymeric scale in the raster zone. The dimensions in this case are as follows: the period is equal to 21.8 μm, the groove bottom – 9.2 μm, the groove top – 10.6 μm, the hill bottom – 14 μm, and the hill top (ridge) – 12.6 μm. It should be said that Fig. 4.11 is a result of measurements carried out near the internal edge of raster zone, thus the width of the hill exceeds the width of the groove. However, the width of the groove at a half depth matches the width of chromium strips of the photomask very well. The slopes of the replicated grating are steep, although moderate inclines are noticed as a consequence of RIE application to Si wafer. The accuracy of replication was additionally investigated by acquiring a large scale AFM images from 5×5 μm^2 areas at groove bottoms and flat ridges of the raster zone of Si master mould and polymeric gratings. The characteristic AFM images are shown in Fig. 4.12. It can be indicated that the surface morphology of the Si groove bottom almost fully coincides with the one recorded at the polymeric flat ridge (Fig. 4.12a–b). The same tendency is valid for the opposite pair of mutually related surfaces, i.e. Si flat ridge and groove bottom of the polymeric grating (Fig. 4.12c–d). The RIE has caused additional roughening of the groove bottom of Si master mould, which is also transferred to the polymeric scale. It is evident that the quality of replication is high even if the replicated features are small and have lateral dimensions of nanometer order.

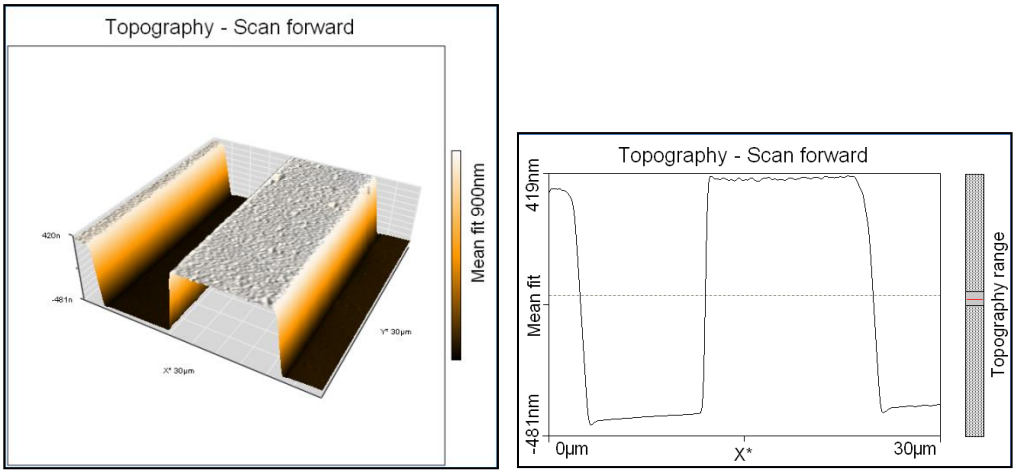

a) b)

Fig. 4.11. AFM image of the surface of polymeric scale: a) 3D topography; b) profile

The main parameters of roughness were calculated for the quantitative evaluation of each surface using the same software. The results obtained for eight different regions of the raster zone were averaged. The values of parameters of roughness which were calculated for 5×5 μm^2 areas of Si master mould and polymeric grating, are presented in Table 4.2. Evidently, the surface roughness of polymeric grating is very similar to that of Si master mould. Roughening induced into silicon during the RIE process evenly declines after UV imprint transfer of surface relief to photopolymer.

All in all, it can be concluded that the surface morphology of the formed polymeric scales is comparable to that of Si imprint mould. Hence, the combination of PET substrate and acrylic photopolymer can be potentially used in high-precision angular positioning systems.

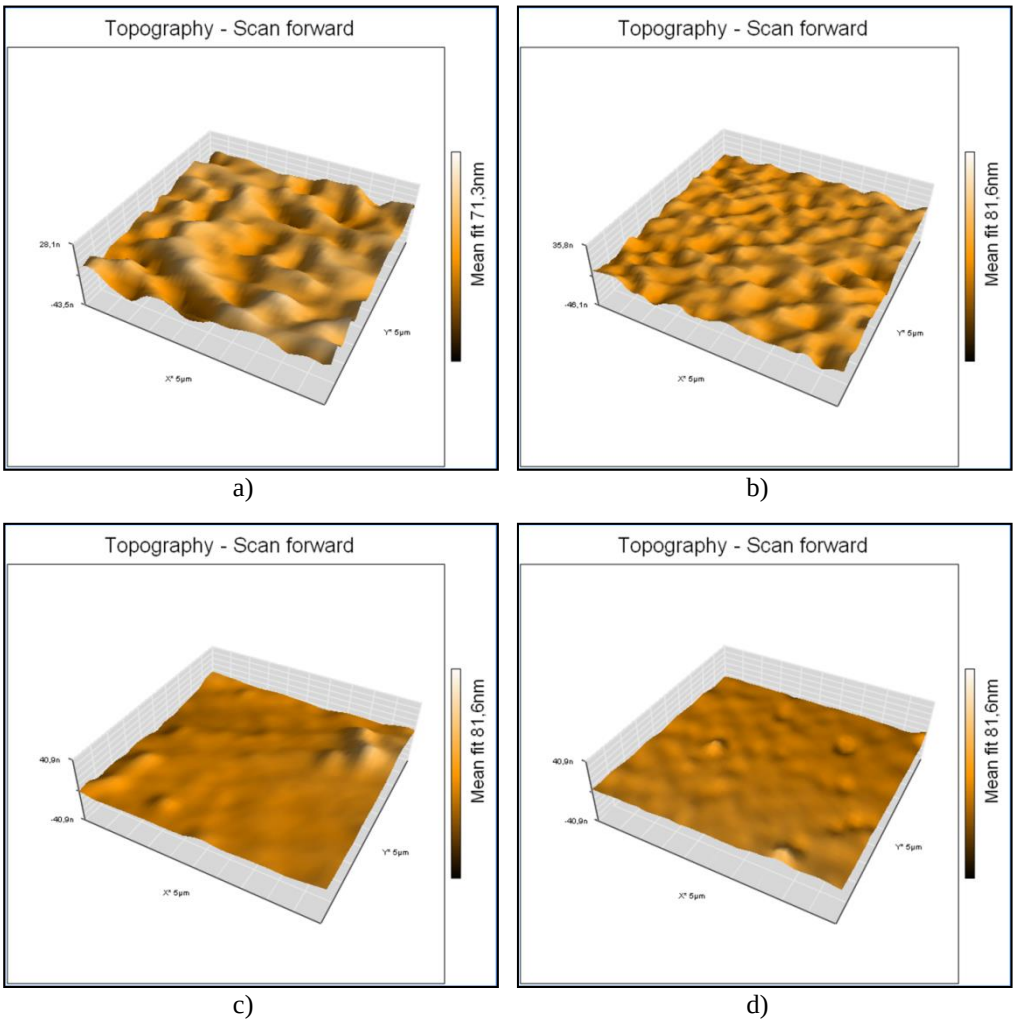

Fig. 4.12. AFM 3D topographic images of Si master mould and the replicated polymeric grating surfaces: a) Si groove bottom; b) polymer flat ridge; c) Si flat ridge; d) polymer groove bottom

Table 4.2. Values of roughness parameters for Si master mould and polymeric grating

	Si master mould		**Polymeric grating**	
	Flat ridge	**Groove bottom**	**Flat ridge**	**Groove bottom**
R_a, nm	2.76	4.67	3.25	2.83
R_q, nm	4.01	5.36	3.91	3.61
Z, nm	31.7	44.1	33.2	24.0

4.2.3. Investigation of optical properties

Optical transmittance

There is a significant need for the fabricated polymeric scales to be characterised by such optical characteristics which would enhance their application possibilities. In particular, optical transmission and reflection are highly important, because they allow one to confirm the proper (or improper) selection of materials composing the scales intended for a potential determination of angular displacement in high-precision positioning systems. Since the mentioned optical properties are mutually related, only the transmission was selected to be analysed in this case, whereas the absorption (and so, the reflection) can be trivially calculated afterwards.

For this reason, the optical properties of thin PET films coated with acrylic photopolymer were initially evaluated by measuring ultraviolet-visible (UV-Vis) transmission. UV-Vis spectroscopy is a measurement of attenuation of a light beam passed through or reflected from a sample surface in the ultraviolet-visible spectral region. The light of the latter and adjacent ranges (near-UV and near-infrared (NIR)) is energetic enough to directly promote the electronic transitions of the sample which are registered by an appropriate device [142]. Since the UV-Vis range spans the domain of human visual acuity of approximately 400–750 nm, this spectroscopy is useful to identify absorption, transmission and reflection of a variety of technologically important materials. The application areas of the latter technique vary from analytical chemistry and life sciences to breakthrough sampling in high-end research of materials and industrial purposes [142].

For this task, a conventional UV-Vis spectrometer was employed. Its operation is based on the measurement of the intensity of light passed through a sample (P) comparing it to the intensity of light before the pass (P_o), when the frequency of radiation is not changed. The ratio (P/P_o) is called the transmittance (T), usually expressed in per cent (%). A modern UV-Vis spectrometer functions according to the subsequent scheme (Fig. 4.13). The device is a single-beam instrument, where the light coming from the UV-Vis source passes the lenses and is dispersed by a monochromator (prism or diffraction grating) before it reaches the sample placed in a cuvette. Then, the rays of light are gathered into one beam by appropriate lenses. The resulting beam is registered by a light detector connected with a read-out device (e.g., a computer).

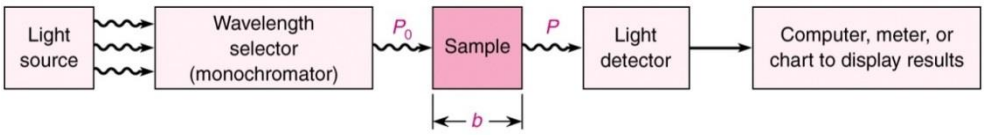

Fig. 4.13. The operation principle of UV-Vis spectrometer

In the analysed case, the transmission measurements were carried out by using a fibre optic UV/VIS/NIR Spectrometer AvaSpec-2048 in the wavelength range from 300 nm to 800 nm, with a resolution of 1.4 nm. The setup of the utilised analytical equipment is provided in Fig. 4.14.

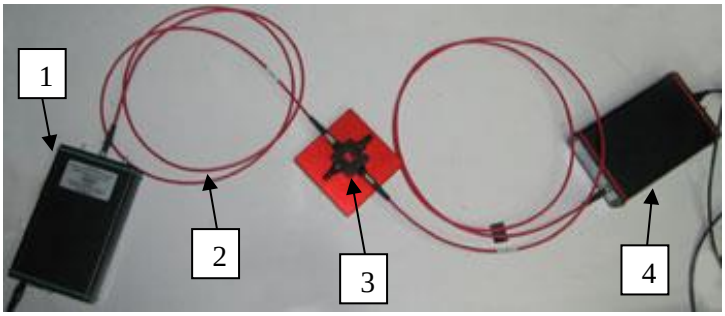

Fig. 4.14. UV/VIS/NIR Spectrometer AvaSpec-2048. Parts: 1 – UV-Vis light source with integrated optics; 2 – fibre optic cable; 3 – cuvette with analysed specimen; 4 – UV-Vis light detector unit with integrated optics and an output to a computer

Optical transmittance of PET and PET covered with a photopolymer layer (3 μm) with respect to the UV-Vis region is presented in Fig. 4.15. It is demonstrated that the influence of photopolymer on the performance of PET in terms of the relevant parameter is relatively negligible, i.e. a decrease in optical transmittance is almost constant and does not exceed 5–6% of the initially registered values throughout the visible light range; the average transmittance value for PET substrate reaches approximately 75%, with the corresponding value for overall polymeric compound being nearly 70%, while the appropriate values almost are very similar in the first half of ultraviolet light range. The numbers show that the applied polymeric substances are a suitable option for the transmission of light as a means for the major purpose stated at the beginning of this section.

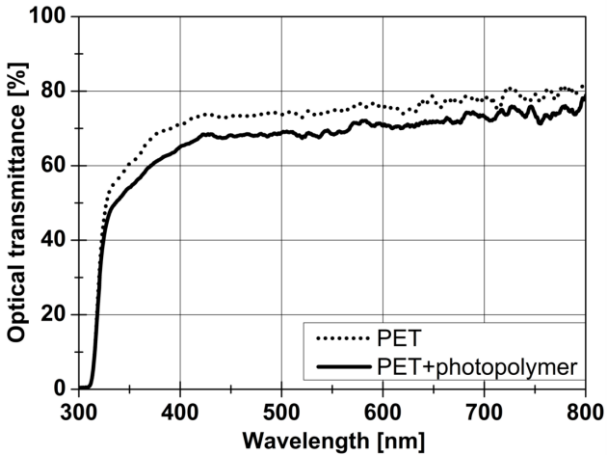

Fig. 4.15. The influence of acrylic photopolymer layer on the optical transmittance of PET film in UV-Vis region

Diffraction intensity

As it was elaborated earlier, interferential rotary encoders could benefit from the proposed polymeric scales. For this purpose, another optical property is substantially desirable. To be more precise, the diffraction intensity of the formed

periodic microstructure plays a crucial role. Optical encoders based on the interferential scanning principle usually employ interference of zero and first-order diffraction beams. The essential components of such sensors are two diffraction gratings: a transparent scanning reticle and reflective step grating. The first grating diffracts an incident light beam at least into the 0 and +/-1 diffraction orders, whereas the second one performs the projection of these orders onto common diffraction directions, where they interfere. Phase shifts between the light beams, which interfere due to the displacement of the first grating relative to the second one, are registered by photodetectors (see Subchapter 1.6 for a more comprehensive explanation). Unwanted beams of diffracted light are spatially filtered. Hence, the diffracted light intensity directly influences the performance of the encoder.

It should be reminded that absolute diffraction efficiency is defined as the ratio between the energy flow (power) of monochromatic light diffracted from the grating (with respect to the maximum order being analysed) and the energy flow (power) of the incident light. Intensity may be a substitute for energy flow in this definition [143]. According to the latter definition, if the value of incident light intensity is constant, diffraction efficiency is directly related to the value of diffracted light intensity; the higher it is, the higher efficiency is observed.

In the executed analysis, the distribution of diffraction intensities in spectrum orders was measured by using a helium-neon (λ = 632.8 nm) laser stand schematically represented in Fig. 4.16. The principle of measurement can be perceived straightforwardly referring to the provided figure.

Measurements of the polymeric scales were carried out at seven points located equidistantly along the angular raster zone for each scale. An example of the transmitted diffraction pattern generated on the dark screen by illuminating the grating of the scale by the laser light is given in Fig. 4.17. It shows an effective diffraction in the form of series of bright spots, with the most of the diffracted light intensity concentrated in the zero and first diffraction orders.

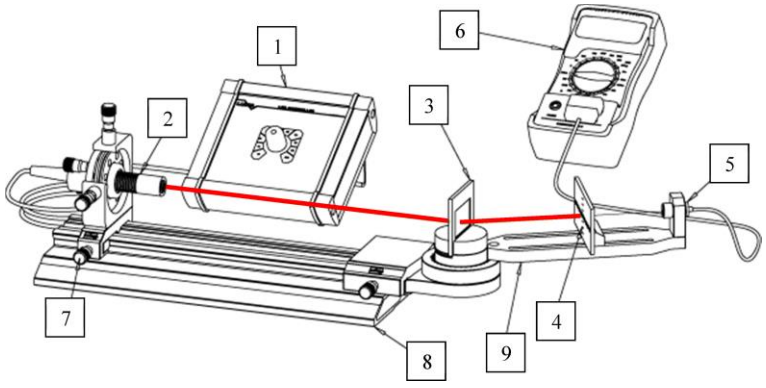

Fig. 4.16. The diffraction intensity measurement stand. Parts: 1 – the power supply; 2 – the He-Ne laser; 3 – a polymeric grating scale; 4 – an optical screen; 5 – a photodetector; 6 – a digital multimetre; 7 – a controller of laser position; 8 – a rail profile of laser position; 9 – a rotational profile unit [144]

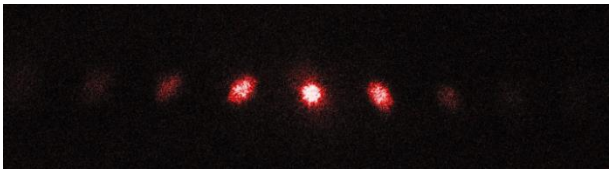

Fig. 4.17. Transmitted diffraction pattern generated due to the interaction of He-Ne laser light with the polymeric scale

Averaged results of both inspected scales for intensity distribution in patterns of the transmitted diffraction are expressed in arbitrary units and presented in Table 4.3. It should be highlighted that the values of diffraction intensity measured at different points of the tested polymeric scales are close to each other, which confirms the uniformity of the UV imprinted polymeric scales over a full area of the raster pattern. Most of the transmitted light is concentrated in the zero and first diffraction orders. Moreover, intensities of the light in the +1 and -1 diffraction orders are not less than 75% of the zero-order beam. Light intensity in the second and higher orders of diffraction pattern is much weaker, and the diffracted beams tend to broaden with increasing diffraction order. Therefore, due to the limited sensitivity of the camera, it is difficult to capture higher orders of diffracted light, and the third order of diffraction is nearly invisible in Fig. 4.17. The values of diffraction intensity measured at different points of the scales deviate not more than 7% and 11% from the corresponding averages (Fig. 4.18) for the 0 and +/-1 order diffraction beams, respectively. Comparative testing of both replicated polymeric scales has shown a sufficient reproducibility of average diffraction intensity patterns, with differences in diffraction intensities not exceeding 5%.

Table 4.3. Intensity distribution in patterns of transmitted diffraction measured at seven points of the polymeric scales

Measurement point	Diffraction order						
	-3	**-2**	**-1**	**0**	**+1**	**+2**	**+3**
1	9	7	290	358	295	8	10
2	11	8	335	384	330	8	11
3	7	12	320	410	307	11	8
4	11	9	347	360	343	8	11
5	10	6	320	370	356	7	11
6	12	5	340	390	358	5	12
7	12	8	325	388	313	8	12

Since the period of the replicated grating of the scale is much larger than the laser wavelength, the intensity distribution of the diffracted light can be described by the scalar grating theory, i.e. the envelope of the diffraction pattern is equal to the diffraction pattern produced by a single grating period. According to the theory, the first minimum of the envelope described by the function sinx/x must occur in the direction of the grating order, a number of which is equal to the ratio of grating period to width of the ridge [145]. In case of this experiment, this ratio is nearly equal to 2, so the results of measurements agree well with the theory despite some deviations of the imprinted pattern from binary phase grating.

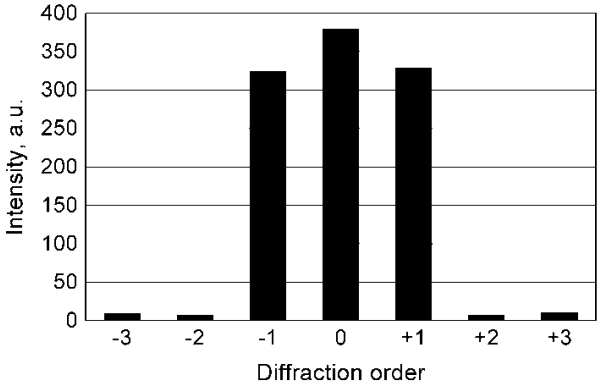

Fig. 4.18. The average values of transmitted diffraction intensity for the tested polymeric scale

Efficient diffraction of the first-order and similar intensities of beams of the zero and first-order diffraction show that the optical properties attributed to the replicated polymeric incremental scales meet the requirements for successful application in optical rotary encoders employing the interferential scanning principle. Proper adjustments of dimensions of the grating (e.g. period, groove depth and profile) can be easily made according to the particular requirements for the configuration of an encoder.

With regards to the data provided in this chapter, a certain modification (version) of polymeric scales would enable them to fulfil the functions of reflective gratings as well. Metallisation of the grating surface is among the main techniques to achieve that. In order to illustrate such possibility, one of the fabricated scales (chosen randomly) was additionally subjected to a coating of ridges of the raster pattern by thin film of aluminium (80 nm) using physical vapour deposition equipment. Al layer is known as one of the most common, cheapest and simple materials to form an optical coating yielding a reflection coefficient of about 88–92% within the visible light spectrum. The obtained results are shown in Fig. 4.19.

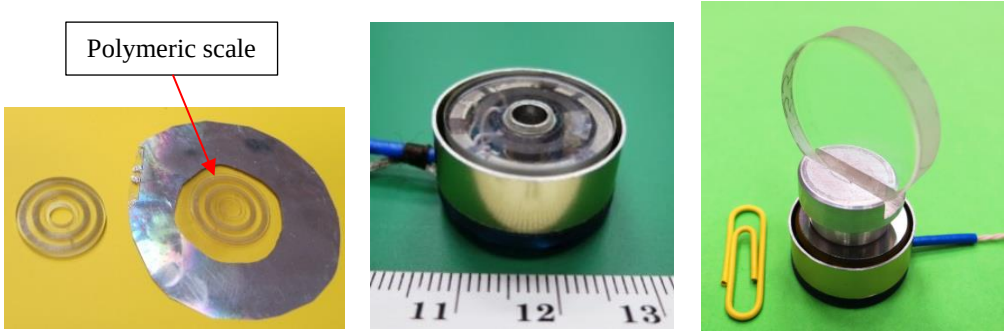

a) b) c)

Fig. 4.19. The application of polymeric incremental scale, with ridges of pattern coated by 80 nm Al layer (a), to organic glass rotor of miniature (22 mm in diameter) piezoelectric rotary stage (b) that might be used for angular positioning of optical element (c)

4.3. Chapter conclusions

In this chapter, a novel polymeric incremental rotary scales meeting the requirements of compactness, high quality and acceptable cost-performance ratio were fabricated and thoroughly characterised. The essential conclusions of this chapter are:

- Two PET-based scales were formed when dividing the fabrication process into two steps: 1) the formation of a silicon master mould by using optical microlithography and reactive ion etching; 2) the formation of an angular raster pattern in a polymeric substrate by using the UV imprint technique.
- Optical microscopy indicated the absence of macro-defects and acceptable reproducibility of Si master mould and polymeric scales with respect to the applied photomask. The same analytical tool demonstrated the appearance of Moiré fringes as one of the ways to detect angular displacement in high-precision positioning systems. The respective Moiré effect was also illustrated by using the MATLAB software.
- Surface morphology analysis with an AFM confirmed the results of optical microscopy in terms of macro-defects and reproducibility. Despite some micro-irregularities observed at the surface of step-profile polymeric microstructure, the elements of raster pattern match the respective counterparts of Si master mould to an adequate extent. The surface roughness of polymeric gratings is comparable to that of Si master mould.
- The investigation of optical transmittance utilising UV-Vis spectrometry revealed that a decrease in optical transmittance of UV-sensitive photopolymer layer in a 300–800 nm range is almost constant and does not exceed 5–6% of values for uncoated PET substrate. UV imprinting causes no problems associated with contamination of Si master mould or sticking to the polymer.
- The measurements of intensity distribution in transmitted diffraction showed that most of the diffracted light intensity is concentrated in the 0 and +/-1 diffraction orders. The values measured at seven different points of the tested polymeric scales do not deviate by more than 7% and 11% from the corresponding averages for the zero and first-order diffraction beams, respectively. The differences in average diffraction intensities between the inspected scales do not exceed 5%.
- The ridges of raster pattern of one polymeric scale were coated by thin film of Al (80 nm), thus indicating the opportunity to make use of optical reflection principle when searching for an acceptable replacement for the conventional glass-chromium scales in high-precision angular positioning systems.

5. THE PROPOSED PROTOTYPE OF A HIGH-RESOLUTION PIEZOELECTRIC ROTARY STAGE

After a thorough investigation of a high-resolution piezoelectric rotary stage from theoretical and experimental points of view discussed in the previous three chapters, decision was made to create a prototype of the rotary piezostage. It would provide a solid background for an overall understanding in terms of design and operation of the device. Considering the constantly growing technical and commercial features-based demands, both the academia and industry could substantially benefit from potential full implementation and realisation of the proposed actuator and/or its modifications. It should be pointed out that the prototype presented in this chapter contains not only the piezoelectric stage, but also the newly designed motion controller with an installed closed-loop control system, thus ensuring precise and accurate motion of the rotor.

In this chapter, the emphasis is mainly placed on the geometric virtual model of the proposed prototype of the piezoelectric rotary stage, with the produced physical prototype of the same device provided in the final step.

5.1. Geometric virtual model of the proposed prototype

The geometric virtual model of the proposed prototype was designed (Fig. 5.1) on the basis of the experimental one presented in Chapter 3, since the dimensions of the components and overall performance of the analysed object were confirmed to be suitable for the intended application. This task was accomplished using Autodesk 3ds Max software in collaboration with company Precizika Metrology.

So as to treat the piezoelectric stage as a complete angular positioning system, a closed-loop control system is a must-have element constantly ensuring a pre-defined required precision and accuracy of positioning, rotor speed, torque, and other dynamic characteristics. Therefore, a programmable motion controller was necessary to design. A geometric virtual model of the proposed prototype of the controller is given in Fig. 5.2. At the back of the device, there is a DC output for energy supply, a USB 2.0 port for exporting the measurement data, an RS232 IN port for setting parameters and programming with a computer, and an RS232 OUT port for observation of measurement results and related technical characteristics on the computer screen.

a) 

b) 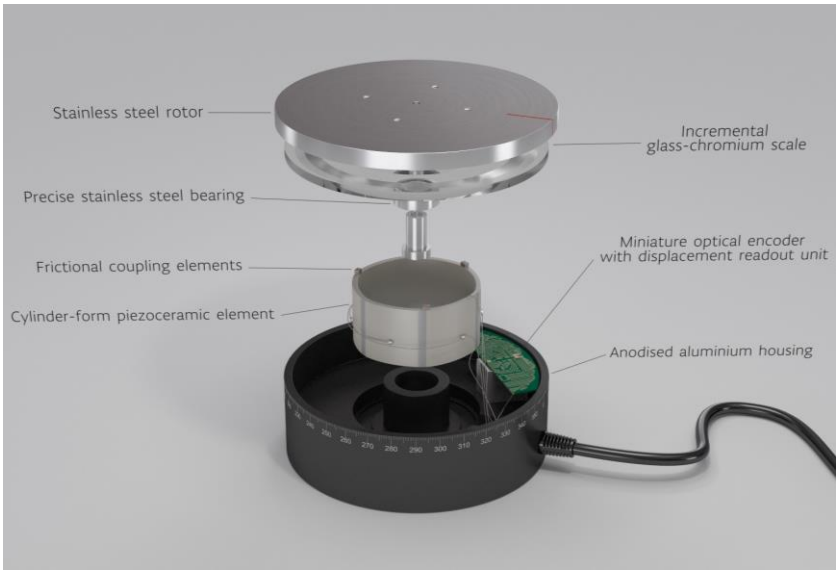

Fig. 5.1. A geometric virtual model of the proposed prototype of a piezoelectric stage: a) the overall (isometric) view with indicated dimensions; b) an exploded view with denoted major parts

A combination of the piezostage and a motion controller resulted in the generation of prototype of high-resolution piezoelectric rotary stage (Fig. 5.3a). The controller is activated/deactivated by an "On/Off" button. The "Menu/Set" button enables one both to enter the menu list containing all parameters which can be adjusted and select a feature needed to be changed. Browsing through the list and increasing/decreasing the value of the parameter of interest is performed by the "+" and "-" buttons. In order to initiate or terminate the angular displacement of the rotor, the button "Start/Stop" is employed. The "Reset" option provides a possibility for the rotor to drive back to the initial position at 0 degrees.

a) 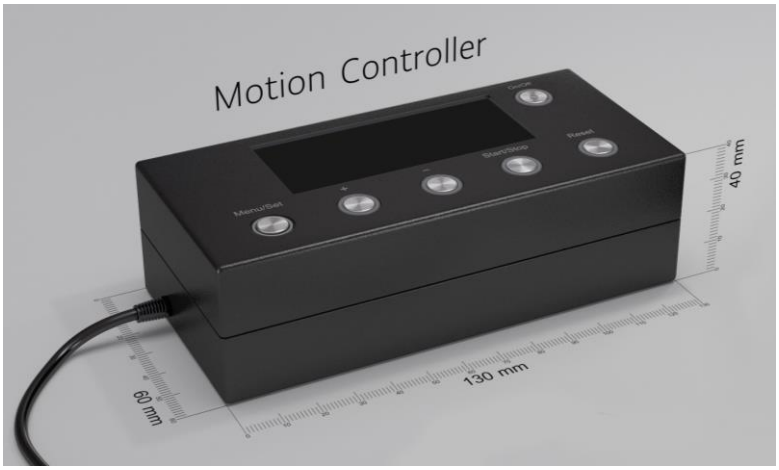

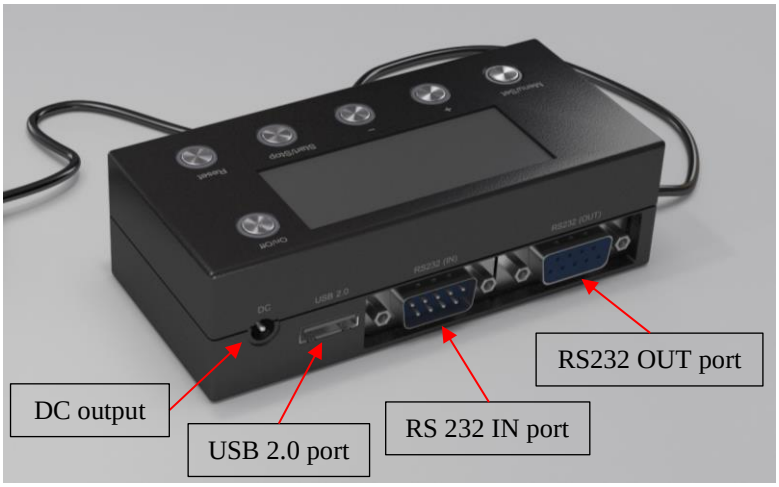

b)

Fig. 5.2. A geometric virtual model of the proposed prototype of a motion controller: a) an overall (isometric) front view with indicated dimensions; b) an overall (isometric) back view

The positioning of optical elements stands among the most prevalent application fields of the device (Fig. 5.3b). In the given example, an LCD display shows five main operational parameters utilised to adjust and set the operation of the piezoelectric rotary stage properly. They encompass “Angular displacement: 30 [^{o}]”, “Weight load: 0 [g]”, “Angular speed: 360 [^{o}/s]”, “Excitation voltage: 60 [V]”, and “Excitation frequency: 126.26 [kHz]”.

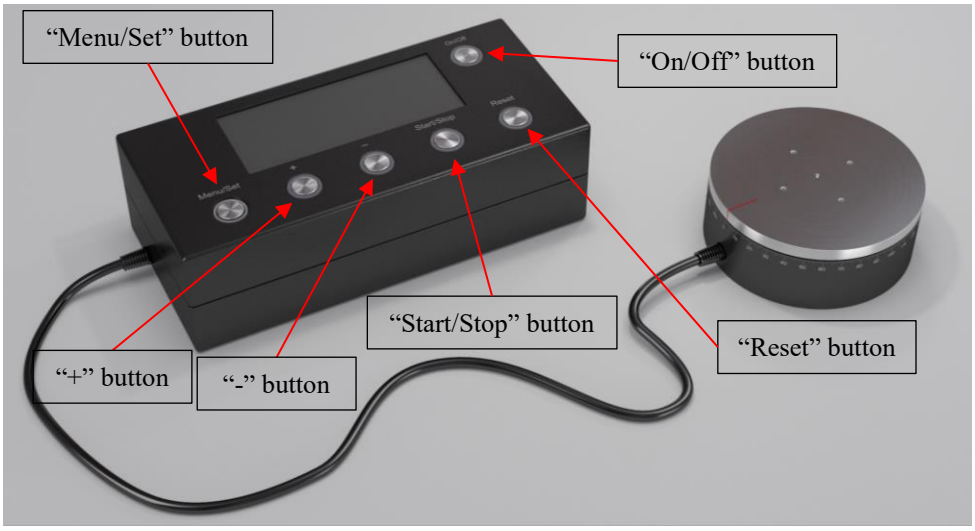

a)

b)

Fig. 5.3. A geometric virtual model of the proposed prototype of high-resolution piezoelectric rotary stage: a) an overall view; b) the stage in action (positioning of optical element)

Considering the fact that the investigated piezoelectric stage (see Chapter 2 and Chapter 3) is rather compact in size, simple in structure and characterised by a well-defined performance, the decision was made not only to combine it with the motion controller, as shown above, but also to propose a range of actuators identical in the operation principle, but different in dimensions and dynamic characteristics (Fig. 5.4). The mentioned range could be attractive to both the academia and industry due to wide possibilities of application.

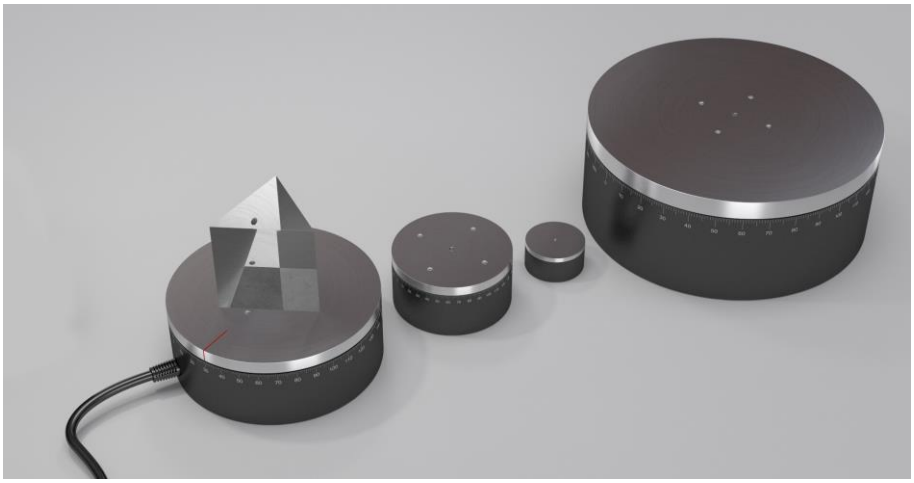

Fig. 5.4. Geometric virtual models of the proposed prototypes of several modifications of the high-resolution piezoelectric rotary stage

5.2. Produced physical prototype

As it was already mentioned, a system of motion control is indispensable to any high-precision angular positioning system, including piezoelectric rotary stages, when aiming for high-quality motion. Usually, the structure and operation principle of the piezoelectric rotary motors and drives cause a presence of specific shortcomings (neglecting those mentioned in the first chapter); these, for instance, are time-varying tribological parameters of friction pairs or irregularity of instantaneous motion velocity and dependence of the velocity on the rotational direction. The latter issues highly influence the dynamic parameters and performance of piezoelectric motors and drives.

Considering both of the mentioned aspects and the requirement of high-resolution motion for the designed piezoelectric rotary stage, it was decided to develop and adapt an integrated closed-loop feedback control system with a separate motion control unit at the final part of this work; this was achieved in collaboration with the scientists from the faculty of electronics and electrical engineering at KTU. The created system enables to decrease the displacement errors to a significant extent. The produced physical prototype acting as a relatively simplified version of the geometric virtual model presented in Subchapter 5.1 is given in Fig. 5.5. In this version, the desired angular displacement is set by using an external programming device (e.g. a computer), with the autonomous control to be realised in the nearest future, thus enabling a user to control the piezoelectric rotary stage in a completely wireless mode. A simplified structural control scheme of the device is provided in Fig. 5.6. In this scheme, *PK driver* denotes the piezostage, and *mark disk* denotes a glass-chromium incremental scale attached to the rotor; together with the optical encoder, these structural components comprise the complete rotary stage. As the scheme is rather trivial, it will not be explained in details here.

Fig. 5.5. The physical prototype of a high-resolution piezoelectric rotary stage with an integrated closed-loop feedback control system

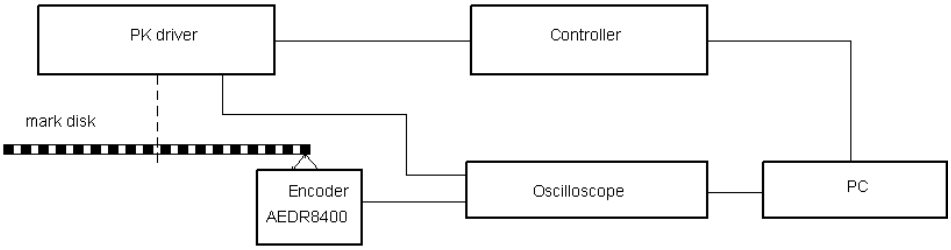

Fig. 5.6. A simplified structural control scheme of the high-resolution piezoelectric rotary stage

Fig. 5.7 shows a structural scheme of the programmable logical controller (PLC) acting as the main component in the setup. The operation of the PLC is controlled by a universal CPU microprocessor Atmega 8. The angular position of the rotor is registered by an optical reflective encoder AEDR-8400 interacting with the incremental scale that contains 2500 rasters. The encoder outputs two quadrature signals to the CPU for further processing and identification of the position. By a short press of buttons *SW1* or *SW2*, the piezoelectric stage is rotated and stopped at the desired angular position in clockwise or counter-clockwise direction of motion.

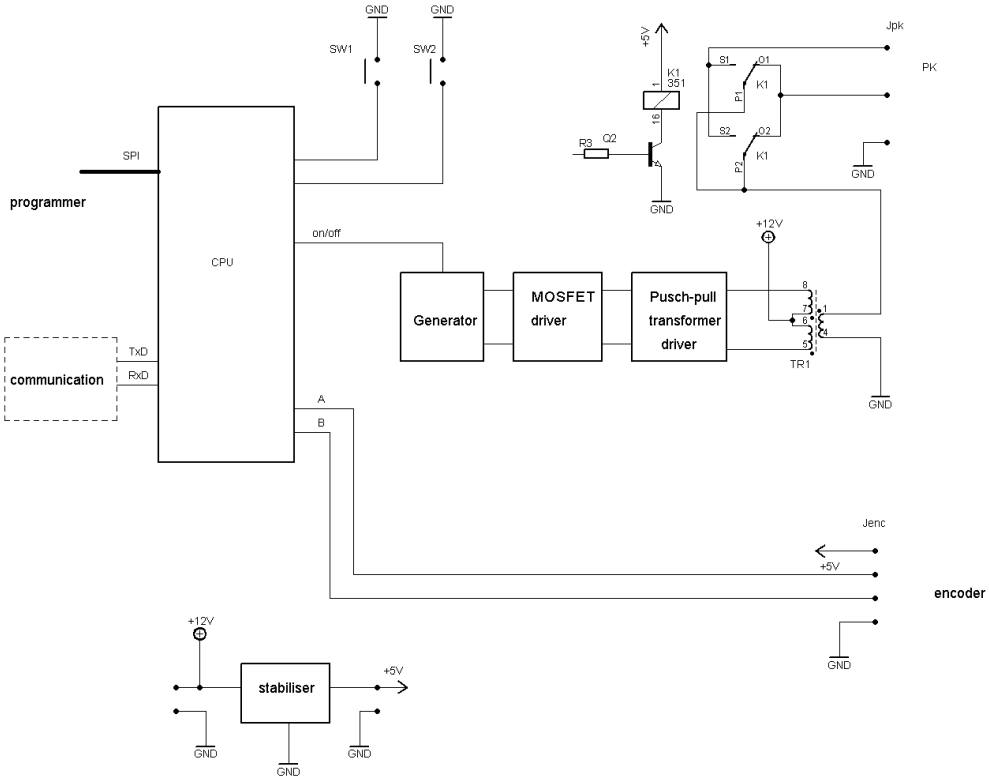

Fig. 5.7. A structural scheme of programmable logical controller used to control the operation of the high-resolution piezoelectric rotary stage

Initially, the piezocylinder is excited by a DDS-type signal generator AD9832. The generated signal is received by the MOSFET transistor ensuring a quick operation and moderate allowable heating of the switch-type transistors. The signal of the required amplitude is formed at the output (secondary) coil of the transformer (*TR1*). The relay-type switch receives the signal and passes it to one of the electrode groups (depending on the necessary rotation direction) of the piezocylinder. A driving voltage of 9 V_{dc} is supplied to the PLC; a higher voltage may lead to overheating of the piezocylinder.

The main performance characteristics of the designed high-resolution piezoelectric rotary stage are summarised in Table 5.1.

Table 5.1. The main performance characteristics of the designed high-resolution piezoelectric rotary stage

Dimensions	Ø66 x 25 mm
Weight	150 g
Active axis	θ_Z
Rotation range	$>360^o$
Motion direction	bidirectional
Resolution	0.254 μrad
Sensor	Optical incremental encoder
Max. angular speed (load-free)	60 rpm (6.28 rad/s)
Drive torque	5.6 mNm
Max. external load capacity	2 kg
Motor type	Resonant ultrasonic
Material	Anodised aluminium and stainless steel

5.3. Chapter conclusions

According to the obtained results, the following conclusions have been drawn:

- A geometric virtual model of the proposed prototype of the high-resolution piezoelectric rotary stage with a closed-loop feedback control system was developed. The respective models of several modifications of the piezostage, which are identical in the operation principle but different in dimensions and dynamic characteristics, were created as well.
- A relatively simplified physical version of the developed geometric virtual model of the high-resolution piezoelectric rotary stage was produced and presented. In terms of the main performance characteristics, the piezostage is comparable (or more competitive) to analogous devices on the market and superior with respect to cost-effectiveness.

CONCLUSIONS

1. A comprehensive literature review of the existing high-precision rotary stages revealed that piezoelectric resonant USMs have a huge potential to be widely applied as driving elements in high-resolution rotary stages and positioners; however the main limiting issues are insufficient precision, complex structure, and relatively high manufacturing costs. It was also identified that polymeric incremental scales can offer a more favourable cost-performance ratio than the conventional glass-chromium incremental scales, and they can be used to measure precise angular displacements of rotary stages.
2. Theoretical investigation of the designed high-resolution piezoelectric rotary stage driven by resonant ultrasonic standing-waves was carried out. It was disclosed that:
   i) The operational frequency interval of the piezocylinder is 125.8–132 kHz in the presence of driving voltage of 20–80 V. Elliptical motion trajectories of the contact zones in the axial-tangential plane form well-defined rotational motion of the rotor.
   ii) Lumped-parameter analytical model of vibro-impact interaction dynamics between the piezocylinder and rotor showed that the recommended operational frequency of the piezocylinder should be equal to or span in the vicinity of resonant frequency, and a there should be a small gap between the rotor and the contact zone element in the normal direction during the rotor motion. The model can be easily adapted to various piezoelectric rotary and linear motors utilising friction-based contact between input and output links.
   iii) A numerical transient study of the piezocylinder interaction with the rotor under varying external loading (0–2 kg) conditions revealed that the time needed for the actual rotor motion to start is inversely and non-linearly dependent on the applied external load.
3. The results of experimental investigation of the designed piezoelectric rotary stage in terms of the main dynamic characteristics indicated that:
   i) The operational resonant frequency of 126.26 kHz induces tangential and axial displacements of the top surface of the piezocylinder, thus generating elliptical motion trajectories of the contact zone elements in the clockwise and counter-clockwise directions. The highest displacement amplitudes are registered in the tangential direction, so the respective oscillations are the driving ones in the entire range of applied voltage amplitudes (20–80 V).
   ii) The assessment of surface displacement of the piezocylinder by holographic interferometry confirms the suitability of the selected topology of electrodes and the excitation for a uniform displacement of the top and side surfaces.
   iii) The values of average resolution of the developed piezoelectric rotary stage are 0.250 μrad (clockwise motion) and 0.258 μrad (opposite motion), which make the device superior to most of competitive products on the market. The dependence of resolution on the applied external load (0–2 kg) is non-linear, with the maximal resolution observed at 0.25 kg; a further increase in the load until the maximum results in a decrease of resolution by about 11 times.

iv) The influence of driving voltage (20–80 V) on the angular speed (28–66 rpm) of the rotor under the effect of varying external load (0–2 kg) is defined by a non-linear tendency for the speed to rise, when the supplied voltage increases. It is demonstrated that the torque of the rotor non-linearly increases with the increase in the driving voltage. A rise of the applied torque load imposes a non-linear decrease in the angular speed of the rotor under constant driving voltage.

v) Dynamic operation mode characterised by the generation of torsional oscillations concomitant with rotational motion of the rotor was exhibited. The novel mode is featured by slow bidirectional scanning-type motion of the rotor, thus very preferable in high-precision positioning systems.

4. Two polymeric (PET-based) incremental scales were fabricated combining optical microlithography and UV-nanoimprint techniques in order to possibly measure the angular displacement of the rotor of piezoelectric rotary stage. It was found that the surface roughness of the polymeric raster pattern is comparable to that of Si master mould. The decrease in optical transmittance of the scales in the 300–800 nm range is almost constant and does not exceed 5–6% of values for the photopolymer-uncoated PET substrate. Most of the diffracted light intensity of the scales is concentrated in the 0 and +/-1 diffraction orders. The differences in average diffraction intensities between the inspected scales do not exceed 5%.
5. Geometric virtual model of the high-resolution piezoelectric rotary stage with a closed-loop feedback control system was developed, followed by a relatively simplified physical version produced afterwards. In terms of the main performance characteristics, this device is comparable (or more competitive) to analogous devices on the market and superior with respect to its cost-effectiveness. The proposed design of the piezoelectric stage is in the process of transfer into viable industrial product to be commercialised by the company Precizika Metrology.

REFERENCES

1. BAURIENĖ, G., KULVIETIS, G., GRIGORAVIČIUS, A. Optimization of fixation elements parameters for ring type piezoelectric actuator generating elliptical movement. *Mechanics*. 2014, 20(3), 294-298. doi: 10.5755/j01.mech.20.3.7388
2. LU, X., HU, J., YANG, L., ZHAO, C. A novel dual stator-ring rotary ultrasonic motor. *Sensors and Actuators A: Physical*. 2013, 189, 504-511. doi: 10.1016/j.sna.2012.11.009
3. YANG, X., LIU, Y., CHEN, W., LIU, J. A cylindrical traveling wave ultrasonic motor using bonded-type composite beam. *Ultrasonics*. 2016, 65, 277-281. doi: 10.1016/j.ultras.2015.09.014
4. LIU, Y., CHEN, W., FENG, P., LIU, J. A square-type rotary ultrasonic motor with four driving feet. *Sensors and Actuators A: Physical*. 2012, 180, 113-19. doi: 10.1016/j.sna.2012.04.024
5. SMITH, G.L., RUDY, R.Q., POLCAWICH, R.G., DEVOE, D.L. Integrated thin-film piezoelectric traveling wave ultrasonic motors. *Sensors and Actuators A: Physical*. 2012, 188, 305-311. doi: 10.1016/j.sna.2011.12.029
6. LAN, C-C., WANG, J-H., FAN, C-H. Optimal design of rotary manipulators using shape memory alloy wire actuated flexures. *Sensors and Actuators A: Physical*. 2009, 153(2), 258-266. doi: 10.1016/j.sna.2009.05.019
7. ZHENG, J., SALTON, A., FU, M. Design and control of a rotary dual-stage actuator positioning system. *Mechatronics*. 2011, 21(6), 1003-1012. doi: 10.1016/j.mechatronics.2011.03.011
8. ZHAO, C. *Ultrasonic motors: technologies and applications*. Beijing: Science Press, 2015.
9. SLOCUM, H. A. *Precision machine design*. USA: Prentice-Hall, 1992.
10. Newport | *Motion basics and standards* [interactive]. [Last viewed 2016 12 01]. Access via internet: https://www.newport.com/n/motion-basics-and-standards
11. BURRIS, M. *Stepper motors vs servo motors - selecting a motor* [interactive]. 2016. [Last viewed 2016 12 01]. Access via internet: https://www.lifewire.com/stepper-motor-vs-servo-motors-selecting-a-motor-818841
12. Advanced Micro Controls Inc. | *Stepper vs. servo* [interactive]. [Last viewed 2016 12 01]. Access via internet: http://www.amci.com/tutorials/tutorials-stepper-vs-servo.asp
13. Newport | *Stage components considerations* [interactive]. [Last viewed 2016 12 02]. Access via internet: https://www.newport.com/n/stage-components-considerations
14. SCHELLENEKENS, P. et al. Design for precision: current status and trends. *CIRP Annals – Manufacturing Technology*. 1998, 47(2), 557-586. doi: 10.1016/S0007-8506(07)63243-0
15. Catalogue of Camille Bauer | *Angular position engineering at a glance* [interactive]. [Last viewed 2016 12 02]. Access via internet: http://www.camillebauer.com/src/download/DM-1022-000-01-EN-05.11.pdf

16. Parker | *Linear and rotary positioning stages* [interactive]. [Last viewed 2016 12 02]. Access via internet: http://www.parkermotion.com/engineeringcorner/linearmechanics.html
17. Aerotech | *Rotary stages* [interactive]. [Last viewed 2016 12 03]. Access via internet: http://www.aerotech.com/product-catalog/stages/rotary-stage.aspx
18. Newport | *Motorized rotation stage* [interactive]. [Last viewed 2016 12 03]. Access via internet: https://www.newport.com/c/motorized-rotation-stages
19. Throlabs | *Motorized rotation stages and mounts* [interactive]. [Last viewed 2016 12 03]. Access via internet: http://www.thorlabs.com/navigation.cfm?guide_id=2175
20. Newmark Systems | *Rotary positioners* [interactive]. [Last viewed 2016 12 03]. Access via internet: http://www.newmarksystems.com/rotary-positioners/
21. Dynamic Solutions | Rotary stages [interactive]. [Last viewed 2016 12 03]. Access via internet: http://www.dynamicsolutionsusa.com/product/mechanical-components/rotary-stages
22. Dover Motion | *Rotary tables* [interactive]. [Last viewed 2016 12 03]. Access via internet: http://www.dovermotion.com/SpecificProductFamily_Rotary_Tables
23. HUGHES, A., DRURY, B. *Electric motors and drives: fundamentals, types and applications*. 4th ed. UK: Elsevier, 2013.
24. KRISHNAN, R. *Electric motor drives: modeling, analysis, and control*. USA: Prentice Hall, 2001.
25. LU M-S. A review of high-efficiency motors: specification, policy, and technology. *Renewable and Sustainable Energy Reviews*. 2016, 59, 1-12. doi: 10.1016/j.rser.2015.12.360.
26. PENG, Y., PENG, Y., GU, X., WANG, J., YU, H. A review of long range piezoelectric motors using frequency leveraged method. *Sensors and Actuators A: Physical*. 2015, 235(1), 240-255. doi: 10.1016/j.sna.2015.10.015
27. KING, G. T, PRESTON, E. M., MURPHY, M. J. B, CANNELL, S. D. Piezoelectric ceramic actuators: a review of machinery applications. *Precision Engineering*. 1990, 12(3), 131-136. doi: 10.1016/0141-6359(90)90084-C.
28. RU, C., LIU, X., SUN, Y. *Nanopositioning technologies – fundamentals and applications*. Switzerland: Springer, 2016.
29. Cedrat technologies | *Piezopositioner OPP120SM* [interactive]. [Last viewed 2016 12 04]. Access via internet: http://www.cedrat-technologies.com/en/mechatronic-products/actuators/mechanisms.html
30. Piezomotor | *Piezo LEGS WavePlate* [interactive]. [Last viewed 2016 12 04]. Access via internet: http://www.piezomotor.com/app/static/cat/2014/index.html#/66
31. Attocube | *Nanoprecise stepper rotator ECR5050* [interactive]. [Last viewed 2016 12 04]. Access via internet: http://www.attocube.com/attomotion/industrial-line/ecr5050/
32. SmarAct | *High precision rotary positioner SR5714* [interactive]. [Last viewed 2016 12 04]. Access via internet: http://www.smaract.com/products/rotary-positioners/sr-5714

33. PI | *Q-632 Q-Motion rotation stage* [interactive]. [Last viewed 2016 12 04]. Access via internet: https://www.physikinstrumente.com/en/products/rotation-stages/stages-with-piezomotor/q-632-q-motion-rotation-stage-111229/
34. Nanomotion | *FBR060 rotary stage* [interactive]. [Last viewed 2016 12 04]. Access via internet: http://www.nanomotion.com/motion-product/fbr060-rotary-stage/
35. PI | *U-628 PILine rotation stage* [interactive]. [Last viewed 2016 12 04]. Access via internet: https://www.physikinstrumente.com/en/products/rotation-stages/stages-with-piezomotor/u-628-piline-rotation-stage-703060/
36. SPANNER, K., KOC, B. Piezoelectric motors, an overview. *Actuators*. 2016, 5(1):6, 3-18. doi: 10.3390/act5010006
37. SmarAct | *Applications* [interactive]. [Last viewed 2016 12 04]. Access via internet: http://www.smaract.com/applications
38. Leica | Total stations [interactive]. [Last viewed 2016 12 04]. Access via internet: http://leica-geosystems.com/products/total-stations
39. LI, J. et al. A piezoelectric-driven rotary actuator by means of inchworm motion. *Sensors and Actuators A: Physical*. 2013, 194, 269-276. doi: 10.1016/j.sna.2013.02.020
40. Piezoelectric electromechanical translation apparatus. Inventor: JR MAY, G. WILLIAM. US patent US 3902084 A. 1975-08-26. [Last viewed 2016 12 05]. Access via internet: https://www.google.com/patents/US3902084
41. KIM, C. S., KIM, H. S. Precise rotary motor by inchworm motion using dual wrap belts. *Review of Scientific Instruments*. 1999, 70(5), 2546-2550. doi: 10.1063/1.1149789
42. HU, C. et al. Rotatory stepping piezoelectric motor with micro-angle. In *Proceedings of the 9th International Conference on Electronic Measurement & Instruments (ICEMI).* Curran Associates, Inc., 2009. pp. 545-549.
43. OHNISHI, K., UMKEDA, M., KUROSAWA, M., UEHA, S. Rotary inchworm-type piezoelectric actuator. *Electrical Engineering in Japan*. 1990, 110(3), 107-114. doi: 10.1002/eej.4391100310
44. ZHOU, M., RUAN, Y., LIU. W., HUANG. S., FU, X. A bio-inspired piezoelectric motor with simple structured asymmetric stator. *Smart Materials and Structures*. 2014, 23(4), 1-9. doi: 10.1088/0964-1726/23/4/045003
45. FURUTANI, K., FURUICHI, M., MOHRI, N. Coarse motion of 'seal mechanism' with three degrees of freedom by using difference of frictional force. *Measurement Science and Technology*. 2001, 12(12), 2147-2153. doi: 10.1088/0957-0233/12/12/316
46. FURUTANI, K., OHTA, N. Positioning performance of L-shaped seal mechanism with 3 degrees of freedom. *Proceedings of IEEE International Conference on Robotics and Automation*. IEEE Xplore, 2002. pp. 3660-3665.
47. FURUTANI, K., OHTA, N., KAWAGOE, K. Coarse and fine positioning performance of an L-shaped seal mechanism with three degrees of freedom. *Measurement Science and Technology*. 2003, 15(1), 103-111. doi: 10.1088/0957-0233/15/1/014

48. SZUFNAROWSKI, F. *Dynamic modeling and bioinspired control of a walking piezoelectric motor*. *PhD Thesis* [interactive]. 2013. [Last viewed 2016 12 09]. Access via internet: https://www.techfak.uni-bielefeld.de/~fszufnar/publications/phd_thesis_web.pdf
49. ZHAKYPOV, Z., GOLUBOVIC, E., UZUNOVIC, T., SABANOVIC, A. High precision control of a walking piezoelectric motor in bending mode. *Proceedings of the 9th Asian Control Conference (ASCC).* IEEE Xplore, 2013.
50. Position control device. Inventor: BRISBANE, D.A. US patent US 3377489A. 1968-04-09. [Last viewed 2016 12 05]. Access via internet: https://www.google.com/patents/US3377489
51. Device for precision displacement of a dolid body. Inventors: GALUTVA, V.G., RYAZANTSEV, I. A., PRESNYAKOV, S. G., MODESTOV, K.J. US patent US 3684904A. 1972-08-15. [Last viewed 2016 12 05]. Access via internet: http://www.google.tl/patents/US3684904
52. Bimorphous element adjustment drive. Inventors: MARTH, H., GLOES, R. DE patent DE 4408618 A1. 1995-09-21. [Last viewed 2016 12 05]. Access via internet: http://www.google.je/patents/DE4408618A1?cl=en
53. Fine walking actuator. Inventors: JOHANSSON, S., BEXELL, M., LITHELL, O.P. US patent US 6337532 B1. 2002-01-08. [Last viewed 2016 12 05]. Access via internet: https://www.google.com/patents/US6337532
54. ZHANG, M. Z., AN, Q., LI, W. J., ZHANG, J. W. Piezoelectric friction-inertia actuator – a critical review and future perspective. *International Journal of Advanced Manufacturing Technologies*. 2012, 62, 669-685. doi: 10.1007/s00170-011-3827-z
55. BREGUET, M. J., DRIESEN, W., KAEGI F., CIMPRICH, T. Applications of piezo-actuated micro-robots in micro-biology and material science. *Proceedings of International Conference on Mechatronics and Automation*. IEEE Xplore, 2007. pp. 1-8.
56. GAO, W., SATO, S., ARAI, Y. A linear-rotary stage for precision positioning. *Precision Engineering*. 2010, 34(2), 301-306. doi: 10.1016/j.precisioneng.2009.07.003
57. MORITA, T. et al. A smooth impact rotation motor using a multi-layered torsional piezoelectric actuator. *IEEE Transactions on Ultrasonics, Ferroelectrics and Frequency Control*. 1999, 46(6), 1439-1445. doi: 10.1109/58.80886
58. BERGANDER, A. et al. Monolithic piezoelectric push-pull actuators for inertial drive. *Proceedings of International Symposium on Micro-NanoMechatronics and Human Science*. IEEE Xplore, 2003. pp. 309-316.
59. WANG, C. Y., CHANG, H. S. Design and performance of a piezoelectric actuated precise rotary positioner. *Review of Scientific Instruments*. 2006, 77(105101), 1-5. doi: 10.1063/1.2336760
60. ZHANG, Q., CHENG, L. P., TING, Y. M., RANG, F. K., HUA, Z. F. Piezoelectric rotary motor based on active bulk torsional element with grooved helical electrodes. *IEEE/ASME Transactions on Mechatronics*. 2012, 17(2), 260-268. doi: 10.1109/TMECH.2010.2099129

61. PENG, Y., ITO, S., SAKURAI, Y., SHIMIZU, Y., GAO, W. Construction and verification of a linear-rotary microstage with a millimeter-scale range. *International Journal of Precision Engineering and Manufacturing*. 2013, 14(9), 1623-1628. doi: 10.1007/s12541-013-0219-3
62. CHEN, K., WEN, J., CHENG, G., MA, J., ZENG, P. An asymmetrical inertial piezoelectric rotary actuator with the bias unit. *Sensors and Actuators A: Physical*. 2016, 251, 179-187. doi: 10.1016/j.sna.2016.10.004
63. BUECHI, R. et al. Inertial drives for micro- and nano-robots: two novel mechanisms. *SPIE Proceedings*. 1995, 2593, 80-88. doi: 10.1117/12.228638
64. CHENG, G., HU, Y., WEN, J., ZENG, P., XING, C. Piezoelectric inertial rotary actuators based on asymmetrically clamping structures. *Sensors and Actuators A: Physical*. 2015, 223, 125-133. doi: 10.1016/j.sna.2015.01.007
65. VAN DE WULP, H. et al. Compact, piezo-driven, vacuum compatible rotation device. *Review of Scientific Instruments*. 1995, 66(11), 5339-5342. doi: 10.1063/1.1146109
66. SHIM, Y. J., GWEON, G. D. Piezo-driven metrological multiaxis nanopositioner. *Review of Scientific Instruments*. 2001, 72(11), 4183-4187. doi: 10.1063/1.1408932
67. ZHANG, H. et al. Impact drive rotary precision actuator with piezolectric bimorphs. *Frontiers of Mechanical Engineering in China*. 2008, 3(1), 71-75. doi: 10.1007/s11465-008-0008-3
68. Piezoelectric adjusting element. Inventor: WISCHNEVSKIY, W. US patent US 6765335 B2. 2002-06-12. [Last viewed 2016 12 05]. Access via internet: https://www.google.com/patents/US6765335
69. PI | *Operating principle of PILine* [interactive]. [Last viewed 2016 12 04]. Access via internet: https://www.physikinstrumente.com/en/technology/piezoelectric-drives/piline-ultrasonic-motors/
70. RAGULSKIS, K., BANSEVICIUS, R., BARAUSKAS, R., KULVIETIS, G. *Vibromotors for precision microrobots*. USA: Hemisphere Publishing Corp, 1988.
71. HE, S., CHIAROT, R. P., PARK, S. A single vibration mode tubular piezoelectric ultrasonic motor. *IEEE Transactions on Ultrasonics, Ferroelectrics, and Frequency Control*. 2011, 58(5), 1049-1061. doi: 10.1109/TUFFC.2011.1905
72. PAN, L.C, MA, T. Y., LIU, B. Y., ZHANG, Q., FENG, H. Z. Torsional displacement of piezoelectric fiber actuators with helical electrodes. *Sensors and Actuators A: Physical*. 2008, 148, 250-258. doi: 10.1016/j.sna.2008.08.002
73. KUROSAWA, M., NAKAMURA, K., OKAMOTO, T., UEHA, S. An ultrasonic motor using bending vibrations of a short cylinder. *IEEE Transactions on Ultrasonics, Ferroelectrics, and Frequency Control*. 1989, 36(5), 517-521. doi: 10.1109/58.31795
74. KOC, B., CAGATAY, S., UCHINO, K. A Piezoelectric motor using two orthogonal bending modes of a hollow cylinder. *IEEE Transactions on*

Ultrasonics, Ferroelectrics, and Frequency Control. 2002, 49(4), 495-500. doi: 10.1109/58.996568
75. LIU, Y., CHEN, W., FENG, P., LIU, J. A rotary piezoelectric motor using bending vibrators. *Sensors and Actuators A: Physical*. 2013, 196, 48-54. doi: 10.1016/j.sna.2013.03.03
76. UCHINO K. Piezoelectric ultrasonic motors: overview. *Smart Materials and Structures*. 1998, 7, 273-285. doi: 10.1088/0964-1726/7/3/002
77. KUO, M. W., CHUANG, F. S., NIAN, Y. C., TARNG, S. Y. Precision nano-alignment system using machine vision with motion controlled by piezoelectric motor. *Mechatronics*. 2008, 18(1), 21-34. doi: 10.1016/j.mechatronics.2007.07.010
78. Nanomotion | *Rotary piezo motor* [interactive]. [Last viewed 2016 12 12]. Access via internet: http://www.nanomotion.com/wp-content/uploads/2016/02/ER-15-4_rotary_piezo_102313.pdf
79. WATSON, B., FRIEND, J., YEO, L. Piezoelectric ultrasonic resonant motor with stator diameter less than 250μm: the Proteus motor. *Journal of Micromechanics and Microengineering*. 2009, 19(2), 1-5. doi: 10.1088/0960-1317/19/2/022001
80. JUÁREZ-GALLEGO, A. J., GRAFF, F. K. *Power ultrasonics: applications of high-intensity ultrasound*. Oxford: Woodhead Publishing, 2015.
81. Motor device utilizing ultrasonic oscillation. Inventor: SASHIDA, T. US patent US 4562374 A. 1984-05-16. [Last viewed 2016 12 12]. Access via internet: https://www.google.com/patents/US4562374
82. Shinsei | *Ultrasonic motor* [interactive]. [Last viewed 2016 12 12]. Access via internet: http://www.shinsei-motor.com/English/techno/ultrasonic_motor.html
83. FERREIRA, L. B. D.A, NÓVOA, O. R. P., MARQUES, T. A. Multifunctional material systems: a state-of-the-art review. *Composite Structures*. 2016, 151(1), 3-35. doi: 10.1016/j.compstruct.2016.01.028
84. BISHOP, H. R. *The Mechatronics Handbook*. USA: CRC Press, 2002.
85. Measurement Specialities | *Piezo film sensors: technical manual* [interactive]. [Last viewed 2016 12 12]. Access via internet: https://www.sparkfun.com/datasheets/Sensors/Flex/MSI-techman.pdf
86. CRAIG, K. *Optical encoders. Lecture notes* [interactive]. [Last viewed 2016 12 12]. Access via internet: http://engineering.nyu.edu/mechatronics/Control_Lab/Criag/Craig_RPI/SenActinMecha/S&A_Optical_Encoders.pdf
87. WEBSTER, G. J. *The measurement, instrumentation and sensors handbook*. USA: CRC press, 1999.
88. CARR, J. et al. Miniaturized optical encoder for ultra precision metrology systems. *Precision Engineering*. 2009, 33, 263-267. doi: 10.1016/j.precisioneng.2008.07.003
89. Precizika Metrology | *Rotary encoders* [interactive]. [Last viewed 2016 12 12]. Access via internet: http://metrology.precizika.lt/Products/html
90. ETIC | *Optical encoders* [interactive]. [Last viewed 2016 12 12]. Access via internet: http://www.easttexasic.com/optical-encoders.html

91. Sensors | *Encoder operating principles* [interactive]. [Last viewed 2016 12 12]. Access via internet: http://archives.sensorsmag.com/articles/1198/enc1198/
92. US Digital | *E2 optical kit encoder* [interactive]. [Last viewed 2016 12 12]. Access via internet: http://www.usdigital.com/products/encoders/incremental/rotary/kit/E2
93. Avago Technologies | *AEDR-850x* [interactive]. [Last viewed 2016 12 12]. Access via internet: https://docs.broadcom.com/docs/AV02-2790EN
94. Newark | *AEDR-8500-100* [interactive]. [Last viewed 2016 12 12]. Access via internet: http://www.newark.com/productimages/standard/en_US/4783029.jpg
95. SAUNORIENĖ, L., RAGULSKIS, M., PALEVIČIUS, A., OSTAŠEVIČIUS, V., JANUŠAS, G. Hybrid numerical-experimental moire technique for analysis of microstructures. *SPIE Proceedings*. 2006, 6345, 1-8. doi: 10.1117/12.693150
96. SHAO, J., DING, Y., TIAN, H., LI, X., LI, X., LIU, H. Digital moiré fringe measurement method for alignment in imprint lithography. *Optics & Laser Technology*. 2012, 44, 446-451. doi: 10.1016/j.optlastec.2011.08.010
97. MERINO, S., RETOLAZA, A., JUARROS, A., LANDIS, S. A new way of manufacturing high resolution optical encoders by nanoimprint lithography. *Microelectronic Engineering*. 2007, 84, 848-852. doi: 10.1016/j.mee.2007.01.024
98. ACIKGOZ, C., HEMPENIUS, A. M., HUSKENS, J., VANCSO, J. G. Polymers in conventional and alternative lithography for the fabrication of nanostructures. *European Polymer Journal*. 2011, 47, 2033-2052. doi: 10.1016/j.eurpolymj.2011.07.025
99. HENDRICKS, R. N., CARTER, R. K. Nanoimprint lithography of polymers. *Polymer Science: A comprehensive Reference*. 2012, 7, 251-274. doi: 10.1016/B978-0-444-53349-4.00194-1
100. SHAN, X., LIU, C.Y, LAM, C. Y. Studies of polymer deformation and recovery in micro hot embossing. *Microsystem Technologies*. 2008, 14, 1055-1060. doi: 10.1007/s00542-007-0486-y
101. SYNOWICKI, A. R., JOHS, D. B., MARTIN, C. A. Optical properties of soda-lime float glass from spectroscopic ellipsometry. *Thin Solid Films*. 2011, 519(9), 2907-2913. doi: 10.1016/j.tsf.2010.12.110
102. Pilkington | *Raw materials* [interactive]. [Last viewed 2016 12 13]. Access via internet: http://www.pilkington.com/pilkington-information/about+pilkington/education/float+process/raw+materials.htm
103. SMITH, W. D. et al. Perfluorocyclobutyl copolymers for microphotonics. *Advanced Materials*. 2002, 14, 1585-1589. doi: 10.1002/1521-4095(20021104)14:21<1585
104. BETTIOL, A. A., ANSARI, K., SUM, C. T., VAN KAN, A. J., WATT, F. Fabrication of micro-optical components in polymer using proton beam writing. *SPIE Proceedings*. 2004, 5347, 255-263. doi: 10.1117/12.524300
105. GRIGALIŪNAS, V., JUCIUS, D., TAMULEVIČIUS, S., GUOBIENĖ, A., KOPUSTINSKAS, V. Optically variable imaging using nanoimprint technique.

Applied Surface Science. 2005, 245(1-4), 234-239. doi: 10.1016/j.apsusc.2004.10.015
106. Goodfellow | *Polyethylene terephthalate material information* [interactive]. [Last viewed 2016 12 13]. Access via internet: http://www.goodfellow.com/E/Polyethylene-terephthalate.html
107. Valley design corp. | *Soda lime float glass* [interactive]. [Last viewed 2016 12 13]. Access via internet: http://www.valleydesign.com/sodalime.htm
108. Morgan Advanced Materials | *Hard PZT* [interactive]. [Last viewed 2016 12 01]. Access via internet: http://www.morgantechnicalceramics.com/en-gb/materials/lead-zirconate-titanate-pzt/hard-pzt/
109. Morgan Advanced Materials | *PZT 400 series* [interactive]. [Last viewed 2016 12 01]. Access via internet: http://www.morgantechnicalceramics.com/media/2323/pzt400-series.pdf
110. SolidWorks | *SolidWorks Premium 2016* [interactive]. [Last viewed 2016 12 01]. Access via internet: http://files.solidworks.com/pdf/SW2016_Premium_DS_ENU.pdf
111. SolidWorks | *Commercial industries* [interactive]. [Last viewed 2016 12 01]. Access via internet: http://www.solidworks.com/sw/industries/mechanical-design-industries.htm
112. Cambridge University Engineering Department. *Materials data book* [interactive]. 2003. [Last viewed 2016 12 01]. Access via internet: http://www-mdp.eng.cam.ac.uk/web/library/enginfo/cueddatabooks/materials.pdf
113. HECKER JR., C. J. *Anodising aluminium*. 284-293 [interactive]. [Last viewed 2016 12 02]. Access via internet: http://infohouse.p2ric.org/ref/02/01433.pdf
114. NGUYEN, H. T. *Electrically conductive anodized aluminum surfaces* [interactive]. 2006. [Last viewed 2016 12 02]. Access via internet: http://www.techbriefs.com/component/content/article/ntb/tech-briefs/materials/1159
115. ASM Aerospace Specification Metals Inc. | *AISI type 304 stainless steel* [interactive]. [Last viewed 2016 12 02]. Access via internet: http://asm.matweb.com/search/SpecificMaterial.asp?bassnum=MQ304A
116. Outokumpu | *Mechanical properties* [interactive]. [Last viewed 2016 12 02]. Access via internet: http://www.outokumpu.com/en/products-properties/more-stainless/mechanical-properties/Pages/default.aspx
117. MADOU, J. M. *Fundamentals of Microfabrication: the science of miniaturization*. USA: CRC Press, 2002
118. ANSYS | *Products* [interactive]. [Last viewed 2016 12 02]. Access via internet: http://www.ansys.com/Products
119. ANSYS | *About ANSYS* [interactive]. [Last viewed 2016 12 02]. Access via internet: http://www.ansys.com/About-ANSYS
120. ANSYS | *Mechanical products* [interactive]. [Last viewed 2016 12 02]. Access via internet: http://resource.ansys.com/staticassets/ANSYS/staticassets/resourcelibrary/brochure/ansys-mechanical-suite-brochure.pdf

121. TUMASONIENĖ I. *Precizinių mikrorobotų pjezokeitiklių savųjų formų atpažinimo problema. Daktaro disertacija*. Vilnius: Technika, 2009.
122. BANSEVIČIUS et al. Analysis of cylindrical piezoelectric actuator used in 3-DOF deflectors. *Latest Trends in Engineering Mechanics, Structures, Engineering Geology*, p. 86-91. ISBN: 978-960-474-376-6
123. STEFANCU, A., MELENCIUC, S., BUDESCU, M. Penalty based algorithms for frictional contact problems. *The Bulletin of the Polytechnic Institute of Jassy – Construction. Architecture Section.* 2011, 61(3), 119-129.
124. OLSSON, E., FORSBERG, F. Three-dimensional selective imaging of sound sources. *Optical Engineering*. 2009, 48(3). doi: 10.1117/1.3093609
125. Polytec | *Basic principles of vibrometry* [interactive]. [Last viewed 2016 11 24]. Access via internet: http://www.polytec.com/us/solutions/vibration-measurement/basic-principles-of-vibrometry /
126. Wikipedia | *Laser scanning vibrometry* [interactive]. [Last viewed 2016 11 24]. Access via internet: https://en.wikipedia.org/wiki/Laser_scanning_vibrometry
127. Slideshare | *An introduction to scanning laser vibrometry for non-contact vibration measurement* [interactive]. [Last viewed 2016 11 24]. Access via internet: http://www.slideshare.net/iyovan/webinar-intro-toscanningvibrometryapril2013
128. KREISS, T. *Handbook of holographic interferometry: optical and digital methods*. Germany: Wiley-VCH Verlag GmbH & Co, 2005.
129. PALEVICIUS P. et al. Applicability of time-averaged holography for micro-electro-mechanical system performing non-linear oscillations. *Sensors*. 2014, 14, 1805-1821. doi: 10.3390/s140101805
130. PALEVIČIUS, A., HAYMAN, G., STEINZIG, M. Holographic PRISMA system for investigation of mechatronic systems. *Proceedings of the 6th International Conference Vibroengineering* 2006. Conference Proceeding, 2006. pp. 27-29.
131. RAGULSKIS, M., PALEVIČIUS, A., RAGULSKIS, L. Plotting holographic interferograms for visualization of dynamic results from finite-element calculations. *International Journal for Numerical Methods in Engineering*. 2003, 56, 1647-1659. doi: 10.1002/nme.632
132. VEST, C. M. *Holographic Interferometry*. USA: John Wiley and Sons Inc., 1979.
133. HO, T. S, JAN, J. S. A piezoelectric motor for precise precision positioning applications. *Precision Engineering*. 2016, 43, 285-293. doi: 10.1016/j.precisioneng.2015.08.007
134. LI, J. et al. A piezoelectric-driven rotary actuator by means of inchworm motion. *Sensors and Actuators A: Physical*. 2013, 194, 269-276. doi: 10.1016/j.sna.2013.02.020
135. LI, J. et al. Development of a compact 2-DOF precision piezoelectric positioning based on inchworm principle. *Sensors and Actuators A: Physical*. 2015, 222, 87-95. doi: 10.1016/j.sna.2014.12.001
136. BAGAD, S. V. *Mechatronics*. India: Technical Publications Pune, 2008.

137. KO, H.P., KIM, S., KIM, J.S., KIM, H.J., YOON, S. J. Wear and dynamic properties of piezoelectric ultrasonic motor with frictional materials coated stator. *Materials Chemistry and Physics*. 2005, 90(2-3), 391-395. doi: 10.1016/j.matchemphys.2004.09.037
138. IRWIN, D. J. *Mechanical Engineer's Handbook*. USA: Academic Press, 2001.
139. Hypertextbook | *Coefficients of friction for teflon* [interactive]. [Last viewed 2016 12 03]. Access via internet: http://hypertextbook.com/facts/2004/GarvinTam.shtml
140. VILYS, J., TAMULEVIČIUS, S., GRIGALIŪNAS, V., MEŠKINIS, Š, GUOBIENĖ, A. *Paviršiaus inžinerija ir nanotechnologijos*. Kaunas: Vitae Litera, 2007.
141. MALINAUSKAS K. *Micro-opto-electromechanical (MOEMS) system development and adaptation for non-invasive blood pulse analysis. Doctoral dissertation*. Kaunas: Technologija, 2013.
142. The Chemistry Hypermedia Project | *Ultraviolet and visible absorption spectroscopy (UV-Vis)* interactive]. [Last viewed 2016 11 20]. Access via internet: http://www.tissuegroup.chem.vt.edu/chem-ed/spec/uv-vis/uv-vis.html
143. PALMER, C. *Diffraction grating handbook*. [interactive]. 2002. [Last viewed 2016 11 21]. Access via internet: http://optics.hanyang.ac.kr/~shsong/Grating%20handbook.pdf
144. LEYBOLD | *P5834 diffraction gratings*. [interactive]. [Last viewed 2016 11 20]. Access via internet: http://photonics.ld-didactic.de/Educational%20Kits/P5834.html
145. BORN, M., WOLF, E. *Principles of optics: electromagnetic theory of propagation. Interference and diffraction of light*. 7th ed. UK: Cambridge University Press, 1999.

LIST OF PUBLICATIONS

Papers in Web of Science journals with impact factor

1. Bansevičius, Ramutis Petras; Bubulis, Algimantas; Grybas, Ignas; Jūrėnas, Vytautas; Kulvietis, Genadijus. Development of two modifications of piezoelectric high resolution rotary table // Journal of Vibroengineering / Vibromechanika, Lithuanian Academy of Sciences, Kaunas University of Technology, Vilnius Gediminas Technical University. Kaunas: Vibroengineering. ISSN 1392-8716. 2013, Vol. 15, no. 4, p. 2124-2129. [Science Citation Index Expanded (Web of Science); INSPEC; Academic Search Complete; Central & Eastern European Academic Source (CEEAS); Computers & Applied Sciences Complete; Current Abstracts; TOC Premier]. [IF: 0,660; AIF: 2,255; IF/AIF: 0,293; Q3; 2013 Journal Citation Reports® Science Edition (Thomson Reuters, 2016)].
2. Jucius, Dalius; Grybas, Ignas; Grigaliūnas, Viktoras; Mikolajūnas, Marius; Lazauskas, Algirdas. UV imprint fabrication of polymeric scales for optical rotary encoders // Optics and laser technology. Oxford: Elsevier. ISSN 0030-3992. 2014, vol. 56, p. 107-113. [Science Citation Index Expanded (Web of Science)]. [IF: 1,647; AIF: 2,732; IF/AIF: 0,603; Q2; 2014 Journal Citation Reports® Science Edition (Thomson Reuters, 2016)].
3. Grybas, Ignas; Bubulis, Algimantas; Bansevičius, Ramutis Petras; Jūrėnas, Vytautas. Research of rotary piezotable driven by two harmonic signals // Mechanika / Kauno technologijos universitetas, Lietuvos mokslų akademija, Vilniaus Gedimino technikos universitetas. Kaunas: KTU. ISSN 1392-1207. 2014, Vol. 20, no. 6, p. 573-576. [Science Citation Index Expanded (Web of Science); INSPEC; Compendex; Academic Search Complete; FLUIDEX; Scopus]. [IF: 0,292; AIF: 1,862; IF/AIF: 0,157; Q4; 2014 Journal Citation Reports® Science Edition (Thomson Reuters, 2016)].
4. Grybas, Ignas; Bansevičius, Ramutis Petras; Jūrėnas, Vytautas; Bubulis, Algimantas; Janutėnaitė, Jūratė; Kulvietis, Genadijus. Ultrasonic standing waves-driven high resolution rotary table // Precision engineering. New York, NY: Elsevier. ISSN 0141-6359. 2016, vol. 45, p. 396-402. [Science Citation Index Expanded; Academic Search Alumni Edition; Academic Search Complete; Academic Search Elite; Academic Search Premier; Academic Search Research & Development; Current Contents (Engineering, Computing & Technology); Ingenta Connect; ScienceDirect]. [IF: 1,914; AIF: 2,736; IF/AIF: 0,700; Q1; 2015 Journal Citation Reports® Science Edition (Thomson Reuters, 2016)].

Papers in journals referred in other international databases

1. Grybas, Ignas; Bansevičius, Ramutis Petras; Bubulis, Algimantas; Jūrėnas, Vytautas; Janutėnaitė, Jūratė; Kulvietis, Genadijus. R and D of high resolution rotary table based on the ultrasonic standing waves // Vibroengineering Procedia: international conference Vibroengineering - 2014, Katowice, Poland, 13-15 October, 2014. Kaunas: JVE International. ISSN 2345-0533. 2014, vol. 3, p. 55-58. [Compendex; Academic OneFile].

National patents

1. Bansevičius, Ramutis Petras; Bubulis, Algimantas; Grybas, Ignas; Jūrėnas, Vytautas; Kasparaitis, Albinas. LT 6129 B. Aukštos skyros pjezoelektrinis kampinio pozicionavimo įrenginys / išradėjai: Ramutis Bansevičius, Algimantas Bubulis, Ignas Grybas, Vytautas Jūrėnas, Albinas Kasparaitis; pareiškėjas: Kauno technologijos universitetas. 2015-03-25. 4 p. [Lietuvos Respublikos patentų duomenų bazė].
2. Bansevičius, Ramutis Petras; Grybas, Ignas; Bubulis, Algimantas; Jūrėnas, Vytautas. LT 6254 B. Sukamojo judesio pjezoelektrinė pavara / išradėjai: Ramutis Bansevičius, Ignas Grybas, Algimantas Bubulis, Vytautas Jūrėnas; pareiškėjas: Kauno technologijos universitetas. 2016-03-10. 4 p. [Lietuvos Respublikos patentų duomenų bazė].

SL344. 2017-07-21, 18,75 leidyb. apsk. l. Tiražas 12 egz. Užsakymas 234.
Išleido Kauno technologijos universitetas, K. Donelaičio g. 73, 44249 Kaunas
Spausdino leidyklos „Technologija“ spaustuvė, Studentų g. 54, 51424 Kaunas

APPENDIX A

The operation principles of piezoelectric non-resonant motors and drives

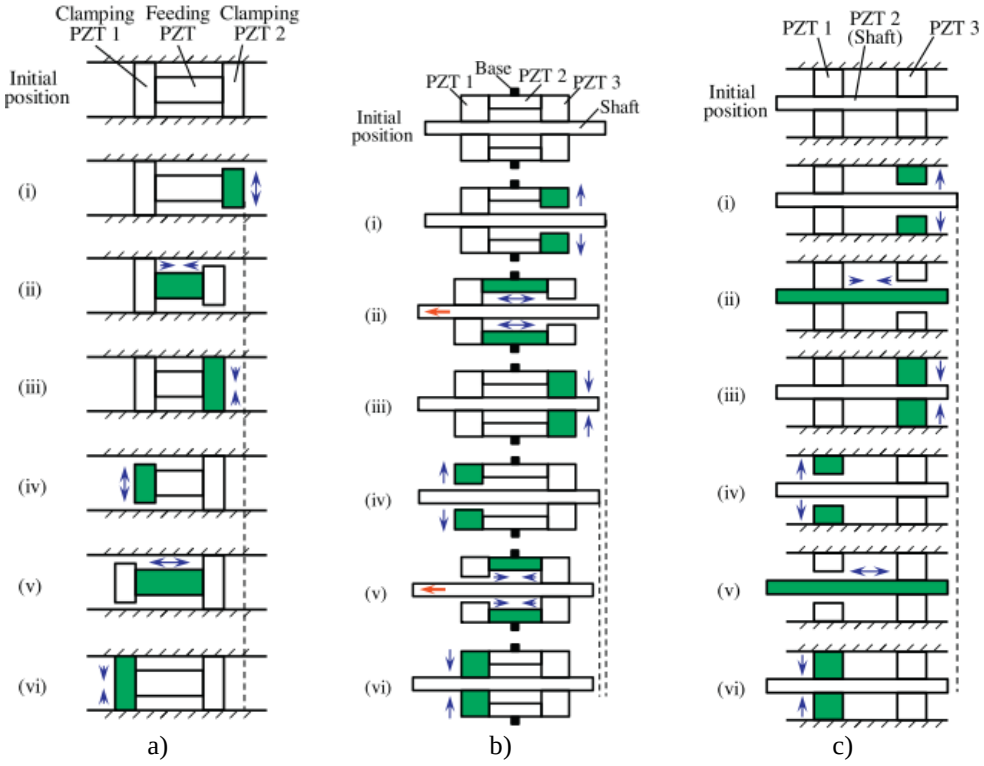

Fig. 1. Operation principle of inchworm motor mechanism in ”walker” (a), “pusher” (b), and “walker-pusher” (c) mode [26]

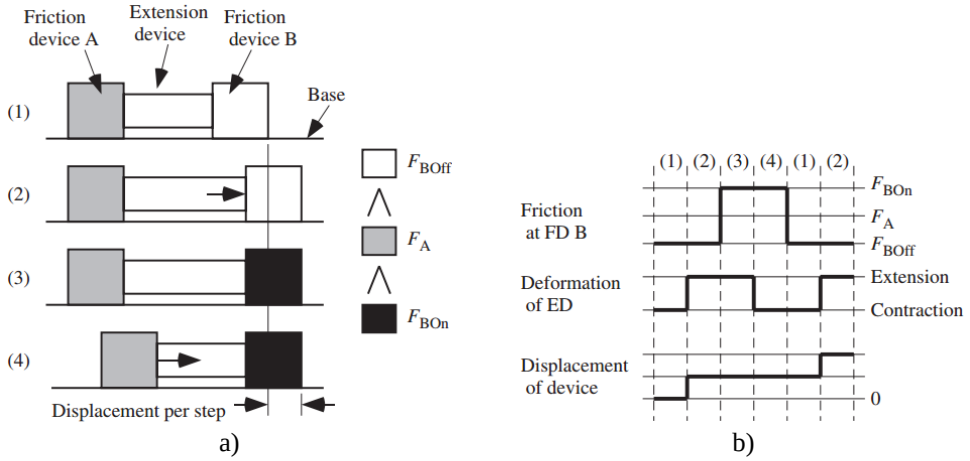

Fig. 2. Operation principle of seal motor: a) motion mechanism; b) timing chart [45]

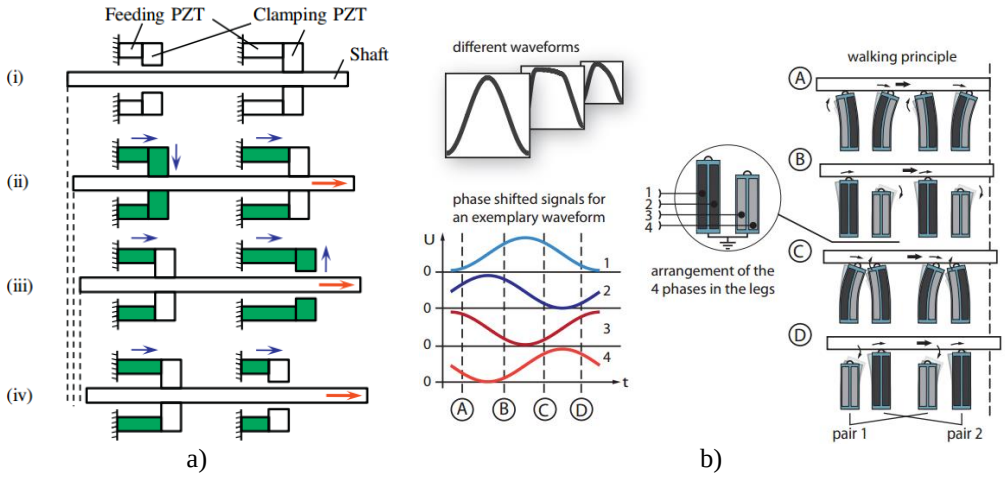

Fig. 3. Operation principle of a walking motor: a) classical mechanism; b) novel approach in stepping mode [26, 48]

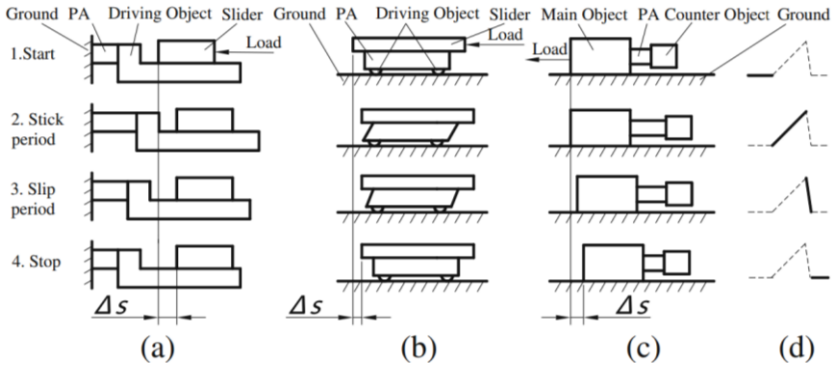

Fig. 4. Operation principles of PFIA-driven motors: a) impact drive (stick-slip) mechanism; b) self-inertia mechanism; c) impact-inertia mechanism; d) corresponding stimulating voltage [54]

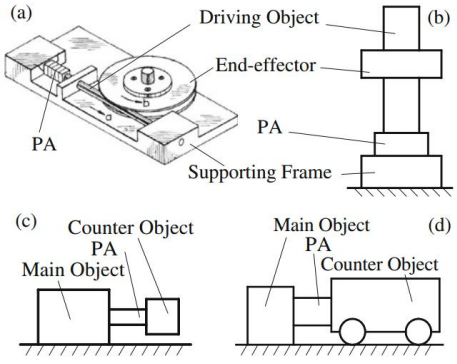

Fig. 5. The typical structure of PFDA-driven (a – rotary, b – linear) and PIDA-driven (c – with suspended counter object, d – with supported counter object) motor [54]

APPENDIX B

The main properties of piezoceramics PZT-401 [109]

Properties	Symbol	Value	Unit
Density	ρ	7,600	kg/m3
Young's modulus	E	78	GPa
Poisson's ratio	σ	0.31	-
Curie temperature	T_C	330	^oC
Max. operating temperature	T_{max}	165	^oC
Compliances (elastic constants)	S^E_{33}	15.6	pm^2/N
	S^E_{11}	12.7	pm^2/N
Dielectric constants	K^T_{33}	1,395	-
	K^T_{11}	1,475	-
Dielectric loss	$\tan\delta$	0.2	%
Coupling factors	k_p	0.58	-
	k_{31}	0.35	-
	k_{33}	0.67	-
Piezoelectric (charge or strain) constants	d_{33}	315	pC/N or pm/V
	d_{31}	132	pC/N or pm/V
Piezoelectric (voltage or stress) constants	g_{33}	25.5	mV·m/N
	g_{31}	10.7	mV·m/N
Mechanical quality factor	Q_m	600	-

APPENDIX C

Results of modal analyses of piezocylinder

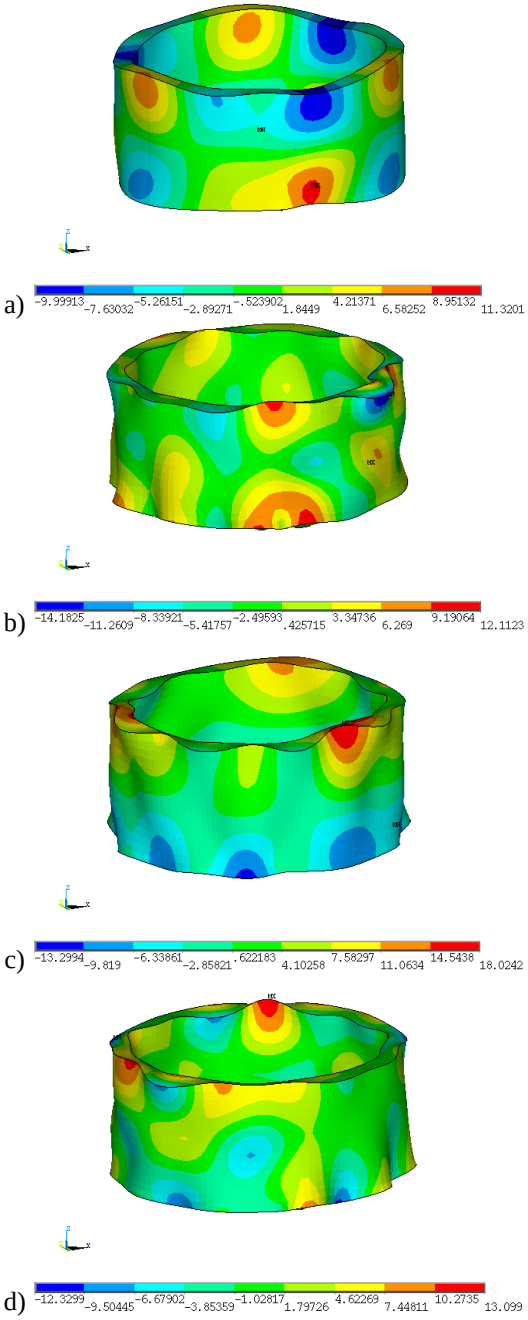

Fig. 1. Displacement of piezocylinder in axial direction (modal analysis) caused by vibration modes at resonant frequency of: a) 128.61 kHz; b) 128.67 kHz; c) 128.78 kHz (128.4-129.4 kHz interval; U = 60 V) and 131.53 kHz (131-132 kHz interval; U = 60 V)

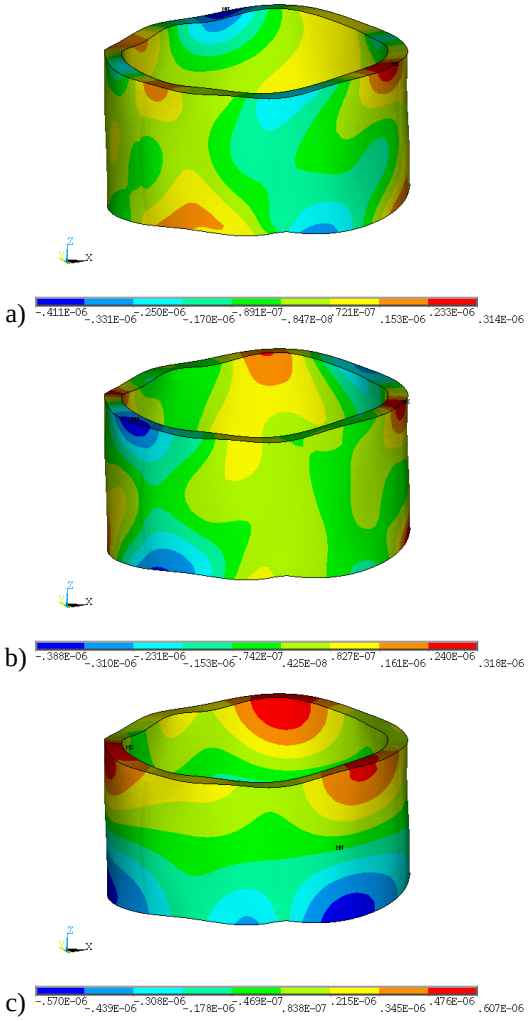

Fig. 2. Displacement of piezocylinder (harmonic analysis) in tangential (a), radial (b) and axial (c) directions caused by vibration mode at resonant frequency of 126.23 kHz (U = 60 V)

APPENDIX D

Results of mathematical modelling of interaction between PC and rotor: a) positions of two contacting points in axial direction in time; b) tangential displacement of the rotor in time; c) total angular displacement of the rotor in time; d) motion trajectory of the contact zone element in tangential-axial plane

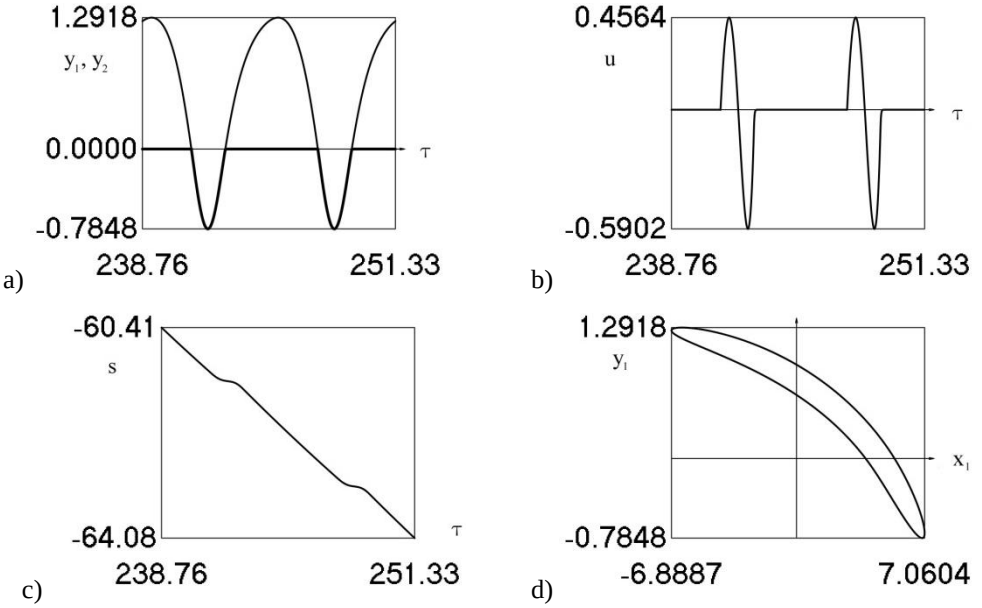

Fig. 1. Response during steady state motions, when $\nu = 1$ and $l = 0$

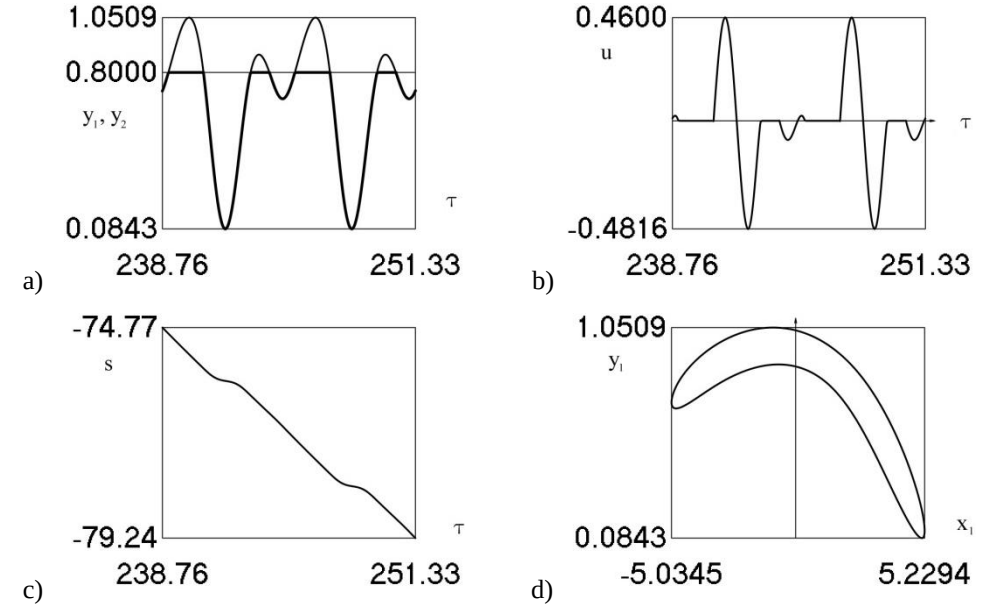

Fig. 2. Response during steady state motions, when $\nu = 1$ and $l = 0.8$

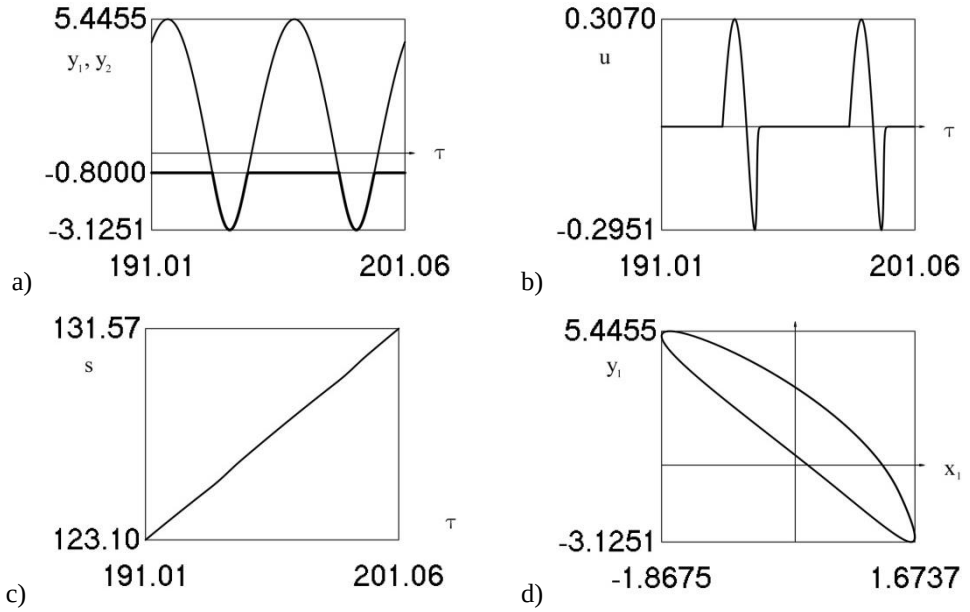

Fig. 3. Response during steady state motions, when $\nu = 1.25$ and $l = -0.8$

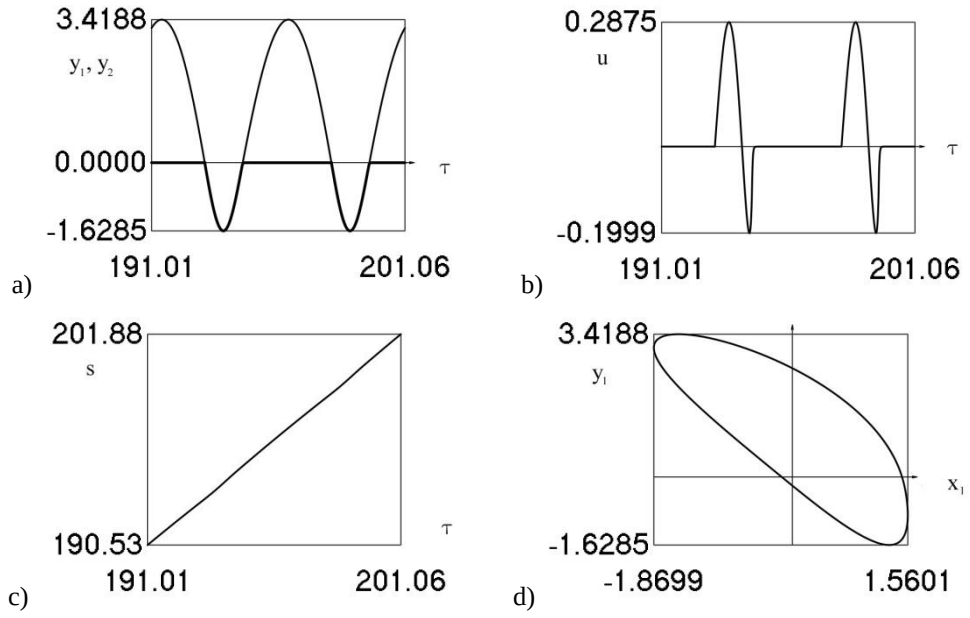

Fig. 4. Response during steady state motions, when $\nu = 1.25$ and $l = 0$

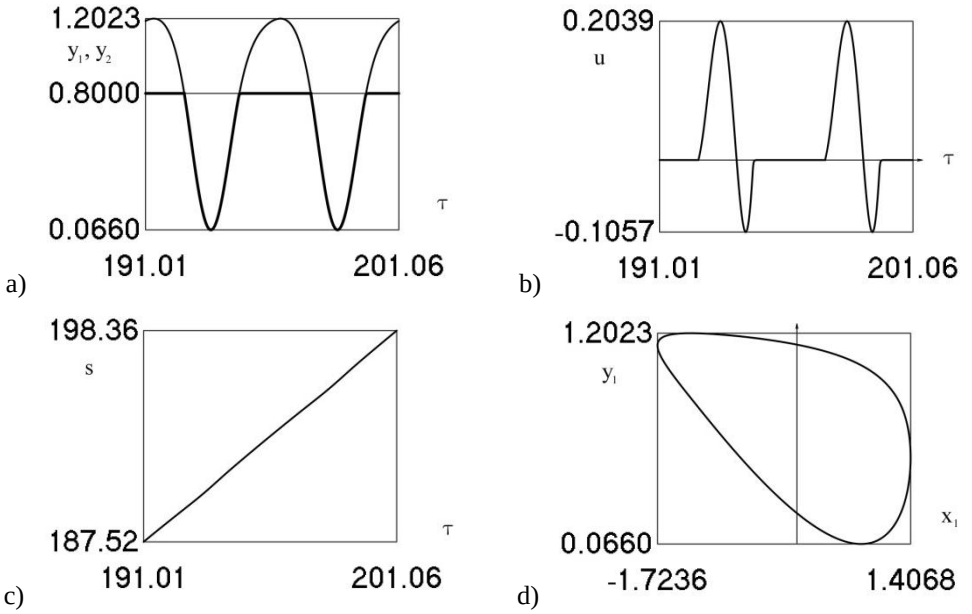

Fig. 5. Response during steady state motions, when $\nu = 1.25$ and $l = 0.8$

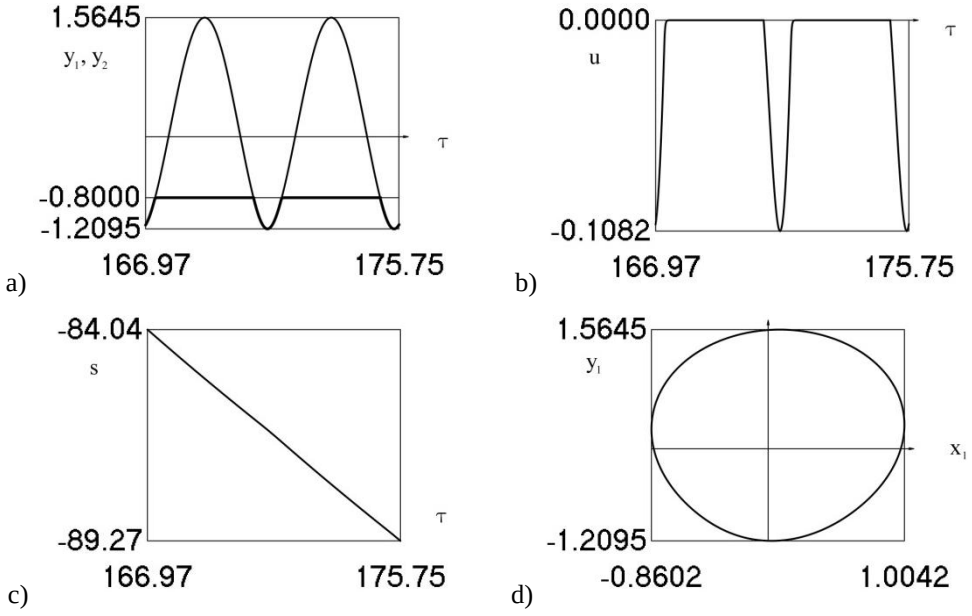

Fig. 6. Response during steady state motions, when $\nu = 1.43$ and $l = -0.8$

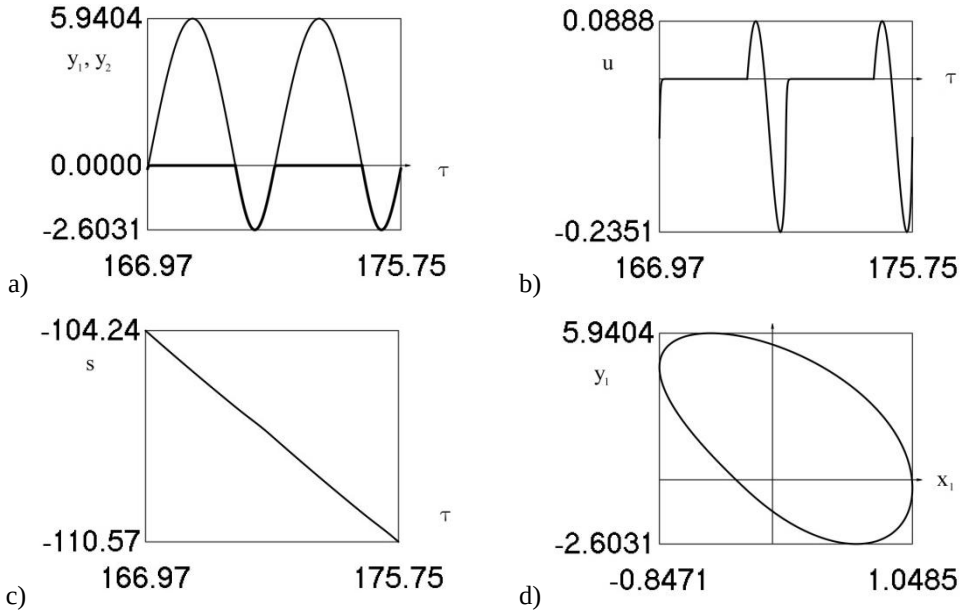

Fig. 7. Response during steady state motions, when $\nu = 1.43$ and $l = 0$

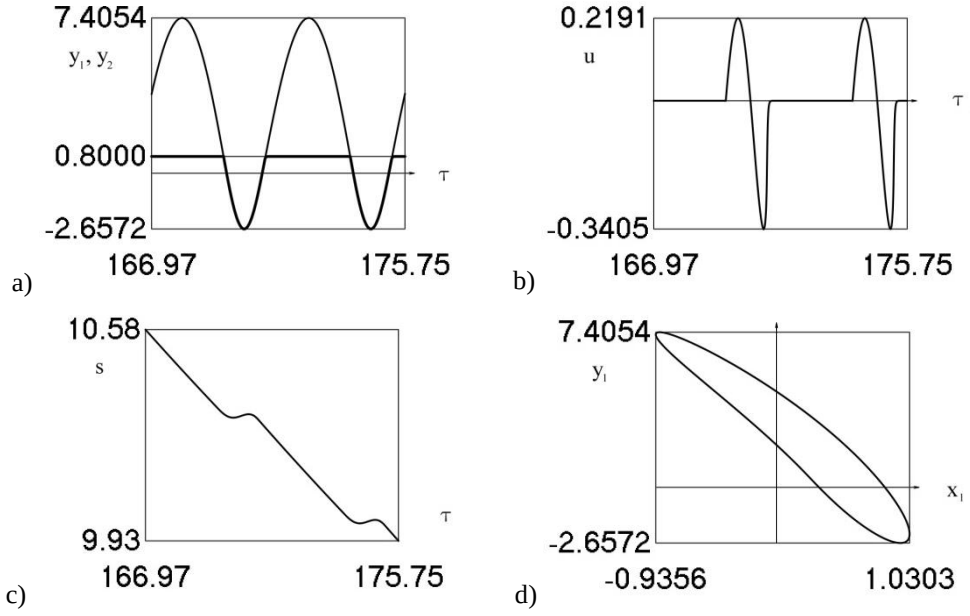

Fig. 8. Response during steady state motions, when $\nu = 1.43$ and $l = 0.8$

APPENDIX E

Transient response of interaction between piezocylinder and rotor

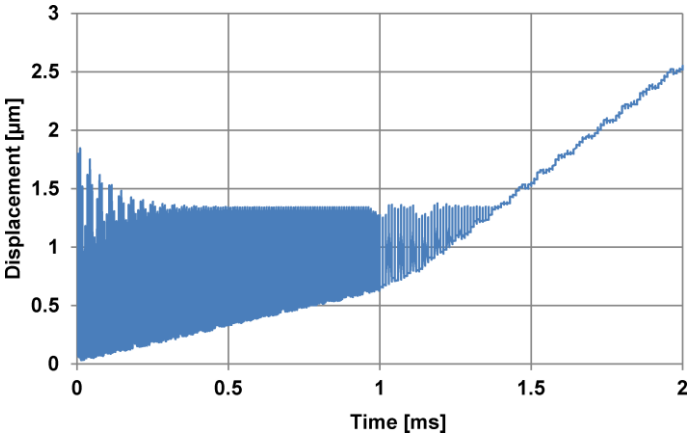

a)

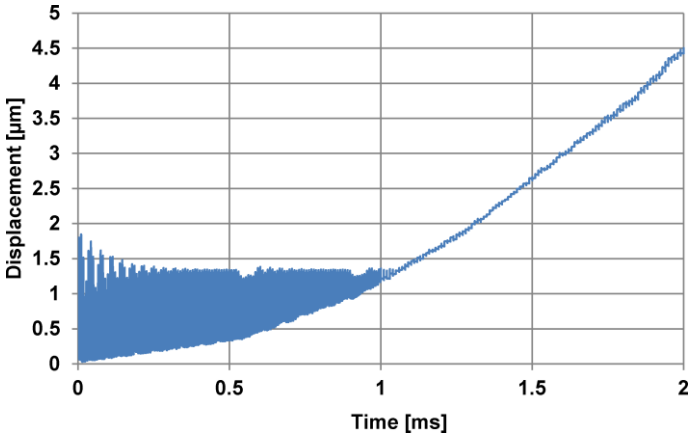

b)

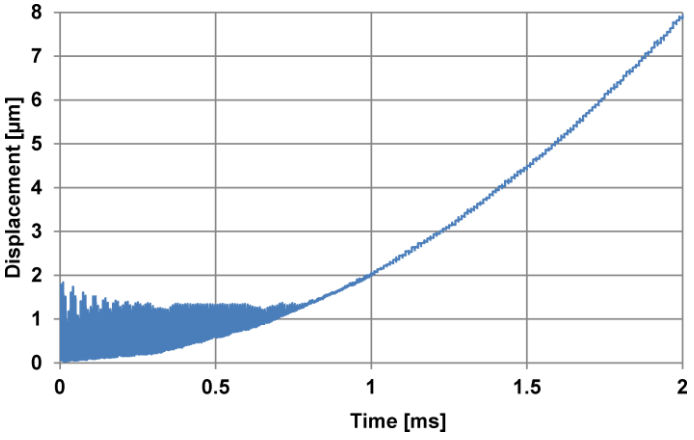

c)

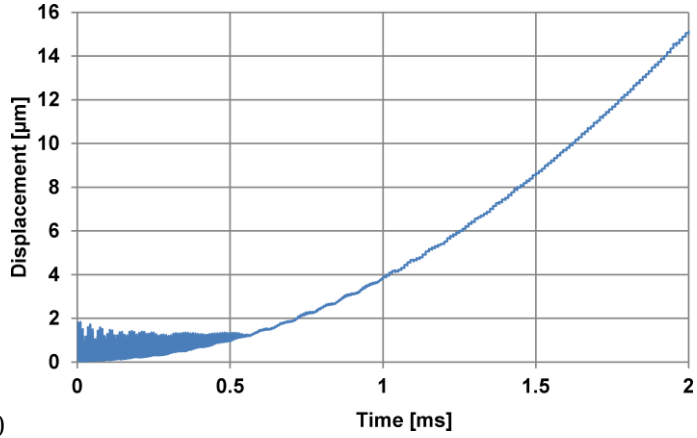

d)

Fig. 1. Transient response of the analysed structure in terms of the maximal tangential displacement at the centres of the contact zone elements after the start of electrical excitation, when the applied external load is: a) 0.1 kg; b) 0.25 kg; c) 0.5 kg; d) 1 kg

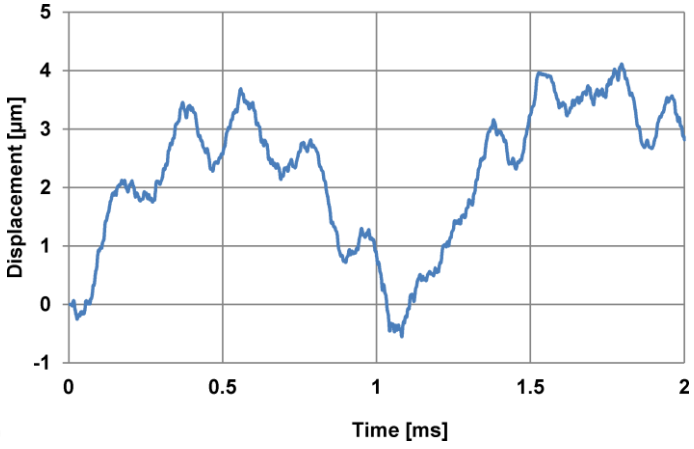

a)

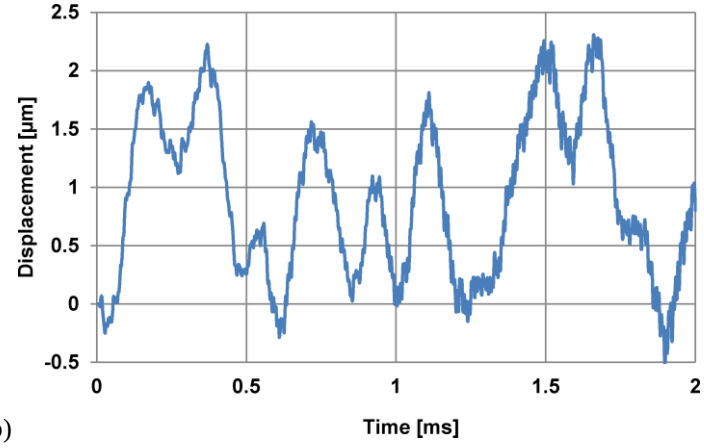

b)

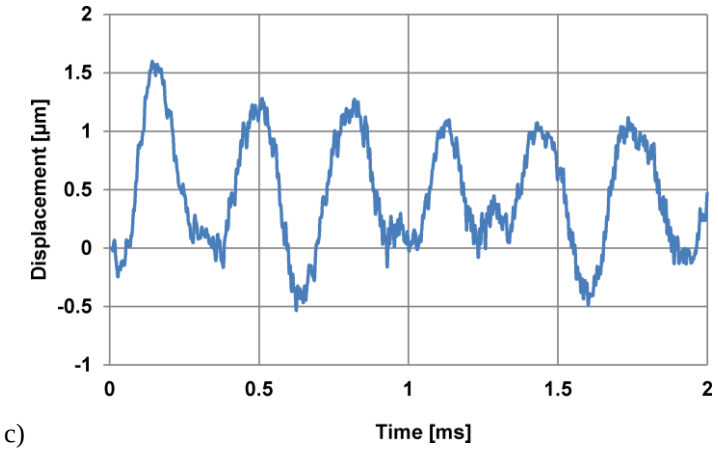

c)

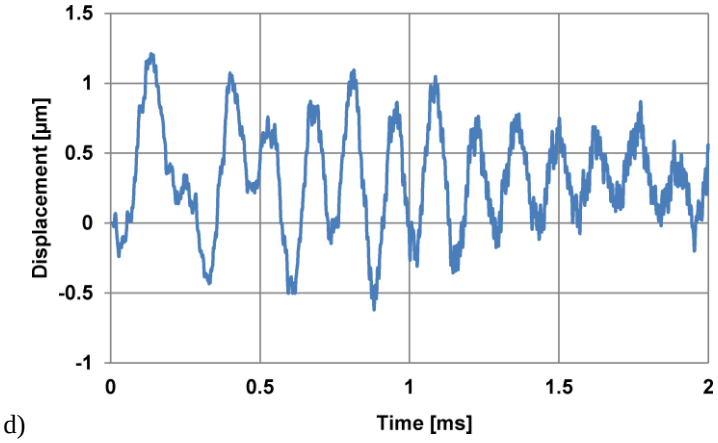

d)

Fig. 2. Transient response of the arbitrary selected point of the rotor with respect to the axial displacement after the start of electrical excitation when applying the external load of: a) 0.1 kg; b) 0.25 kg; c) 0.5 kg; d) 1 kg